Developing Experimental setup for Trapped Ion based Optical Atomic Clock

Thesis submitted to AcSIR For the Award of
the Degree of
DOCTOR OF PHILOSOPHY
In Physical Sciences

By
Atish Roy
Enroll.No: 10PP16A32010

Under the guidance of
Dr. Subhadeep De
&
Dr. Subhasis Panja

CSIR-National Physical Laboratory
New Delhi, India, 110012
June 2019

Certificate

This is to certify that the work incorporated in this Ph.D. thesis entitled **"Developing Experimental setup for Trapped Ion based Optical Atomic Clock"** submitted by **Mr. Atish Roy** to Academy of Scientific and Innovative Research (AcSIR) in fulfillment of the requirements for the award of the Degree of **"Doctor of Philosophy in Physical Sciences"**, embodies original research work under our supervision. We further certify that this work has not been submitted to any other University or Institution in part or full for the award of any degree or diploma. Research material obtained from other sources has been duly acknowledged in the thesis. Any text, illustration, table etc., used in the thesis from other sources, have been duly cited and acknowledged.

It is also certified that this work done by the student, under our supervision, is plagiarism free.

Atish Roy
(Enroll No. :10PP16A32010)

Dr. Subhadeep De
Supervisior
Indian Standard Time Division
CSIR-National Physical Laboratory
New Delhi 110012

Dr. Subhasis Panja
Co-Supervisior
Indian Standard Time Division
CSIR-National Physical Laboratory
New Delhi 110012

Acknowledgement

My interest in the field of research led me to embark on the path of Ph.D. which finally landed me to the "Single trapped ion optical frequency standard (STIOS)" lab of CSIR-NPL. One's Ph.D. life is not easy, apart from the many good things that a PhD teaches a scholar, there are various hurdles and ups and downs that one has to go through. Same is the case with mine too, but such hindrances could never dissuade me from moving ahead in my research step by step. This was possible due to the efforts and presence of many people around me. I want to thank those people and give them due acknowledgement for their contributions and help throughout the journey of my PhD work. It would have been strenuous to accomplish my journey through Ph.D. without them.

First and foremost, I would like to thank my parents for everything; for their tremendous moral support, encouragement and unwavering belief in me. My heartfelt and immense gratitude goes to my Ph.D. supervisor and mentor Dr. Subhadeep De for his unvarying guidance, valuable suggestions, great patience, and constant encouragement and support throughout the entire period of my thesis work. His dedication to scientific research and sincerity in his duty as a Ph.D. supervisor despite of his busy schedule has always been a source of motivation to me. His insightful criticism and precious knowledge in varied areas has led to my growth as a researcher and will in fact help me in building my career. He gave me the opportunity to learn to build up an experiment from scratch, which is indeed a great and lifetime experience for me.

I am greatly thankful to my Co-Supervisor Dr. Subhasis Panja; my DAC members Dr. Jiji Pulikkotil, Dr. S. K. Dubey and Dr. Nahar Singh; and current H.O.D. of our division, Dr. Anurag Gupta whose advice during evaluatory presentations of my work have improved my knowledge as well as my thesis. I shall always remain grateful to Prof. Amitava Sen Gupta, former Divisional Head of Indian Standard Time Division, for promoting and boosting my interest in Electronics and Instrumentation and for giving his valuable time for occasional scientific discussions. He has been and will always be a source of inspiration to me. I extend my heartfelt thanks to our collaborators Dr. B. K. Sahoo (Physical Research Laboratory, Ahmedabad) and Dr. Bindiya Arora (Guru Nanak Dev University, Amritsar) because of whom I had the opportunity to get the taste of theoretical work too. My sincere vote of thanks also goes to Dr. Mahesh Kumar, CSIR-NPL, Delhi and D. Rao, BARC Vizag who gave me access to their laboratory and research facilities.

A good quality sustaining system is significant to surviving and staying sane during doctoral

thesis work and I am lucky enough to have one. Away from home to Delhi for pursuing Ph.D. was heavy-heartening for me but my senior Neha Batra had always been helpful and cheering me up since Day One, making me comfortable in the lab. I thank her for her amicable behavior and for all those lab-related discussions. I am thankful to Thangjam Jayenta for his assistance in construction of the STIOS lab and to Sankar Majhi and Dr. Aishik Acharya to whom I can approach unhesitatingly for any electronics related discussions and doubt clearance. For helping me in learning VHDL and FPGA based programming, I thank my former labmate Anindya Rastogi. I extend my deep sense of acknowledgement to my lab mate and friend, Lakhi Sharma who has always been helpful in all spheres. I thank her for constantly being there to boost up my confidence and lighten up my pessimistic temperament during failures in my research work. I express my gratitude towards her for being the "Grammarly" of my research papers including my Thesis and many other paper works. My lab mates Harish Rathore, Neelam and Kavita who have recently joined the STIOS lab always come up to me with their doubts and for other suggestions regarding our ongoing experiment, this has in turn cleared my understanding too to a deeper level. I therefore thank all my fellow lab mates for the thought-provoking discussions, for the sleepless nights we all had worked together to accomplish our tasks before deadlines, and for all the good moments and the party time we have had in my journey.

I sincerely thank Dr. V. N. Ojha, Dr. Ashish Aggarwal, Dr. Poonam Arora, Pranalee Thorat, Trilok Bhardwaj, Dr. Bharath Vattikonda and Dr. Manoj Das for their encouragement, various scientific discussions and help troughout the journey. My special words of thanks should also go to the technical staff of our division Shuchi Mam, Mahavir Sir, Ved Prakash Ji, Sajjan Ji, Devender Ji, Prem Ji and Kaushik Ji, who have always been there for guidance and help in various administrative processes including the "head-aching" indentation work. A special mention of thanks to AcSIR and the HRD members of our institute Soma Ma'am, Manju Ma'am and Joshi Sir who have always been co-operative in all paper works related to my PhD or for attending conferences and other dealings. I am also grateful to IEEE for giving me an opportunity to attend the EFTF conference in Besançon, France by fully funding it. Last but not the least; I would like to thank Dr. D. K. Aswal, Director, CSIR-NPL for allowing me to carry out my research work in this esteemed laboratory. I gratefully acknowledge the financial support meted out by various funding agencies as DAE-BRNS, DRDO and CSIR which helped in accomplishment of my thesis work. It is actually impossible to mention each and every person who had an impact on my work but I am immeasurably grateful to each one of them as with such amazing people, my Ph.D. journey have been a wonderful one despite of various frustrating hurdles.

At last, I would like to thank Baba Vishwanath for rendering me the knowledge, ability and patience to embark on this research study and to persist and accomplish it satisfactorily.

Abstract

Among the seven basic units of measurement in International System (SI) of units, "second" is measured most accurately with the help of atomic clocks. The evolution of science and technology demands the updation of the precision in measurements to improve the time and frequency metrology. Being the National Metrology Institute (NMI) of India at CSIR-NPL, we are designing a state-of-the-art optical atomic clock using a single trapped Ytterbium (Yb) ion, which will have more accuracy compare to the present microwave based atomic clock. In future, the optical atomic clock is expected to be the new definition of the SI second and peruser time keeping with an inaccuracy over the age of the universe (13.8 billion years). Developing the Yb ion based optical clock involves the accomplishment of a plethora of subsegments including designing, fabrication, instrumentation, various measurements, in the areas of vacuum system, optical setups, electronic modules, software development and so on. This thesis expounds the instrumentation part of the precision ion-trap experiment which includes indigenously designed and developed devices which are requisites of the experiment. In addition, theoretical study is carried out on estimation of the BBR shift, magic wavelength and tuneout wavelength, for in-depth understanding of the systematics. During the measurement, the clock states of Yb ion get perturbed due to environmental factors like black body radiation, AC and DC electric and magnetic fields, leading to uncertainty in the measured quantity. The correct knowledge of the perturbation can be accounted to minimize the uncertainty. Due to this reason we calculate the static and dynamic polarizability of the clock states. We also calculate the magic and tune out wavelengths which may be used as a tool for trapping ions in an optical lattice leading to suppression of their micromotions. Probing this experiment for clock transition follows steps like production of ions, trapping them in an ion trap, laser cooling and state preparation, exciting the clock transition and detection *etc.* Controlling all the associated modules manually within a small interval of time is not possible and thus requires a complete automation so that their operation is free from human errors. To solve this problem, we have developed a universal digitally operated addressing cum control module, the details of which are described in this thesis. During fabrication of the precision ion trap, there will be some machining errors which results to spatial shifting of the trap center relative to the center of the vacuum chamber. To correct this we use compensating electrodes which connect with a redundant and stable low noise DC voltage source to control the position of ion in the trap. Our indigenously developed

voltage source are presented in this thesis, that is able to give output from 0 to 100 V DC with a resolution of 3 mV and long term stability of 1.9 mV. The voltage source is completely computer controlled and programmable. For cooling of the ions, there is requirement of correct laser frequency matching to the resonance transition. To stabilize the laser frequency with respect to any reference point, we designed and developed field programmable gate array based low noise servo controller which contain function generator, lock-in amplifier and Proportional-Integrator-Derivative controller. Using this module we are able to lock frequency of our laser for a week. In case of Yb ion, reference points required for locking some of its transition frequencies is unavailable to be driven by the conventional saturation absorption spectroscopy technique. Due to this reason, we use transfer cavity technique where a laser is frequency stabilized with respect to an atomic transition and is then used to stabilize a Fabry Perot (FP) cavity. This stabilized FP cavity is then treated as the reference cavity to lock frequencies of other useful lasers using standard Pound-Drever Hall technique. Frequency of laser light is often required to be shifted by hundreds of MHz to few GHz for which generally AOMs and EOMs are used. In this thesis, the design and development of the in-house built AOM and EOM drivers has also been reported. Both the drivers are fully computer controlled and automated. Upon development of the described instrumentation, at present we are in a situation to trap ytterbium ion towards our aimed experiment. The work pursued within the scope of my doctoral study, we developed several important instrumentation for CSIR-NPL's mission mode project "Indigenous development of the state-of-the-art quantum standard of time" particulary for its one of the objective "Optical frequency standard".

Table of Contents

1. **Introduction** 3
1.1 Ytterbium-ion optical frequency standard 7
1.2 Experimental challenges 10
1.3 Objective and outcome of the thesis 11

2. **Polarizability, Magic and Tuneout Wavelength Calculation of Yb^+ Clock Transition** 15
2.1 Introduction 15
2.2 Theory of polarizability 16
2.3 Method of calculations 19
2.4 Results and Discussion 22
2.4.1 Static polarizability 22
2.4.2 Magic wavelengths for linearly and circularly polarized light 27
2.4.3 Magic wavelengths for comprehensive trapping 29
2.4.4 Tune-out wavelengths 31
2.5 Conclusion 32

3. **Low Noise Computer Controlled DC Voltage Source** 33
3.1 Introduction 33
3.2 Theory 35
3.3 Circuit Design 37
3.4 Result and Discussion 45
3.5 Application 47
3.6 Conclusion 48

4. **All Digital Universal Automatic Relockable Servo Controller: FPGA Based Lock-in Amplifier & PID Systems** 51
4.1 Introduction 51
4.2 Design 54
4.2.1 Hardware 54

4.2.2 Firmware . . . 56
4.2.3 Graphical User Interface . . . 62
4.3 Characterization and Discussion . . . 63
4.4 Laser frequency stabilization . . . 68
4.5 Auger electron spectroscopy . . . 72
4.6 Low coherence optical tomography . . . 73
4.7 Conclusion . . . 73

5. **Frequency Stabilization of Multiple Laser Wavelengths to a Common Atomic Reference via Transfer Cavity Locking** . . . 75
5.1 Introduction . . . 75
5.2 Theory . . . 77
5.3 Experimental requirements . . . 78
5.4 Experimental setup . . . 80
5.5 Results and Discussion . . . 84
5.6 Conclusion . . . 95

6. **Computer Controlled Radio Frequency Drivers for Acousto and Electro Optical Modulators (AOM & EOM)** . . . 97
6.1 Introduction . . . 97
6.2 Theory . . . 98
6.3 Circuit Diagram for RF drivers . . . 100
6.4 Result and Discussion . . . 106
6.5 Conclusion . . . 110

7. **Conclusion and Outlook** . . . 111

Bibliography . . . 115

Publications . . . 127

List of Figures

1.1 Laboratory view of the Yb-ion optical clock at CSIR-NPL 4
1.2 Projected evolution of commercial atomic clocks those are either presently . . . 6
1.3 Energy level diagram of Yb ion, where we show all transitions that can be . . . 8

2.1 Energy level diagram of Yb^+: All the clock transitions and low-lying states . . 19
2.2 Wavelength dependent dynamic dipole polarizabilities of the $[4f^{14}6s]\ ^2S_{1/2}$ . . . 26
2.3 Dynamic scalar polarizabilities of the $[4f^{14}6s]\ ^2S_{1/2}$ and $[4f^{14}6s]\ ^2D_{3/2}$ states . . 30

3.1 A schematic of our experiment which shows the requirement of automation . . 34
3.2 (a)Block diagram of discrete transistor shunt voltage regulator use for 35
3.3 Circuit diagrams for: (a) generating unique individual address for an 38
3.4 (a) Schematic of DACM which is designed in Eagle v6.4 and Populated PCB . 39
3.5 Schematic of power supply section used to design low noise voltage source. . . . 40
3.6 (a) Schematic of voltage source which is designed in EAGLE V6.4 software . . 41
3.7 Behavior of a digital BUS (black; red; green; blue) which is propagated 42
3.8 Change of voltage source output with the reference voltage which is tuned . . . 44
3.9 Stability of the output after starting the voltage source (black) and after . . . 46
3.10 Characteristic load regulation of the voltage source. The critical load below . . 48
3.11 (a) Characteristics of the switching on (red)/ off (black) of the voltage 49
3.12 Example waveforms: sinusoidal (red), triangle (green), sawtooth (purple) . . . 50

4.1 (a) Block diagram of the instrument showing constituent of the external . . . 52
4.2 (a) Populated PCB of analog interface board between analog signals and . . . 55
4.3 Simulation results showing a Lorentzian signal with (Magenta) and without . . 58
4.4 The graphical user interface (GUI) panel for remote operation of the 62
4.5 Frequency response of the first (green), second (magenta), third (cyan) and . . 63
4.6 (a)Schematic of optical setup for Rb saturation absorption spectroscopy 64
4.7 (a) Characteristic response of the type-C PID (green) due to insertion of a . . . 65
4.8 (a) Doppler broadened Rb-Saturation absorption spectrum consisting 69
4.9 Slope of error signal changes with respect to change in modulation 70
4.10 Noise Spectral Densities of input signal (grey) and Lock-in amplifier's 71

4.11 Measured signal showing performance of the instrument in Auger 72
4.12 Measured signal showing performance of the instrument in Low coherence . . . 73

5.1 Block diagram of the transfer cavity locking, where λ_R is the reference 76
5.2 (a) 780 nm reference laser, (b) Slave laser 760 nm/ 935 nm (c) 739 nm 79
5.3 Optical setup for transfer cavity locking consisting of SAS and FP cavity . . . 81
5.4 Block diagram of servo controller used for transfer cavity locking technique . . 83
5.5 (a) Optical setup of transfer cavity locking and for tuning the length of 84
5.6 (a) Wavelength meter data shows the steps for laser frequency stabilization of . 85
5.7 Error signal generation from SAS (red), transmission mode of the cavity for . . 87
5.8 The mode of the slave laser (green) follows that of the reference laser (red) . . 89
5.9 Power spectral density of error signal in locked condition for SAS signal 90
5.10 Tunability of slave laser obtained by scanning part of the reference laser 91
5.11 Increase in tunability range of the slave laser (green) by side of the fringe . . . 93
5.12 Frequency drift of reference laser (Red) and Slave laser (Green) 94

6.1 Schematic of frequency modulation using (a) AOM and (b) EOM. In 98
6.2 (a) Block diagram of AOM RF driver circuit used to modulate light 99
6.3 (a) Schematic and (b) populated printed circuit board of an RF driver for . . . 102
6.4 (a) Block diagram of EOM RF driver and (b) the developed hardware 103
6.5 (a) Schematic and (b) populated PCB board for the EOM RF driver 104
6.6 (a) Tuning VCO frequency with respect to the voltage given at the control . . 107
6.7 (a) Tuning VCO frequency with respect to voltage given to control pin 109

List of Tables

1.1 Energy levels and their spectroscopic information that are relevant for our . . . 9

2.1 Contributions to the static values of $\alpha_{J_n}^{(i=0,2)}$ for the $[4f^{14}6s]\ ^2S_{1/2}$ and 24
2.2 The λ_{magic} values in nm and their corresponding α_{F_n} values in a.u. values . . . 28
2.3 The λ_{T} values in nm for all possible M_F components of the considered 29
2.4 Summarized values for BBR and polarizabilities of the clock states 31

3.1 Truth table of DEC-1 when $\{\overline{\text{E}}_{i1}; \overline{\text{E}}_{i2}; \overline{\text{E}}_{i3}\}$ operates at $\{0; 0; 1\}$ 37
3.2 Bill of materials to construct the DACM and voltage source 43

4.1 List of items required and the parts number that we made for designing 57
4.2 Values of coefficients and total bits allocated to parameters associated with . . 59
4.3 Values of coefficient in different PID types 61
4.4 Specification of our FPGA based frequency generator, lock-in amplifier and . . 66
4.5 Comparison of our module to different commercially available devices 67

5.1 Comparison of parameters measured experimentally for optical cavity 86
5.2 Measurement of linewidth of lasers after locking in transfer cavity system . . . 95

6.1 List of items required for fabricating the RF driver for AOM following the . . . 101
6.2 List of items required for designing RF driver for driving the EOMs 105

Chapter 1

Introduction

Measurement of any physical quantity is important from the viewpoint of establishing a clear understanding of a particular phenomena. For measuring various physical quantities, there are seven basic International system of units (SI units) [1]. Each of the SI units are referenced with respect to constants such as, for mass and temperature has units kilogram and Kelvin that are referenced to the Planck and Boltzmann constants, respectively [1]. Among these seven SI units, "second" is one of the most important one because it is not only used for measuring time or frequency but it also defines references for other SI units [1]. Due to this reason, defining reference for time & frequency standard is crucial for scientific measurement and advanced technology. For maintaining time & frequency standard, atomic clocks are used where oscillator frequency is measured with respect to an atomic transition frequency. In case of Caesium atomic clocks, transition frequency (9.192631770 GHz) between ground state hyperfine levels of ^{133}Cs is used as a reference frequency that defines one second in SI unit [1]. The Cs-based microwave clock provides a stable frequency with a fractional uncertainty of 10^{-16} [2]. So far, time can be measured most accurately among all other SI units. The evolution of science and technology demands more accurate clock for different applications such as, global navigation satellite system, radio telescope based on very long baseline interferometry, probing fundamental science, communication system, smart power grids, quantum communication, cyber securities, *etc.* [3]. Performance of a clock is defined by its "stability" and "accuracy". For that Allan deviation is a measure to characterize clock's performance. The Allan deviation of an atomic clock is defined by the equation [4]

$$\sigma(\tau) = \frac{\Delta\nu}{\nu_\circ} \times \sqrt{\frac{T_c}{N\tau}}, \tag{1.1}$$

where $\Delta\nu$ is measured linewidth of the atomic transition, $\nu_\circ$ is the transition frequency, N is number of species probed in a single measurement, T_c is time required for a single measurement and τ is the measurement period. The stability of atomic clock thus becomes better with an increased quality factor $\nu_0/\Delta\nu$ of the oscillator and a better signal to noise ratio $\sqrt{\frac{T_c}{N\tau}}$. Of

Fig. 1.1: Laboratory view of the Yb-ion optical clock at CSIR-NPL

these two parameters, increment in quality factor is achieved by using an optical frequency at few hundreds of THz rather than microwave frequency (GHz). The natural linewidths are narrow or ultra-narrow due to choice of forbidden or highly forbidden transitions. Sometimes, $\Delta\nu$ is limited by linewidth of the probe lasers than the linewidth of the transition. This leads to a 1000 times improvement in the quality factor. This has motivated us towards developing an optical atomic clock to improve the time and frequency metrology in India and stay at par to the international standard. At present, the best existing optical atomic clock gives a stable reference frequency with a fractional uncertainty of 10^{-18} [5] which is 100 times better than the microwave laser cooled Cesium based clocks. The evolution of optical clocks begun after the invention of frequency combs which aids in measuring optical frequency in a very stable manner and also produces multiple reference frequencies [4]. Developing an optical atomic clock eventuates from trapping atoms or ion in a well characterized and controlled environment followed by reduction of their thermal energy using laser cooling. Once the secular motion of the trapped species is minimized, the clock transition is probed using a laser, then the resulting spectroscopic signal is used as feedback to stabilize the clock laser frequency. The stabilized laser frequency is up/down-converted using combination of optical frequency comb and electronic hardware to finally use it for defining 1 second or use its different frequencies as reference for other applications [4].

The optical atomic clocks are mainly divided into two types on the basis of trapped species. Optical lattice clock that is based on trapped atoms in an optical lattice and the other one is trapped ion optical clock based on single ion trapped using electric field [6]. Both types of clock have their own advantage/disadvantage, which brings various challenges to the experimentalist in building a precise optical atomic clock. The optical lattice clock has a better signal to noise (S/N) ratio because of larger number of trapped atoms as compared to the single ion based atomic clock. Optical clock based on single ion allows longer measurement time than the lattice clock because a single ion is isolated from external environmental interaction and stored within the trap for much longer period [4], whereas in lattice clock, there is a possibility of atom-atom interaction that affects the reproducibility of the measurement. Low laser power is required in ion based clocks while periodically arranged potentials for trapping neutral atoms in optical lattice clocks require high power lasers [7]. As a result of that total power consumption in the setup is much lower, which suits for specific applications like space grade clock. Other than that, the trapping of ion and controlling its motion is comparatively easier than manipulating large number of neutral atoms. Miniaturization of ion based optical clocks is possible because of its less complex experimental requirements and rather simple design as compared to higher complications in lattice clocks. The lifetime of trapped ion is very large than that of trapped atoms, which decreases the time period of use of atomic reservoir in ion-trap based clocks. The low S/N ratio in ion based clock is possible to overcome by using low noise detector, e.g., CCD

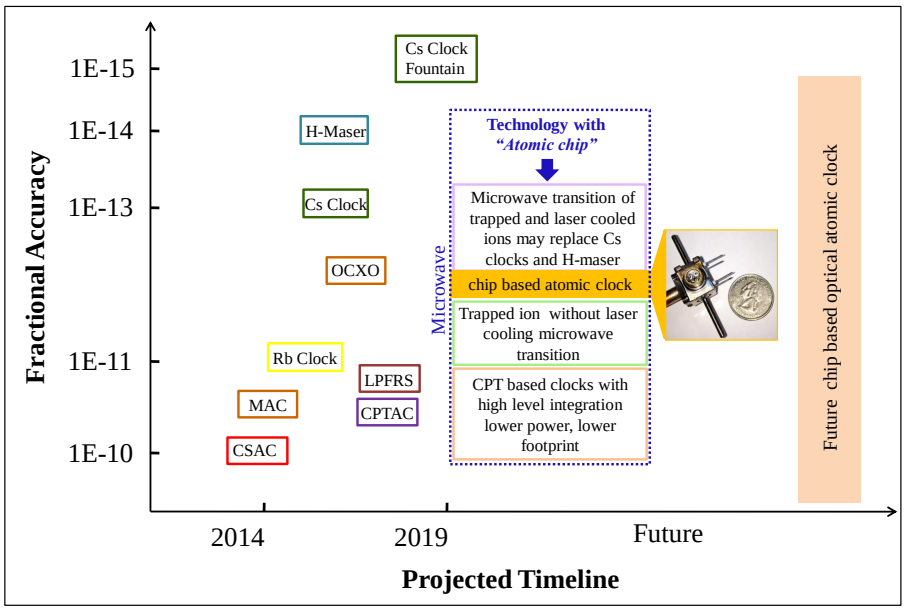

Fig. 1.2: Projected evolution of commercial atomic clocks those are either presently available or in the development phase.

cameras and photo multipliers together with high resolution imaging objective. Also, in future there might be a concept of hybrid trap [8] which will assemble the technique of trapping by electric fields and optical lattice to trap multiple ions for good S/N ratio. There is a possibility of new generation of commercial optical clocks using single or multiple ion traps, which may be used in applications requiring lesser accuracy but higher than the present microwave based atomic clocks [9, 10]. The possibilities and present scenario for new kind of chip based atomic clock are presented in Fig. 1.2. It is desired that small and chip based optical atomic clocks will be used in satellite systems for more accurate time synchronization. A review on different types of singly charged trapped ion optical clocks together with their advantages, disadvantages and scientific potentials are described in our earlier publication [11]. At CSIR-NPL, which is the metrology institute of India, we are developing an optical atomic clock based on single, laser cooled Ytterbium-171 ion. In Fig. 1.1, actual picture of the Yb ion optical clock laboratory is depicted. This work is motivated to meet the future needs of the high end technologies and uplift our nation at par to the international standard as there is always a requirement of better clock for scientific experiments and technology demands. The objective of our experiment is to trap a single Yb ion (Yb^+) for optical frequency standard, which may be used as secondary time & frequency standard until redefinition of the second in SI unit system.

1.1. Ytterbium-ion optical frequency standard

In optical atomic clock, choice of the technique to probe clock transition is not the only parameter which decides the stability of the reference frequency generation. The choice of species whose one of the forbidden optical transition we want to trap and probe, is the crucial part of the experiment. The choice of the experimental species depends on many parameters such as, life time of the clock states, commercial availability of lasers used in experiment, ionization potential of the neutral atom, sublimation energy requirement for atomic vapour, percentage of insensitiveness of the clock states in presence of external perturbation and so on. Considering all these parameters, and viability of creating an optical atomic clock international committee for weights and measures (CIPM) listed few atoms and ions [12], whose clock transitions may be used for redefinition of the SI second. Among these listed atoms and ions, we choose Yb^+ and use its clock transition as reference to build optical atomic clock. To excite various transitions of Yb^+, it requires lasers at wavelengths 399 nm, 369 nm, 935 nm; 760 nm and 467 nm for ionizing, cooling, repumping and probing clock transition, respectively [13]. These lasers and their respective optics are easily commercially available. RF based endcap quadrupole ion trap are the suitable ones for trapping single ion as they provide enough optical access to the trap centre , which is required for shining all different lasers [14]. For trapping and probing single ion in isolation, ultra high vacuum on the order of 10^{-12} torr is required. In this range of vacuum, remaining hydrogen atoms chemically react with Yb^+ and form hydride which decreases the life time of the trapped ion. However, using Yb^+ is advantageous as ytterbium hydride easily photodissociates to Yb^+ in presence of cooling laser at 369 nm and gets retrapped [15]. This makes Yb^+ a better candidate for ion based atomic clock as the frequent ion loading is not needed. Yb^+ provides three different clock transition states with life times 7.2(3) ms [16], 61(6) ms [17] and about 8.4 year [18] with an additional microwave clock transition between hyperfine doublet ground states at 12.6 GHz [19], which is one of the primary reasons to choose Yb^+ for our experiment. The energy level diagram of Yb^+ indicating all clock transitions, E1 transitions used for cooling and repump transitions are shown in Fig. 1.3. Various perturbations occurring around the trapped ion results in shift in the clock states and creates uncertainty in the measurement. Some of these systematic shifts are electric field leading to Stark shift, Black Body Radiation shift, light shift, effect of magnetic field causing Zeeman shift, second order Doppler shift and *etc.* Such shifts arising from various sources are called systematic shifts of the atomic clock. We choose ^{171}Yb isotope because it has a nuclear spin $I = 1/2$, which couples with the electron spin and produces F = 0 hyperfine sublevels at both ground and excited states associated to the clock transition. As a result of that the clock transitions are insensitive to the first order Zeeman shift. Trapped Yb^+ based clock is widely used for many other experiments like formation of qubits [20] and for measuring temporal consistency of the fundamental constants. Yb^+ and its clock transition $|^2S_{1/2}, F = 0\rangle \rightarrow |^2F_{7/2}, F = 3\rangle$ is more

sensitive for the measurement of consistency of the Fine structure constant [21, 22]; it is in fact 100 times more sensitive than Sr based best optical lattice clock [23]. In addition to this, $|^2F_{7/2}, F = 3\rangle$ state has large enhancement for measuring violation of local Lorentz symmetry [24]. These promote Yb^+ as the suitable candidate for our experiment which allows to study wide variety of physics problems.

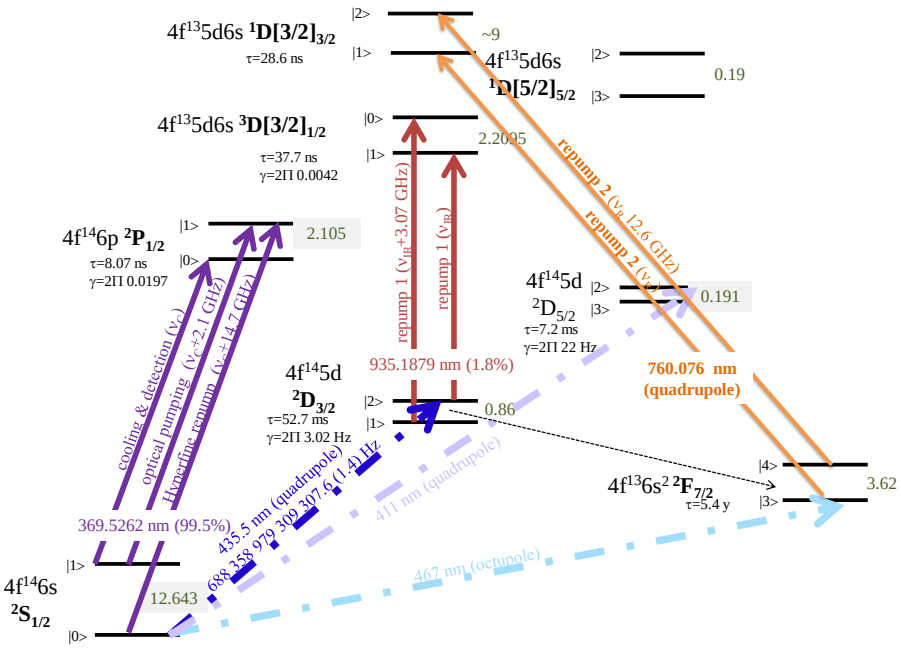

Fig. 1.3: Energy level diagram of Yb ion, where we show all transitions that can be used for laser cooling and clocks. Splitting between hyperfine states are given in GHz.

We are setting up Yb^+ clock experiment at the 467 nm $|^2S_{1/2}, F = 0\rangle \rightarrow |^2F_{7/2}, F = 3\rangle$ electric octupole clock transition. Starting point of our Yb^+ based experiment is its production. In the presence of 399 nm and 369 nm lasers, the outer electron of the Ytterbium atom gets excited and stripped off from the atomic potential, thus photoionizing it and producing Ytterbium ions. Once the atoms get ionized, they get trapped in the harmonic potential generated by combination of AC and DC electric fields. Using 369.5 nm, the E1 transition between ground $|^2S_{1/2}, F = 1\rangle$ to $|^2P_{1/2}, F = 0\rangle$ states is used for laser cooling and probing ions by fluorescence measurement. From the excited $|^2P_{1/2}, F = 0\rangle$ state, there is a finite probability of the ion leaking from the cooling cycle and getting de-excited to $|^2D_{3/2}, F = 1,\ 2\rangle$ or $|^2F_{7/2}, F = 3,\ 4\rangle$ states, which have longer lifetimes. As a result of that the laser cooling of the ion stops. To pump the ion back to the cooling cycle, additional repump lasers of wavelength 935 nm and 760 nm are used to create a closed cycle. When ion goes back to the ground state, there is a finite probability of the ion reaching to another hyperfine ground state $|^2S_{1/2}, F = 0\rangle$. To overcome

Tab. 1.1: Energy levels and their spectroscopic information that are relevant for our experiment.

Energy states	Δ E (cm^{-1})	A_{ik} (s^{-1})	Life time	Hyperfine splitting (GHz)	References
$\|4f^{14}6s\ ^2S_{1/2}, F = 0, 1\rangle$	-	-	-	12.645(2)	[20]
$\|4f^{14}6p\ ^2P_{1/2}, F = 0, 1\rangle$	27 061.82	1.23×10^8	8.07(9) ns	2.105(1)	[25, 26]
$\|4f^{14}5d\ ^2D_{3/2}, F = 1, 2\rangle$	22 960.80	16.39	61(6) ms	0.86(2)	[17, 20]
$\|4f^{14}5d\ ^2D_{5/2}, F = 3, 2\rangle$	24 332.69	138.89	7.2(3) ms	0.1909(2)	[16, 27]
$\|4f^{13}5d6s\ ^3D[3/2]_{1/2}, F = 0, 1\rangle$	33 653.86	2.61×10^7	37.7(5) ns	2.210(1)	[28]
$\|4f^{13}5d6s\ ^1D[3/2]_{3/2}, F = 0, 1\rangle$	34 575.37	3.42×10^7	28.6(1) ns	9.1(1)	[29]
$\|4f^{13}5d6s\ ^2F_{7/2}, F = 3, 4\rangle$	21 418.75	-	8.4 year	3.62(1)	[18, 29]

this, we use 369 nm + 14.7 GHz as hyperfine repump which brings the ion back from F = 0 to F = 1 state of the ground level. For similar reasons, we require sidebands of the repump lasers too, such as additional laser frequencies at 935 nm + 3.07 GHz, and 760 nm + 12.6 GHz. The shift in frequency of the laser light is done by optical modulators like Acousto optic modulator (AOM) and Electro optic modulator (EOM). Subsequent to laser cooling, the next process is state preparation in which we use 369.5 nm + 2.1 GHz laser frequency in presence of repump lasers to optically pump the ion at the ground state $|^2S_{1/2}, F = 0\rangle$, so that the clock transition is ready to be excited using 467 nm laser. During driving of the clock transition, the cooling laser together with the 760 nm repump lasers are also operating to ensure excitation of the clock transition by electron shelving technique. Absence of any fluorescence signal at this stage ensures that the probed clock laser frequency is equal to the Yb^+ clock transition. As previously mentioned, Yb^+ affords three different clock transitions which are $|^2S_{1/2}, F = 0\rangle \rightarrow |^2F_{7/2}, F = 3\rangle$ (E3), $|^2S_{1/2}, F = 0\rangle \rightarrow |^2D_{3/2}, F = 2\rangle$ (E2) and $|^2S_{1/2}, F = 0\rangle \rightarrow |^2D_{5/2}, F = 2\rangle$ (E2'). Among these three transitions only E3 and E2 clock transitions are favorable for generating stable frequency source because of their long life times hence low natural linewidths of 3 Hz and 3 nHz, respectively. In our experiment, we are interested about the E3 transition. The details of energy levels and relevant spectroscopic information which will be used to develop optical atomic clock are tabulated in Tab. 1.1.

1.2. Experimental challenges

To setup the described trapped ion optical frequency standard, we have mainly five leading challenges to be effectuated: achieving ultra high vacuum, designing and developing of a precision ion trap, electronic instrumentation, optical setups and stabilized ultra narrow clock laser. Each of these requisites are further assortment of several building blocks which are challenging to develop and construct. In our experiment, we aim for achieving ultra high vacuum of the order of 10^{-12} mbar, which is desired for increasing the trapping lifetime. To achieve this order of vacuum requires several different vacuum pumps like turbo pump, ion pump and Ti-sublimation pump along with proper choice of metals, electroplating and baking of the system for the vacuum chamber. The design and fabrication of a precision ion trap is also challenging because an inaccurate design will introduce trap induced systematic shifts to the clock transition. A detailed calculation is thus necessary prior to designing of the trap. Confinement of ion using the trap requires a high voltage RF with nearly-absent higher order harmonics, with which the trap electrodes are biased to create a quadrupole trapping potential. We also require a low noise DC voltage source for biasing compensation electrodes to control the ion motion. There is also a requirement of an atomic oven which would provide nearly collimated beam of neutral atoms to be ionized and trapped at the trap centre. Here, the challenge is to design an oven which produces less divergent atomic beam with small cross section so that no patch potential is created due to atoms sticking to the electrodes. Otherwise, a quadrupole shift produced due to this patch potential will lead to an inaccurate measurement of the clock frequency.

The heart of the optical frequency standard is the lasers which are used in the experiment for ionization, cooling, repumping and clock transition probing and thus stabilization of the laser frequencies are essential. The stabilization of ionizing, cooling and repump lasers require a servo controller to lock its central frequency with respect to a reference point and to prevent the system from electronic pickup noises which brings destabilization in laser frequency. The reference point is generally an atomic transition spectra in saturation absorption spectroscopy or a stabilized Fabry perot cavity with respect to any reference laser frequency. Stabilization of clock laser requires extra effort as the narrow linewidth of the probing transition demands a narrow and stable probing frequency. An ultrastable reference point in the form of peak of a transmission/reflected mode from a high finesse Ultra Low Expansion (ULE) optical cavity is utilized. Long term frequency stabilization of these lasers during experiment is an important requisite. The designing of low noise and fast servo controller for stabilizing the laser frequency is therefore essential. The servo controller is an assemble of many sophisticated electronic modules like function generator, lock-in amplifier, PID controller. All these modules require high bandwidth and low noise for stabilizing laser frequency of the clock laser and moderate bandwidth for other lasers as per our experimental requirement. Optical setup for

laser locking requires modulation in laser frequency, which is done by Acousto and Electro optical modulators. These modulators require low noise, stabilized and additionally computer controlled RF drivers to fulfill our experimental requirements. Stabilization of laser intensities is also an important part and this is dealt with using AOM and RF drivers which require additional feedback control of the RF power. In the overall experimental process, we require five different lasers, ten optical modulators and few mechanical shutters for providing correct frequency at a correct sequence during the experiment at run. For generating correct frequency during experiment, we have to stabilize laser with respect to different references like ionizing laser is stabilized using wavelength-meter, cooling and repump lasers are stabilized by transfer cavity locking technique using Rb transition spectra. The stabilizing of clock laser requires an extra effort for generating ultra-narrow linewidth & ultrastable frequency using ULE cavity and fast servo controller. Also correct optical modulation and correct sequencing for shutters' operation are required to stabilize their drivers using reference frequency from commercial atomic clocks. Hence, time difference between each events during cooling and probing clock transition is so fast that it is not desired to operate whole system manually, which creates a requirement of a precise automation unit for controlling system through computer. For this, we need to have control on tuning the laser frequencies, fast switch -on-off of the laser light, DC voltage on compensating electrodes, control on magnetic field at different stages, atomic oven ON/OFF timing and recording of the data from different sources. There is also requirement of choice of communication protocol between computer and electronic modules so that we minimize the processing delays during data transfer. This thesis describes many of these mentioned instrumentation which were worked upon during pursual of my PhD thesis.

1.3. Objective and outcome of the thesis

Developing the Yb^+ optical atomic clock is an ensemble of many different blocks, such as, theoretical calculations, wide range of instrumentation and finally meaningful analysis of data. In case of a precision spectroscopy, many systematic shifts due to quantum perturbations increase the uncertainty budget which had to be eliminated or corrected. Due to this reason, complete theoretical knowledge about the systematic shift is imperative in addition to finding feasible solution to minimize the effect of the shifts to help in accurate frequency measurement. Based on our experimental purpose, many instrumentations such as mechanical shutters, current source, voltage source, AOM/EOM drivers, magnetic shielding coils, optical systems, *etc.* are also part of the experiment. Controlling a wide range of such modules in simultaneous and synchronous manner require an automation of the experiment. Developing of a trapped ion optical frequency standard is long term goal of the lab. Within that frame work, the described work in this thesis starts with theoretical calculation of the photon assisted systematic shifts and then describe about the automation and indigenously developed instruments like voltage

source, address module, servo controller and RF drivers. We also describe a novel technique to generate reference point for stabilizing laser frequencies which are required in this experiment.

In Chapter 2, we are focusing on the Yb-ion system and used various theoretical tools such as, relativistic coupled-cluster (RCC) method and relativistic many-body perturbation theory (MBPT) to calculate the electric dipole (E1) transition matrices associated to ground and excited states of the clock transition. Finally, using the results obtained by these methods, *i.e.* wave function of the desired states, we calculate ac and dc polarizabilities of the states associated to the clock transition. Magic and tune-out wavelengths have been estimated that could be of interest to cancel out light shifts. Magic wavelength are useful to construct array of Yb-ions stored in an optical lattice where the clock transition frequency remains unperturbed. As application of this calculation, it gives values of polarizability and estimate BBR shift which is one of the major contributors in systematic shifts.

In Chapter 3, we describe the address module used for automation in our experiment. This module is hooked up with every indigenously developed electronic instruments so that they can be controlled via a computer. This module provides unique address to each instrument so that all can be controlled using a universal data bus thus avoiding the mess of wires around the experimental setup. We have developed a computer controlled, regulated DC voltage source for biasing the compensating electrodes and controlling the ion position. Such computer controlled ultra-stable high voltage sources tunable to any arbitrary waveforms at low frequencies have many other applications as well. Details of the DC source is also described in this chapter.

In Chapter 4 , we describe indigenously developed servo controller for laser frequency stabilization. Such a servo system requires function generator, lock-in amplifier and PID controller for laser frequency stabilization to an absolute reference. These modules are programmed on an FPGA using VHDL language. The developed integrated digital servo controller is very compact, portable and also free from any electronic pickup noise. Characterization of the modules in terms of filter frequency response, PID bandwidth *etc.* are done using different measuring instruments. We have also added an auto relock mechanism to our PID module which makes the instrument smart and efficient. Using our developed algorithm, the system itself monitors its stability and in cases of slipping from the lock point, it automatically searches and relocks to the setpoint.

In Chapter 5, we have developed optical setups for providing absolute reference point with respect to an atomic transition to the servo controller to lock laser frequency. In our experiment, for photoionization and repump lasers at 935 nm and 760 nm wavelength no such atomic references are available so that simple pump-probe spectroscopy can be done for locking these

lasers. We use wavelength meter for locking photoionizing laser as it requires only short term frequency stability. For repump lasers, we use transfer cavity locking technique where we first lock a master laser using an atomic transition, with respect to which the Fabry-Perot cavity is stabilized. The stabilized cavity transmission spectrum is then used as a reference for the repump lasers for locking their frequency. In this technique, the stability of master laser is transferred to slave laser through an intermediate Fabry Perot cavity.

We require several laser beams at shifted frequencies to drive multiple transitions between different hyperfine levels, which is done using AOMs and EOMs. These modulators require stabilized RF sources within the range 80 MHz to 3 GHz to drive them. In chapter 6, we describe the design, working principle and characterize these drivers.

Finally in Chapter 7, I give conclusion of this thesis and possible future works towards developing Yb-ion optical frequency standard.

Chapter 2

Polarizability, Magic and Tuneout Wavelength Calculation of Yb^+ Clock Transition

Publication: A. Roy, S. De, Bindiya Arora and B. K. Sahoo, Accurate determination of blackbody radiation shift, magic and tune-out wavelength for the $6S_{1/2} \rightarrow 5D_{3/2}$ clock transition in Yb^+, J. Phys. B: At. Mol. Opt. Phys. **50**, 205201 (2017).

2.1. Introduction

Trapped and laser cooled ions are exciting for studying wide variety of quantum mechanical phenomena such as simulating many-body systems, computation and information processing, quantum sensors and metrology. Since invention of the Paul and Penning traps, enormous efforts have been made for studying such phenomena using trapped ion systems where laser cooling enhances possibility of probing the quantum dynamics by overcoming thermal energy of the ions. Optical trapping of ions and storing them in optical lattices have been less investigated so far as compared to the neutral atoms and are promising since micromotions are not present there, which is otherwise unavoidable in any electrodynamic trap. Ions stored in an optical lattice can be manipulated to different geometries such as linear chain, zig-zag ladder, triangular and so on, which opens up possibility of studying novel quantum phases [30], realization of micro-trap systems for quantum information processing [31], [32], effective spin-spin interaction mediated by long range Coulomb interaction and quantum magnetism in an ion chain [33], [34]. In our experiment, we use Ytterbium-ion (Yb^+) for trapping and probing its clock transition. The two quadrupole (E2) transitions, $[4f^{14}6s]\ ^2S_{1/2} \rightarrow [4f^{14}5d]\ ^2D_{3/2}$ and $[4f^{14}6s]\ ^2S_{1/2} \rightarrow [4f^{14}5d]\ ^2D_{5/2}$, and one octupole (E3) transition, $[4f^{14}6s]\ ^2S_{1/2} \rightarrow [4f^{13}6s^2]\ ^2F_{7/2}$, of Yb^+ as shown in Fig. 2.1 are being undertaken for the optical frequency standards [35, 36, 37, 38, 5]. In this chapter, we have shown the possibilities of multiple ions trapped in optical lattice to probe one of its clock transition $[4f^{14}6s]\ ^2S_{1/2} \rightarrow [4f^{14}5d]\ ^2D_{3/2}$. The possibilities of building such a system is judged by its systematics shifts, which creates uncertainties in the frequency measurements. For precise frequency measurements, knowledge of the major source of systematics shifts like

differential black-body radiation (BBR) shifts and light shifts are important. Theoretical estimation of these shifts are crucial factors for deciding the uncertainties of the clock transitions. Accurate estimation of these quantities demands a reliable knowledge of the scalar components of the static polarizabilities. Precise values of the static scalar polarizabilities of the atomic states associated with the $[4f^{14}6s]\ ^2S_{1/2} \rightarrow [4f^{14}5d]\ ^2D_{3/2}$ clock transition in Yb^+ is required in calculation of light shift of clock state which gives information regarding reduction of this effect using a specific wavelength called magic wavelength. At this wavelength, the differential shift of ground and excited state of a clock transition goes to zero. The uncertainty in our measurement due to this shift reduces if we get correct knowledge about the geometry of the lattice used for trapping multiple ions. In this chapter, we describe thoroughly about the calculations used for polarizability and coulomb shift, which gives evidence of the possibilities of multiple Yb^+ trap in optical lattice for the $[4f^{14}6s]\ ^2S_{1/2} \rightarrow [4f^{14}5d]\ ^2D_{3/2}$ clock transition. This might open up developing multi-ion optical clock in future as this is of interest within the community [39] .

2.2. Theory of polarizability

In an atomic energy state, the Stark shift of the n^{th} hyperfine level with angular momentum F_n and its magnetic component M_{F_n} is introduced when it is placed in a uniform oscillating electric field of a laser beam

$$\mathcal{E}(t) = \frac{1}{2}\mathcal{E}\hat{\varepsilon}e^{-(\iota\omega t - \mathbf{k}.\mathbf{r})} + c.c., \tag{2.1}$$

with $\mathcal{E}$ being the amplitude, $\hat{\boldsymbol{\varepsilon}}$ is the polarization vector of the electric field and *c.c.* referring to the complex conjugate of the former term and oscillating at frequency ω given by

$$\Delta E_{F_n}^{\text{Stark}} \approx -\frac{1}{4}\alpha_{F_n}(\omega)\mathcal{E}^2, \tag{2.2}$$

where $\alpha_{F_n}(\omega)$ is the frequency dependent or dynamic polarizability of the state and is given by

$$\begin{aligned}\alpha_{F_n}(\omega) &= \alpha_{F_n}^{(0)}(\omega) + \alpha_{F_n}^{(1)}(\omega)\frac{A\cos\theta_k M_{F_n}}{2F_n} + \alpha_{F_n}^{(2)}(\omega)\left(\frac{3\cos^2\theta_p - 1}{2}\right) \\ &\quad \times \left[\frac{3M_{F_n}^2 - F_n(F_n+1)}{F_n(2F_n-1)}\right].\end{aligned} \tag{2.3}$$

Here $\alpha_{F_n}^{(i)}(\omega)$ are the scalar, vector and tensor components of the frequency dependent polarizability for i = 0, 1, and 2 respectively, A represents degree of polarization, θ_k is the angle between quantization axis and wave vector, and θ_p is the angle between quantization axis and direction of polarization. In presence of magnetic field, $\cos\theta_k$ and $\cos^2\theta_p$ can have any values

depending on the direction of applied magnetic field. In absence of magnetic field, $\cos\theta_k = 0$ and $\cos^2\theta_p = 1$ for linearly polarized light, where polarization vector is assumed to be along the quantization axis. However, it yields $\cos\theta_k = 1$ and $\cos^2\theta_p = 0$ for circularly polarized light, where the wave vector is assumed to be along the quantization axis. Here, we present results for both polarizations of the light assuming absence of the magnetic field. The component of the polarizability can be expressed as [40, 41].

$$\alpha^{(0)}_{F_n}(\omega) = \alpha^{(0)}_{J_n}(\omega), \tag{2.4}$$

$$\alpha^{(1)}_{F_n}(\omega) = (-1)^{J_n+F_n+I+1}\left\{\begin{array}{ccc} F_n & J_n & I \\ J_n & F_n & 1 \end{array}\right\}\sqrt{\frac{F_n(2F_n+1)(2J_n+1)(J_n+1)}{J_n(F_n+1)}} \times \alpha^{(1)}_{J_n}(\omega) \tag{2.5}$$

and

$$\alpha^{(2)}_{F_n}(\omega) = (-1)^{J_n+F_n+I}\left\{\begin{array}{ccc} F_n & J_n & I \\ J_n & F_n & 2 \end{array}\right\}\sqrt{\frac{F_n(2F_n-1)(2F_n+1)}{(2F_n+3)(F_n+1)}} \times \sqrt{\frac{(2J_n+3)(2J_n+1)(J_n+1)}{J_n(2J_n-1)}}\,\alpha^{(2)}_{J_n}(\omega) \tag{2.6}$$

Here, J_n is the total angular momentum of the atomic state, I is the nuclear spin and $\alpha^{(i)}_{J_n}$ for i = 0, 1, 2 are the scalar, vector and tensor components of the atomic dipole polarizability. Mathematical expressions of these polarizability components as discussed in Ref. [42], are given as,

$$\alpha^{(0)}_{J_n}(\omega) = \frac{2}{3(2J_n+1)}\sum_{k\neq n}\frac{(E_n-E_k)|\langle J_n||\mathbf{D}||J_k\rangle|^2}{\omega^2-(E_n-E_k)^2}, \tag{2.7}$$

$$\alpha^{(1)}_{J_n}(\omega) = \sqrt{\frac{24J_n}{(J_n+1)(2J_n+1)}}\sum_{k\neq n}(-1)^{J_n+J_k}\left\{\begin{array}{ccc} J_n & 1 & J_n \\ 1 & J_k & 1 \end{array}\right\} \times \frac{\omega|\langle J_n||\mathbf{D}||J_k\rangle|^2}{\omega^2-(E_n-E_k)^2} \tag{2.8}$$

$$\alpha^{(2)}_{J_n}(\omega) = \sqrt{\frac{40J_n(2J_n-1)}{3(J_n+1)(2J_n+3)(2J_n+1)}}\sum_{k\neq n}(-1)^{J_n+J_k}\left\{\begin{array}{ccc} J_n & 2 & J_n \\ 1 & J_k & 1 \end{array}\right\} \times \frac{(E_n-E_k)|\langle J_n||\mathbf{D}||J_k\rangle|^2}{\omega^2-(E_n-E_k)^2}, \tag{2.9}$$

where J_m and E_m are the total angular momentum and energy, respectively, for $m = n, k$ states and $\langle J_n||\mathbf{D}||J_k\rangle$ are the reduced E1 matrix elements. The trapped atom is polarised not only by laser field or DC electric field but also due to the oscillation of electric field from black body radiation, which produces a systematic shift called BBR shift. The source of this shift is the temperature at position of the trapped ion which polarizes the atomic state and produces systematic shift. This shift can be reduced by decreasing the environmental temperature, which is a difficult task and other option is to estimate BBR shift value. For calculation of BBR shift, we approximate that, the polarizability of atomic state due to thermal radiation near the atom position is equal to the static polarization. This is because, at nearly room temperature, the thermal radiation frequencies from black body spectrum is very small compared to E1 transition frequencies of Yb ion which are considered in calculations of polarization of atomic states. The expression of BBR shift is [43]

$$\Delta E_F^{BBR} \simeq -\frac{1}{2}(831.9\ \mathrm{V/m})^2 \left[\frac{T(\mathrm{K})}{300}\right]^4 \alpha_{\mathrm{F}}^{(0)}(0)(\mathbf{1}+\eta), \tag{2.10}$$

where η is the dynamic fractional correction factor and is defined as [43]. This dynamic correction comes due to frequency distribution of black body radiation field. To calculate η, we use electric dipole matrix element of that transition, whose contribution is dominant in polarizability calculations.

$$\eta = \frac{(80/63)\pi^2 T^2}{(J_n+1)\alpha_F^{(0)}(0)} \sum_k \frac{|\langle J_n||\mathbf{D}||J_k\rangle|^2}{(E_n-E_k)^3} \left(1 + \frac{21\pi^2T^2}{5(E_n-E_k)^2} + \frac{336\pi^4T^4}{11(E_n-E_k)^4}\right). \tag{2.11}$$

The differential BBR shift of a transition is, thus, the difference of the BBR shifts of the states associated with that transition. We use atomic units (a.u.) throughout the article unless stated otherwise. The α_{F_n} values can be converted from a.u. to Hz $\mathrm{m^2V^{-2}}$ and $\mathrm{Jm^2V^{-2}}$ by dividing with factors 2.48832×10^{-8} and $6.064 \times\ 10^{40}$, respectively. The differential AC-Stark shift for a transition between states with hyperfine moments F and F' is given by

$$\begin{aligned} \delta(\Delta E_{FF'}^{Stark}) &\approx \Delta E_F^{Stark} - \Delta E_{F'}^{Stark} \\ &= -\frac{1}{2}\delta\alpha_{FF'}(\omega)\mathcal{E}^2(\omega). \end{aligned} \tag{2.12}$$

In order to find out λ_{magic} of a transition, it is imperative to identify the corresponding values of ω at which the differential Stark shift $\delta(\Delta E_{FF'}^{Stark})$ is zero for any finite electric field strength $\mathcal{E}$. By suitably choosing polarization of the electric field and azimuthal sublevels, λ_{magic} can be determined for different hyperfine levels of a transition. In fact, we had demonstrated in a

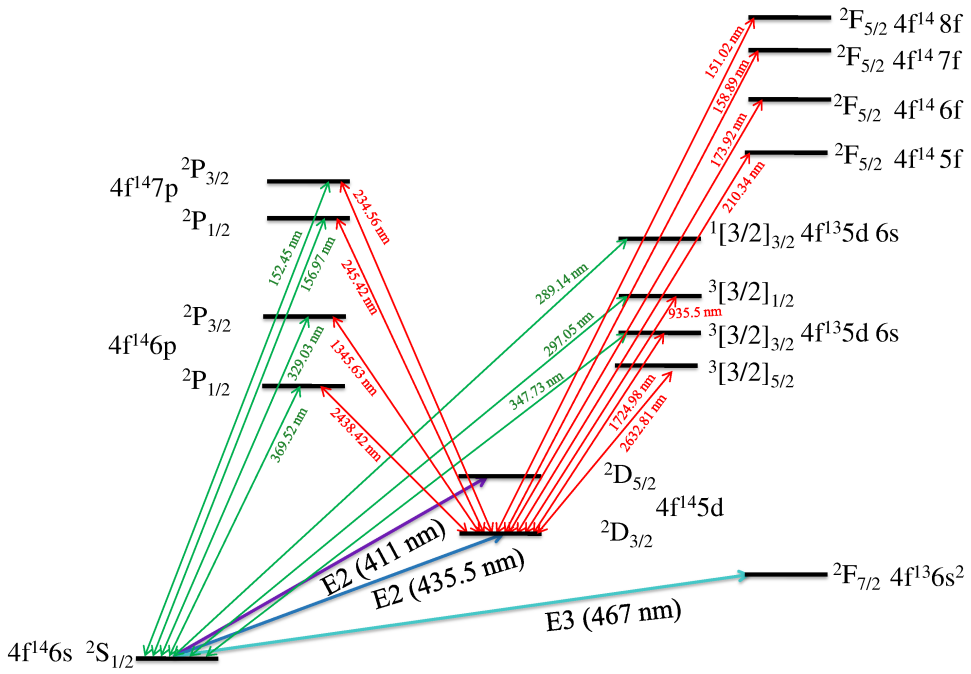

Fig. 2.1: Energy level diagram of Yb^+: All the clock transitions and low-lying states that are relevant for the experimental set-up and demonstrating role of their importance in calculating dipole polarizabilities of the $[4f^{14}6s]\ ^2S_{1/2}$ and $[4f^{14}5d]\ ^2D_{3/2}$ states are highlighted here.

recent work that by suitably deciding a trap geometry, the Stark shift of an atomic state or differential Stark shift of a transition can be obtained which can be independent of the vector and tensor components of the states involved [44]. Assuming that such a trapping configuration can be achieved for trapping the Yb^+ ion, we also give $\lambda_{\rm magic}$ for the aforementioned clock transition. This comprehensive trapping scheme could be useful for avoiding hyperfine level selective trapping of $^{171}Yb^+$. We also evaluate $\lambda_{\rm T}$ values for which $\alpha_F(\omega)$ can become zero independently for the $[4f^{14}6s]\ ^2S_{1/2}$ and $[4f^{14}5d]\ ^2D_{3/2}$ states.

2.3. Method of calculations

When atom is polarized due to electromagnetic wave, the distribution of electrons rotating around the nucleus is changed. Due to this change in configuration of electrons, we divide contribution of each $\alpha_{J_n}^{(i)}$ components broadly into three parts, as described in Refs. [45, 46], which is expressed as

$$\alpha_{J_n}^{(i)} = \alpha^{(i,c)} + \alpha_{J_n}^{(i,cv)} + \alpha_{J_n}^{(i,v)} \quad . \tag{2.13}$$

The superscripts c, cv and v in the parentheses are known as core (independent of J_n), core-valence and valence contributions, respectively [45, 46]. When the core of the electron distri-

bution has an inert gas configuration, core and core-valence contributions usually come out to be much smaller than the valence contribution [47, 45, 46, 48]. This has also been observed earlier in the ground state polarizability study of Yb^+ [48]. Again, it is possible to use the reduced E1 matrix elements among the low-lying bound states directly in Eqs. (2.7-2.9) in a sum-over-states approach to estimate the dominant contribution to $\alpha_{J_n}^{(i,v)}$. We refer to this as "Main" valence correlation contribution and the rest that comes from the other higher level excited states as "Tail" contribution to $\alpha_{J_n}^{(i,v)}$.

For an accurate determination of the E1 matrix elements between many low-lying states, we employ the relativistic coupled-cluster (RCC) method by expressing the wave function ($|\Psi_v\rangle$) of an atomic state that has the closed core [$5p^6$] and a valence orbital v as

$$|\Psi_v\rangle = e^T\{1 + S_v\}|\Phi_v\rangle \tag{2.14}$$

where $|\Phi_v\rangle$ is a reference state, which is defined as $|\Phi_v\rangle = a_v^\dagger|\Phi_0\rangle$ with the Dirac-Hartree-Fock (DHF) wave function $|\Phi_0\rangle$ of the closed-core, T and S_v are the RCC excitation operators that excite electrons from the core and core along with the valence orbital respectively. In this work, we have only accounted for the single and double excitations which are denoted using the subscripts 1 and 2 respectively in the RCC operators as

$$T = T_1 + T_2 \quad \text{and} \quad S_v = S_{1v} + S_{2v}. \tag{2.15}$$

These are known as coupled-cluster singles and doubles (CCSD) method in the literature. Amplitudes of these operators are evaluated using the equations

$$\langle\Phi_0^*|\overline{H}|\Phi_0\rangle \;=\; 0 \tag{2.16}$$

and

$$\langle\Phi_v^*|(\overline{H} - E_v)S_v|\Phi_v\rangle \;=\; -\langle\Phi_v^*|\overline{H}|\Phi_v\rangle, \tag{2.17}$$

where $|\Phi_0^*\rangle$ and $|\Phi_v^*\rangle$ are the excited state configurations, here up to doubles, with respect to the DHF states $|\Phi_0\rangle$ and $|\Phi_v\rangle$, respectively, and $\overline{H} = (He^T)_l$ with subscript l representing the linked terms only. E_v is the energy eigenvalue of the $|\Psi_v\rangle$ state and is determined by using the expression

$$E_v = \langle\Phi_v|\overline{H}\,\{1 + S_v\}\,|\Phi_v\rangle. \tag{2.18}$$

Both Eqns. (2.17) and (2.18) need to be solved simultaneously for obtaining solutions of interdependent variables in a self-consistent approach. At the same level of approximation in

the excitations, a truncated RCC method can incorporate more contributions as compared to a truncated configuration-interaction (CI) method. For example, the lowest order mixing of $[4f^{13}5d6s]\ ^3[3/2]$ with $J = 1/2$ configuration and the DHF wave function of the $[4f^{14}6p]\ ^2P_{1/2}$ configuration is carried out by the S_{2v} operator while calculating the $[4f^{14}6p]\ ^2P_{1/2}$ atomic state function. Similar mixing also takes place among $J = 3/2$ configurations. Moreover, $\overline{H}$ in the CCSD method contains many non-linear terms that can take into account contributions from the higher level excitations, such as triples and quadruples, at the same level of excitation approximation of the CI method. As a matter of fact, the above mentioned configuration mixing are incorporated through the non-linear terms of the CCSD method and they take care of higher order correlation contributions. This is a unique feature of a truncated RCC method in contrast to other truncated many-body methods owing to the exponential form of expression in Eq. (2.14). In fact, it has also been employed to calculate many atomic properties of Yb^+ accurately in the past [49, 50].

After obtaining amplitudes using the above equations, the transition matrix element of the dipole operator D between the states $|\Psi_i\rangle$ and $|\Psi_f\rangle$ is evaluated using the expression

$$\frac{\langle\Psi_f|D|\Psi_i\rangle}{\sqrt{\langle\Psi_f|\Psi_f\rangle\langle\Psi_i|\Psi_i\rangle}} = \frac{\langle\Phi_f|\tilde{D}_{fi}|\Phi_i\rangle}{\sqrt{\langle\Phi_f|\{1+\tilde{N}_f\}|\Phi_f\rangle\langle\Phi_i|\{1+\tilde{N}_i\}|\Phi_i\rangle}}, \tag{2.19}$$

where $\tilde{D}_{fi} = \{1+S_f^\dagger\}e^{T^\dagger}De^T\{1+S_i\}$ and $\tilde{N}_{k=f,i} = \{1+S_k^\dagger\}e^{T^\dagger}e^T\{1+S_k\}$. The above expression involves two non-terminating series in the numerator and denominator, which are $e^{T^\dagger}De^T$ and $e^{T^\dagger}e^T$ respectively, and calculation of these terms are described in our previous works [50]. The "Main($\alpha_{J_n}^{(i,v)}$)" contributions have been calculated by combining the E1 matrix elements obtained using the above expression with the experimental energies as listed in Ref. [51]. Contributions from higher excited states including continuum to $\alpha_{J_n}^{(i,v)}$, denoted as "Tail($\alpha_{J_n}^{(i,v)}$)", are estimated approximately in the DHF method using the expression

$$\alpha_{J_n}^{(i,v)}(\omega) = \frac{2}{3(2J_n+1)}\sum_{K>n}\frac{(\epsilon_K-\epsilon_n)|\langle J_n||\mathbf{D}||J_K\rangle_{DHF}|^2}{(\epsilon_n-\epsilon_K)^2-\omega^2}, \tag{2.20}$$

where $\langle J_n||\mathbf{D}||J_K\rangle_{DHF}$ are obtained using the DHF wave functions, $K > n$ corresponds to the excited states including continuum whose matrix elements are not accounted in the Main($\alpha_{J_n}^{(i,v)}$) contribution, and $\epsilon_{n,K}$ refers to the DHF energies. Similarly, the core-valence contributions $\alpha_{J_n}^{(i,cv)}$ are also obtained through the DHF method approximation using the expression

$$\alpha_{J_n}^{(i,cv)}(\omega) = \frac{2}{3(2J_n+1)}\sum_{K}^{N_c}\frac{(\epsilon_K-\epsilon_n)|\langle J_n||\mathbf{D}||J_K\rangle_{DHF}|^2}{(\epsilon_n-\epsilon_K)^2-\omega^2}, \tag{2.21}$$

where N_c is the total number of electrons in the closed-core of the Yb^+. The static scalar core contributions $\alpha^{(0,c)}(0)$ in Yb^+, which is equal to the ground state polarizability of Yb^{2+}, are evaluated using the DHF, random-phase approximation (RPA) and a perturbed CCSD method considering a dipole operator D as an external perturbation as described in Ref. [52]. The trends in these results demonstrate role of electron correlation effects for its accurate evaluation. The DHF and RPA contributions are subsumed within the CCSD result by the formulation of the theory and are considered as the most precise calculation. Comparison between the results of DHF and CCSD; and RPA and CCSD show small differences while the CCSD method is computationally very expensive. As a matter of fact, it is not possible to apply the CCSD method to determine core contribution to the dynamic polarizabilities for the estimates of the $\lambda_{\rm magic}$ and $\lambda_{\rm T}$ values. Therefore, we employ the DHF method to calculate the core contributions to the dynamic polarizabilities. Nevertheless, core contributions cancel out completely in the determination of $\lambda_{\rm magic}$. Hence, accuracies in those values are not affected by the use of core correlations from the DHF method while the $\lambda_{\rm T}$ values can be estimated within reasonable accuracy.

2.4. Results and Discussion

Figure 2.1 shows the E1 transitions which are contributing in polarization of the states $[4f^{14}6s]\ ^2S_{1/2}$ and $[4f^{14}5d]\ ^2D_{3/2}$. Eqs.(2.7-2.9) shows the dependency of the polarizability of the atomic state upon E1 transition matrix, transition frequency and angular momentum of the energy state. We also observe from Fig. 2.1 that the $[4f^{14}6p]\ ^2P_{1/2,3/2}$ states will contribute dominantly to the polarizabilities of both the ground and $[4f^{14}5d]\ ^2D_{3/2}$ states. Therefore, accuracy of our result depends upon precise calculation of E1 matrix for transition between $[4f^{14}6s]\ ^2S_{1/2} \rightarrow [4f^{14}6p]\ ^2P_{1/2,3/2}$ and $[4f^{14}5d]\ ^2D_{3/2} \rightarrow [4f^{14}6p]\ ^2P_{1/2,3/2}$. In this section, we describe the result of static polarizability used for estimation of stark and BBR shift. We also show the result of magic wavelength and tune out wavelength which is calculated using dynamic polarizability of the clock states. This calculation gives the estimation of wavelength which are used for trapping ions in an optical lattice.

2.4.1 Static polarizability

In calculation of static polarization, we calculated E1 transition matrix from experimental and theoretical data for ground and $[4f^{14}5d]\ ^2D_{3/2}$ state. The values for each E1 transition are tabulated in Tab. 2.1, where we also give contributions from the individual correlation effects to the static $\alpha^{(i)}_{J_n}$ values of the ground and $[4f^{14}5d]\ ^2D_{3/2}$ states in $^{171}Yb^+$. The "Main" contributions are listed separately in the table along with the E1 matrix elements and resonant wavelengths $\lambda_{\rm res}$ of different transitions involving the low-lying $P_{1/2,\,3/2}$ states to illustrate their roles explicitly in the accurate evaluation of $\alpha^{(i)}_{J_n}$. Uncertainties of these matrix elements are

given along with their respective values. The uncertainties in the CCSD values are determined by estimating contributions from the neglected leading order triple excitations and due to use of the finite size basis functions in the calculation. We find that more than 90% contribution to the total static $\alpha^{(i)}_{J_n}$ values come from the $[4f^{14}6p]\ ^2P_{1/2}$ and $[4f^{14}6p]\ ^2P_{3/2}$ states in both the cases. Thus, we replace the E1 matrix elements of the $[4f^{14}6s]\ ^2S_{1/2} \rightarrow [4f^{14}6p]\ ^2P_{1/2,3/2}$ and $[4f^{14}5d]\ ^2D_{3/2} \rightarrow [4f^{14}6p]\ ^2P_{1/2}$ transitions that are obtained from the CCSD method by the values extracted from the combination of the experimental values of the lifetimes and the corresponding branching ratios from Ref. [20, 53] of the $[4f^{14}6p]\ ^2P_{1/2}$ and $[4f^{14}6p]\ ^2P_{3/2}$ states. These values are quoted in bold fonts while the CCSD values are mentioned just below these numbers in Table 2.1. We, however, could not extract out the E1 matrix element of the $[4f^{14}5d]\ ^2D_{3/2} \rightarrow [4f^{14}6p]\ ^2P_{3/2}$ transition from any available experimental data. Nevertheless, we find that the experimental value of the E1 matrix element, that is 2.97 a.u., corresponding to the $[4f^{14}5d]\ ^2D_{3/2} \rightarrow [4f^{14}6p]\ ^2P_{1/2}$ transition is very close to our CCSD result (2.95 a.u.). Since the $[4f^{14}6p]\ ^2P_{1/2}$ and $[4f^{14}6p]\ ^2P_{3/2}$ states are the fine structure partners, electron effects will behave similarly in determining these states. Therefore, we assume that the CCSD value for the E1 matrix element of the $[4f^{14}5d]\ ^2D_{3/2} \rightarrow [4f^{14}6p]\ ^2P_{3/2}$ transition will have similar accuracy as of the corresponding value of the $[4f^{14}5d]\ ^2D_{3/2} \rightarrow [4f^{14}6p]\ ^2P_{1/2}$ transition. Next to the $6P$ states, there lie the states with $[4f^{13}5d6s]$ configurations. Finding E1 matrix elements for these states are strenuous in the RCC method, but a CI method can estimate them more reliably. We consider these values either from the experimental data presented in Ref. [55] or are taken from the theoretical calculations reported in Ref. [54] using a CI method. Since uncertainties of these matrix elements obtained from the CI method are not given and their contributions to the polarizability values are found to be relatively small (see Table 2.1), we have not accounted for uncertainties from these matrix elements in the present work. In order to infer E1 matrix element of the $[4f^{13}5d6s]\ ^3[3/2]_{1/2} \rightarrow [4f^{14}5d]\ ^2D_{3/2}$ transition for estimating its contribution in the evaluation of the polarizability of the $[4f^{14}5d]\ ^2D_{3/2}$ state, we have used the experimentally measured lifetime of the $[4f^{13}5d6s]\ ^3[3/2]_{1/2}$ state from Ref. [55] and branching ratios reported in Refs. [56, 57].

As seen in Table 2.1, the core correlation has significant contribution to the scalar $\alpha^{(0)}_{J_n}$ values. This cannot be evaluated using a sum-over-states approach, so it is imperative to apply a suitable *ab initio* many-body method for its determination. The core correlation contribution $\alpha^{(i,c)}$ to the ground and $[4f^{14}5d]\ ^2D_{3/2}$ states of Yb^+, which corresponds to dipole polarizability of the Yb $^{2+}$ ion, has not been evaluated rigorously earlier. To determine this contribution more reliably, we apply three different methods in the DHF, RPA and CCSD approximations based on the first principle calculations as discussed in Ref. [52]. We find $\alpha^{(i,c)} = 7.45$ a.u., $\alpha^{(i,c)} = 6.38$ a.u. and $\alpha^{(i,c)} = 7.72$ a.u. from the DHF, RPA and CCSD methods, respectively. In Ref. [48], the RPA value is given as 6.386 a.u. which agrees well with our RPA value. The

Tab. 2.1: Contributions to the static values of $\alpha_{J_n}^{(i=0,2)}$ for the $[4f^{14}6s]\ ^2S_{1/2}$ and $[4f^{14}5d]\ ^2D_{3/2}$ states in Yb^+ are given in a.u. Absolute values of the dominantly contributing reduced E1 matrix elements (in a.u.) and resonance wavelengths in vacuum (λ_{res} in nm) are also listed. Values quoted in bold fonts are taken from other work as mentioned below.

Contribution	λ_{res} [51]	E1	$\alpha_{J_n}^{(0)}$	$\alpha_{J_n}^{(2)}$
$[4f^{14}6p]\ ^2P_{1/2}$	369.52	**2.471(3)** [20, 53]	16.51(4)	
$[4f^{13}5d6s]\ ^3[3/2]_{3/2}$	347.73	**1.10** [54]	3.1	
$[4f^{14}6p]\ ^2P_{3/2}$	329.03	**3.36(3)** [20, 53]	27.2(5)	
$[4f^{13}5d6s]\ ^3[3/2]_{1/2}$	297.05	**0.82(2)** [55, 56]	1.46(3)	
$[4f^{13}5d6s]\ ^1[3/2]_{3/2}$	289.14	**1.27(2)** [55]	3.45(3)	
$[4f^{14}7p]\ ^2P_{1/2}$	156.97	0.08(1)	0.0008(1)	
$[4f^{14}7p]\ ^2P_{3/2}$	152.45	0.11(1)	0.014(2)	
$\alpha^{(i,c)}$			7.7(7)	
$\alpha^{(i,cv)}_{6s^2S_{1/2}}$			−0.16(2)	
$\mathrm{Tail}(\alpha^{(i,v)}_{6s\ ^2S_{1/2}})$			0.046(15)	
Total			59.3(8)	
Ref. [48]			62.04	
Ref. [58]			47(9)[a]	
$[4f^{13}5d6s]\ ^3[3/2]_{5/2}$	2632.81	**0.00075** [55]	0.0	0.0
$[4f^{14}6p]\ ^2P_{1/2}$	2438.42	**2.97(4)** [20, 53]	79(2)	−79(2)
$[4f^{13}5d6s]\ ^3[3/2]_{3/2}$	1724.98	**0.27** [54]	0.46	0.37
$[4f^{14}6p]\ ^2P_{3/2}$	1345.63	1.31(2)	8.45(26)	6.76(21)
$[4f^{13}5d6s]\ ^3[3/2]_{1/2}$	935.19	**0.62(1)**[55, 56]	1.31(4)	-1.31(4)
$[4f^{14}7p]\ ^2P_{1/2}$	245.42	0.14(2)	0.018(5)	−0.018(5)
$[4f^{14}7p]\ ^2P_{3/2}$	234.56	0.014(5)	0.0002(1)	0.0001(1)
$[4f^{14}5f]\ ^2F_{5/2}$	210.34	2.43(4)	4.54(15)	−0.91(3)
$[4f^{14}6f]\ ^2F_{5/2}$	173.92	1.47(2)	1.38(4)	−0.275(7)
$[4f^{14}7f]\ ^2F_{5/2}$	158.89	0.93(1)	0.503(11)	−0.101(2)
$[4f^{14}8f]\ ^2F_{5/2}$	151.02	0.35(1)	0.068(4)	−0.014(1)
$\alpha^{(i,c)}$			7.7(7)	0.0
$\alpha^{(i,cv)}_{5d^2D_{3/2}}$			−0.43(3)	−0.08(1)
$\mathrm{Tail}(\alpha^{(i,v)}_{5d\ ^2D_{3/2}})$			4(2)	−0.83(25)
Total			107(3)	−75(2)
Ref. [58]			90(17)[a]	
Ref. [59]				−82(13)

[a]Note: Estimated by combining measured differential scalar polarizability $\alpha^{(0)}_{6s\ ^2S_{1/2}}$ - $\alpha^{(0)}_{5d\ ^2D_{3/2}}$ from Ref. [59] and E1 matrix elements from the measured lifetimes of many states as listed in Ref. [58].

DHF value is found to be larger than the RPA value, the CCSD value is larger than the other two methods. Though RPA is also an all order method, but it takes into account only the core-polarization correlations while the CCSD method includes pair-correlation effects to all orders along with the core polarization effects. We, therefore, consider CCSD value as the final result and it is given along with the estimated uncertainty in Table 2.1.

The "Tail" contributions to $\alpha_{J_n}^{(i,v)}$ and $\alpha_{J_n}^{(i,cv)}$ are also given in Table 2.1, which are obtained using the DHF method. The core-valence contributions are found to be negligibly small, whereas the "Tail" contributions to the scalar and tensor polarizabilities of the $[4f^{14}5d]\ ^2D_{3/2}$ state are significant. Accounting all these contributions, we obtain the final static polarizability of the ground state as 59.3(8) a.u., while the static scalar and tensor polarizabilities of the $[4f^{14}5d]\ ^2D_{3/2}$ state are 107(3) a.u. and $-75(2)$ a.u., respectively. An earlier calculation using the relativistic many-body perturbation theory (MBPT) presents ground state static polarizability value as 62.04 a.u.[48]. The discrepancy arises from the value of E1 matrix elements that are used for the transitions involving the $[4f^{14}6p]\ ^2P_{1/2}$ and $[4f^{14}6p]\ ^2P_{3/2}$ states. On the other hand, Lea *et. al.* have also estimated this value as 47(9) a.u. [58] using experimental E1 matrix elements. In their calculation, only few E1 transitions were included and the core contribution was completely neglected. Nevertheless, both the values agree within their respective uncertainties. Accurate calculations of $\alpha_{J_n}^{(i)}$ for the $[4f^{14}5d]\ ^2D_{3/2}$ state is very challenging as compared to the ground state. Here, the E1 matrix elements between this state and the $[4f^{14}\ np]\ ^2P_{1/2,3/2}$ and $[4f^{14}\ nf]\ ^2F_{5/2}$ states, with the principle quantum number n, mainly contribute. We observe from Table 2.1 that contributions from the E1 matrix elements involving the $[4f^{14}\ nf]\ ^2F_{5/2}$ states converge very slowly as compared to the $[4f^{14}\ np]\ ^2P_{1/2,3/2}$ states with higher n value. We, therefore, consider $n = 5, 6, 7, 8$ for the $[4f^{14}\ nf]\ ^2F_{5/2}$ states and $n = 6, 7$ for the $[4f^{14}\ np]\ ^2P_{1/2,3/2}$ states in the evaluation of "Main" contribution to $\alpha_{J_n}^{(i,v)}$. Among these contributions, the E1 matrix element of the $[4f^{14}5d]\ ^2D_{3/2} \rightarrow [4f^{14}6p]\ ^2P_{1/2}$ transition dominates. The contribution from the $[4f^{14}5d]\ ^2D_{3/2} \rightarrow [4f^{14}6p]\ ^2P_{3/2}$ transition is found to be about ten times smaller than the above transition. This is owing to the fact that its E1 matrix element is almost half while its transition energy is twice larger than the corresponding value of the $[4f^{14}5d]\ ^2D_{3/2} \rightarrow [4f^{14}6p]\ ^2P_{1/2}$ transition. Noticeably contributions from the $[4f^{13}5d6s]$ configurations are non-significant as seen in Table 2.1. Unlike for the ground state, the "Tail" contribution to $\alpha_{J_n}^{(0)}(0)$ is about 4% of its total value. Thus, the dominant sources of uncertainty in $\alpha_{J_n}^{(o)}$ comes from the "Tail" contribution. Similar trends are also observed in the determination of the static $\alpha_{J_n}^{(2)}$ value of the $[4f^{14}5d]\ ^2D_{3/2}$ state, which are also quoted in Table 2.1. Lea *et. al.* have estimated its scalar polarizability value as 90(17) a.u. [58] considering only few E1 matrix elements deducing from the experimental lifetime values. The reason for which we believe to obtain more reliable results for α of the ground and $[4f^{14}5d]\ ^2D_{3/2}$ than the previously estimated values is because of use of more accurate values of the E1 matrix elements of

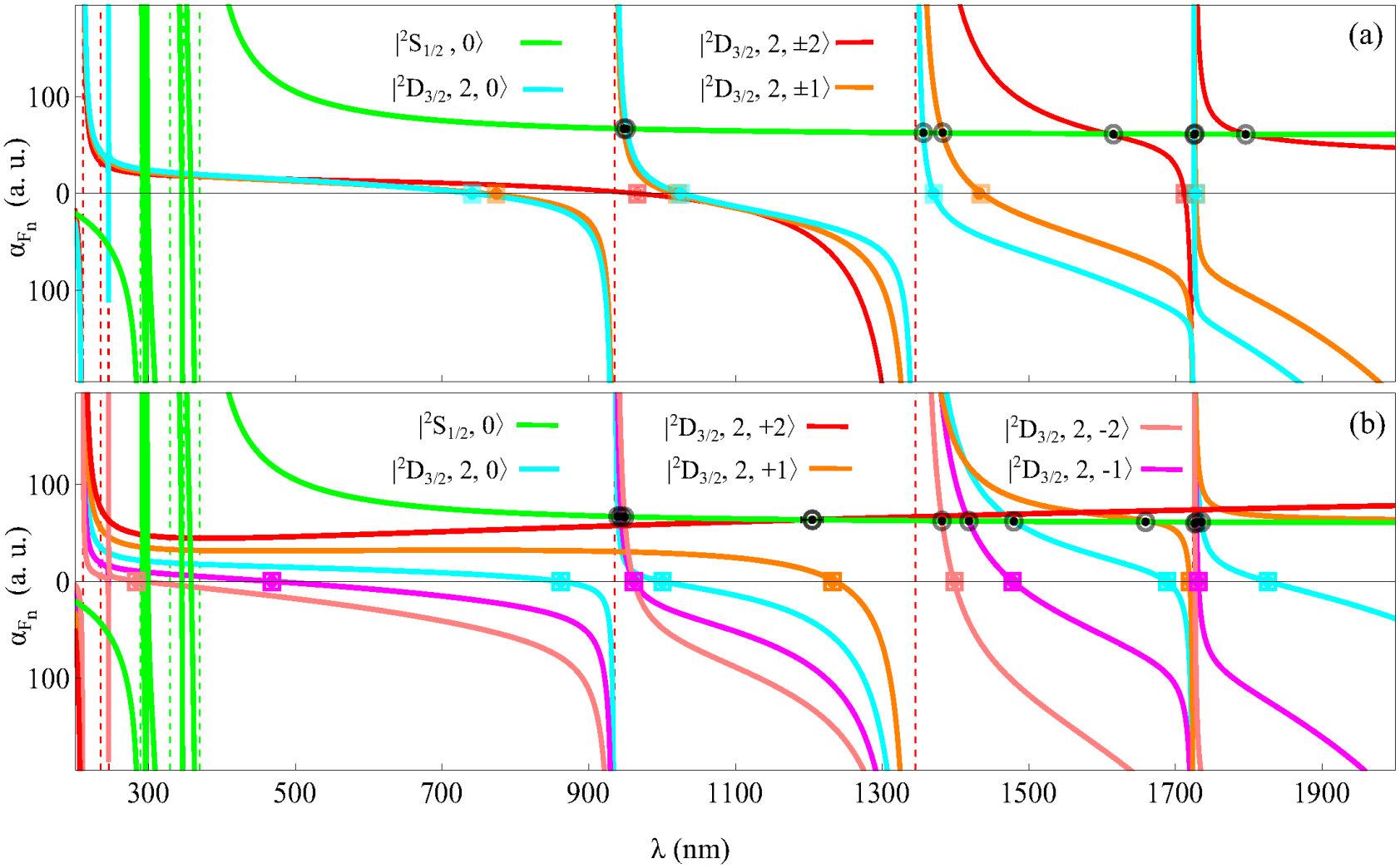

Fig. 2.2: Wavelength dependent dynamic dipole polarizabilities of the $[4f^{14}6s]\ ^2S_{1/2}(F=0)$ state (denoted by $|^2S_{1/2},0\rangle$) and for all possible M_F sublevels of the $[4f^{14}5d]\ ^2D_{3/2}(F=2)$ state (denoted by $|^2D_{3/2},2,M\rangle$) in $^{171}Yb^+$ using (a) linearly and (b) right-circularly polarized light. The λ_{magic} and λ_T values are indicated in dots which are encircled by circles and squares, respectively. The vertical dashed lines signify the resonances from the $[4f^{14}6s]\ ^2S_{1/2}(F=0)$ and $[4f^{14}5d]\ ^2D_{3/2}(F=2)$ states in green and red colors, respectively.

the $[4f^{14}5d]\ ^2D_{3/2} \rightarrow [4f^{14}6p]\ ^2P_{3/2}$, $[4f^{14}5d]\ ^2D_{3/2} \rightarrow [4f^{14}\ 5f]\ ^2F_{5/2}$ and $[4f^{14}5d]\ ^2D_{3/2} \rightarrow [4f^{14}\ 6f]\ ^2F_{5/2}$ transitions, and core contribution that are evaluated using our RCC method. An experimental value of the tensor polarizability of the $[4f^{14}5d]\ ^2D_{3/2}$ state has been reported as $-82(13)$ a.u. [59]. From the comparison, we find our estimated value agrees with the experimental result indicating that we are able to produce polarizabilities in the investigated states accurately.

Using the static polarizability values as mentioned above, we estimate the BBR shifts in the ground and $[4f^{14}5d]\ ^2D_{3/2}$ states of Yb^+ as $-0.52(1)$ Hz and $-0.92(2)$ Hz, respectively. Further, we evaluate the dynamic corrections to these quantities approximately, using Eq. (2.11), as $-0.0004(1)$ Hz and $-0.04(1)$ Hz in the ground and $[4f^{14}5d]\ ^2D_{3/2}$ states respectively. From this analysis, we obtain the net differential scalar polarizability value of the $[4f^{14}6s]\ ^2S_{1/2} \rightarrow [4f^{14}5d]\ ^2D_{3/2}$ transition as $-7.8(5) \times 10^{-40}\,\mathrm{Jm^2V^{-2}}$ against the available experimental value of $-6.9(1.4) \times 10^{-40}\ \mathrm{Jm^2V^{-2}}$ [59]. This corresponds to the differential BBR shift for the $[4f^{14}6s]\ ^2S_{1/2} \rightarrow [4f^{14}5d]\ ^2D_{3/2}$ clock transition as -0.44(3) Hz. This value comes out to be larger than the measured value $-0.37(5)$ Hz by Tamm et al [60], which is being currently considered for estimating uncertainty due to the BBR shift in the above clock transition frequency. There are also two different values predicted as $-0.254(5)$ Hz and $-0.261(8)$ Hz by Lea et al obtained from the *ab initio* calculations and by combining both the experimental and theoretical data, respectively [58].

2.4.2 Magic wavelengths for linearly and circularly polarized light

In order to find out λ_{magic} among different magnetic sublevels M_F of the $[4f^{14}6s]\ ^2S_{1/2}(F = 0) \rightarrow [4f^{14}5d]\ ^2D_{3/2}(F = 2)$ clock transition we estimate dynamic α_{F_n} values of the associated states at different wavelengths ranging from 200-2000 nm. First the atomic polarizabilities of the $[4f^{14}6s]\ ^2S_{1/2}$ and $[4f^{14}5d]\ ^2D_{3/2}$ states are determined using the relations given in Eqs. (2.7-2.9), then total polarizability value is obtained from Eq. (2.3). In Fig. 2.2 we plot our estimated α_{F_n} values of both the states as function of the wavelength. To obtain the λ_{magic} values for the $|4f^{14}6s\ ^2S_{1/2},\ F = 0\rangle \rightarrow |4f^{14}5d\ ^2D_{3/2},\ F = 2\rangle$ transition, we have considered all possible combinations of M_F sublevels and also different light polarizations. In Fig. 2.2(a), we plot the dynamic polarizabilities for the states associated with the $|^2S_{1/2}, F = 0\rangle \rightarrow |^2D_{3/2},\ F = 2,\ M_F = 0, \pm 1, \pm 2\rangle$ transitions against the wavelength corresponding to a linearly polarized light. Similar plots are shown in Fig. 2.2(b) for the $|^2S_{1/2}, F = 0\rangle$ and $|^2D_{3/2},\ F = 2,\ M_F = -2,\ -1,\ 0,\ 1,\ 2\rangle$ states assuming a circularly polarized light. The wavelengths at which intersections of the polarizability curves take place are recognized as λ_{magic}. In Table 2.2 we list the λ_{magic} values for the $|4f^{14}6s\ ^2S_{1/2},\ F = 0\rangle \rightarrow |4f^{14}5d\ ^2D_{3/2},\ F = 2\rangle$ transition in the presence of a linearly polarized light. It can be noticed that these λ_{magic} values

Tab. 2.2: The λ_{magic} values in nm and their corresponding α_{F_n} values in a.u. values among different M_{F_n} sub-levels of the $[4f^{14}6s]\ ^2S_{1/2}(F = 0) \rightarrow [4f^{14}5d]\ ^2D_{3/2}(F = 2)$ clock transition in $^{171}Yb^+$ are listed for both the linearly and right-circularly polarized light.

Linear			Circular		
M_F	λ_{magic}	α_{F_n}	M_F	λ_{magic}	α_{F_n}
0	1725.4(1)	62(2)	-2	1726.5(1)	60(5)
	1356.3(3)	63(2)		1381.8(6)	62(2)
	951.8(5)	66(2)		948.9(2)	64(2)
	357.3(1)	21.03(1)		358.1(2)	-6.2(3)
	344.9(1)	21.81(4)		345.2(2)	-5.1(3)
	298.8(3)	25.68(3)		299.1(1)	-1.31(6)
	291.8(1)	26.52(6)		292.2(1)	-0.80(1)
	245.4(1)	-53.43(3)		243.5(1)	-55.3(2)
±1	1726.6(1)	61(2)	-1	1728.8(3)	61(2)
	1382(1)	63(2)		1418(2)	62(2)
	948(1)	65(2)		944.4(2)	67(3)
	357.3(2)	20.61(3)		357.8(1)	5.7(1)
	344.9(1)	21.01(2)		345.1(1)	6.4(2)
	298.8(1)	24.62(6)		299.0(1)	9.41(5)
	291.8(1)	25.43(5)		292.1(1)	9.89(7)
	245.4(1)	-53.59(6)	0	1735.4(2)	61.4(7)
±2	1788(6)	63(1)		1479(5)	62(5)
	1619(5)	59(1)		939.7(2)	67(2)
	357.4(2)	18.0(2)		357.4(2)	18.8(2)
	345.1(2)	18.42(2)		345.0(2)	19.3(3)
	298.8(1)	20.63(5)		298.8(1)	21.96(5)
	291.9(1)	21.20(5)		291.9(1)	22.50(7)
			1	1657(15)	61(2)
				356.9(2)	32.1(6)
				344.8(2)	32.5(3)
				298.7(1)	35.30(5)
				291.7(1)	35.84(5)
			2	1204(45)	64(2)
				356.5(2)	46.6(9)
				344.7(2)	47.0(5)
				298.5(1)	50.31(7)
				291.6(1)	51.17(9)

support a red-detuned trap (depicted by the positive values of dipole polarizabilities at these wavelengths) except at 245.4 nm. Magic wavelengths at the infrared region are considered to have more experimental significance due to availability of high power fiber or solid state lasers in comparison to ultraviolet wavelengths produced by the sum or difference frequency generation techniques. Similarly, the λ_{magic} for the $|4f^{14}6s\ ^2S_{1/2},\ F = 0\rangle \rightarrow |4f^{14}5d\ ^2D_{3/2},\ F = 2\rangle$ transition in the presence of a right-circularly polarized light are also given in Table 2.2. In

Tab. 2.3: The λ_T values in nm for all possible M_F components of the considered states in $^{171}Yb^+$ using linearly and right-circularly polarized light. The term "Both" for $[4f^{14}6s]\ ^2S_{1/2}(F=0)$ state means that the results are same for linear and circular polarization.

$[4f^{14}6s]\ ^2S_{1/2}(F=0)$			$[4f^{14}5d]\ ^2D_{3/2}(F=2)$					
Polarization	M_F	λ_T	Polarization	M_F	λ_T	Polarization	M_F	λ_T
Both	0	357.9(1)	Linear	0	1725.4(1)	Circular	-2	1726.9(1)
		345.2(1)			1370.2(3)			1398.1(2)
		299.1(1)			1026.9(8)			961.7(1)
		292.2(1)			741.2(5)			283.3(4)
				±1	1727.8(1)		-1	1731.3(1)
					1438.6(3)			1478.1(1)
					1021(1)			961.6(1)
					774(4)			468.2(7)
				±2	1712.4(3)		0	1826(2)
					966(4)			1688.3(3)
								1000(2)
								861(3)
							1	1719.4(1)
								1233(1)
							2	-

the present work, we determine λ_{magic} for right circularly polarization using $A = 1$ considering all possible positive and negative M_F sublevels of the states participating in the transition. Note that λ_{magic} for the left circularly polarized light of a transition with a given M_F are equal to right circularly polarized light with opposite sign of M_F.

2.4.3 Magic wavelengths for comprehensive trapping

In Eqn.2.3, we observe that the polarizability of the state is independent of M_F sublevels if we make tensor and vector component of polarizabilities equal to zero. The vector polarizability of the state goes to zero, if we use laser light with linear polarization and the tensor polarizability goes to zero, if $\cos^2\theta_P$ values is 1/3. To reduce or cancel the tensor component, we change our system configuration in such a way that, the angle between quantization axis of system and the polarization axis of light is nearly 54^0. In this way we reduce the tensor part, which makes the trapping of ion independent of M_F values. In Fig. 2.3, we show λ_{magic} values that are independent of the hyperfine sub-levels and their M_F sublevels of the states involved in the clock transition. These λ_{magic} values will produce null differential Stark shifts exclusively among any hyperfine level of the ground and excited state. We have identified at least seven magic wavelengths for the hyperfine level independent trapping, out of which four are in the ultra violet and two in the infra red region. The λ_{magic} values along with the polarizability values at these wavelengths are marked with arrows in Fig. 2.3. In order to distinguish the M_F

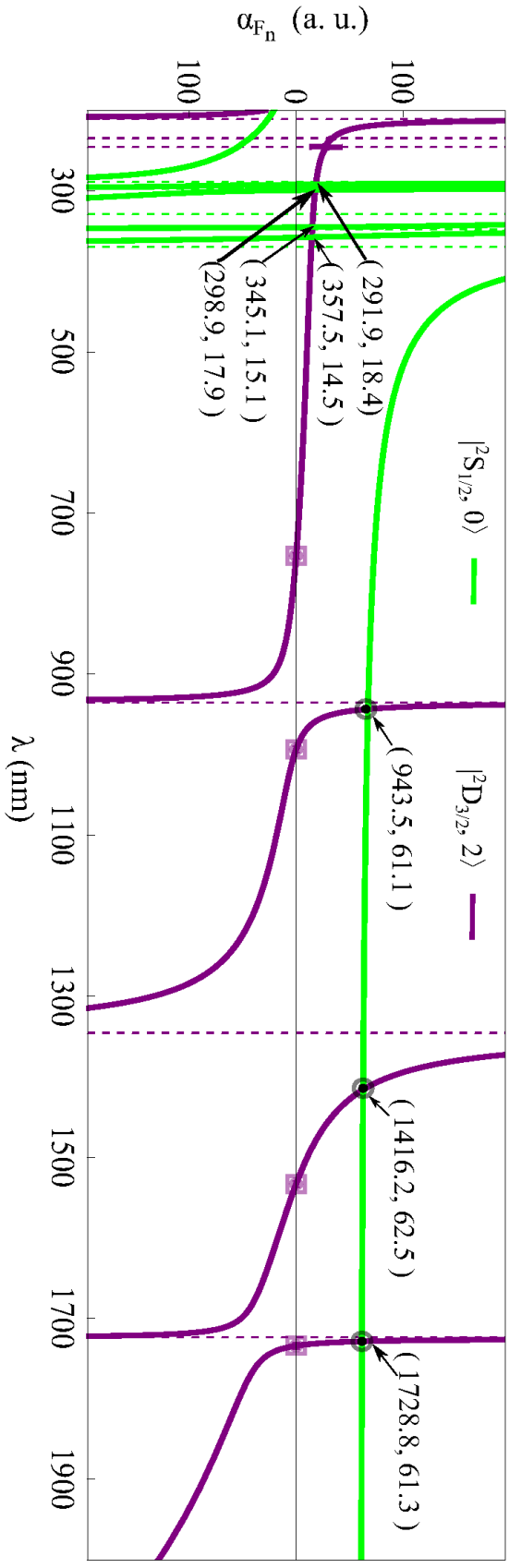

Fig. 2.3: Dynamic scalar polarizabilities of the $[4f^{14}6s]\ ^2S_{1/2}$ and $[4f^{14}6s]^2D_{3/2}$ states when vector and tensor polarizability components are zero. The λ_{magic} and λ_T wavelengths for comprehensive trapping are pointed out in dots and encircled by circles and squares, respectively, are independent of the hyperfine levels and magnetic sub-levels of the states. In particular to the λ_{magic}, their corresponding α_F values are indicated within brackets.The vertical dashed lines signify the resonances from the ground and $[4f^{14}5d]\ ^2D_{3/2}$ states in green and purple colors, respectively.

Tab. 2.4: Summarized values for BBR and polarizabilities of the clock states

Parameters	Experiment [59]	Our calculation
$\alpha_s(^2S_{1/2})$		9.7(1) $\times 10^{-40}$ Jm^2/V
$\alpha_s(^2D_{3/2})$		17.6(5) $\times 10^{-40}$ Jm^2/V
$\alpha_T(^2D_{3/2})$	-13.6(2.2) $\times 10^{-40}$ Jm^2/V	-12.3(3) $\times 10^{-40}$ Jm^2/V
$\Delta\ \alpha_s = {}^2S_{1/2}$ - $^2D_{3/2}$	-6.9(1.4) $\times 10^{-40}$ Jm^2/V	-7.8(5) $\times 10^{-40}$ Jm^2/V
BBR shift $^2S_{1/2}$		-0.52(1) Hz
BBR shift $^2D_{3/2}$		-0.92(2) Hz
Dynamic correction $^2S_{1/2}$		-0.0004(1) Hz
Dynamic correction $^2D_{3/2}$		-0.04(1) Hz
Total BBR shift $^2D_{3/2}$ - $^2S_{1/2}$	-0.37(5) Hz	-0.44(3) Hz

independent magic wavelength, the λ_{magic} presented in Table 2.2 for linearly and circularly polarized light can be compared to the values marked in Fig. 2.3. The trapping scheme as proposed in Ref. [44] and using λ_{magic} indicated in Fig. 2.3, one can optically trap Yb^+ with zero light shift in the $[4f^{14}6s]\ ^2S_{1/2} \rightarrow [4f^{14}5d]\ ^2D_{3/2}$ transition for any given combinations of the F and M_F levels that are experimentally viable.

2.4.4 Tune-out wavelengths

In many experiments, there is a requirement of trapping atom/ion in optical lattice without affecting any one of the energy states. In this type of experiment, tune-out wavelength is used. At tune out wavelength, the polarizability of the state is completely independent of intensity of light used for trapping which makes our desired state unperturbed. In our calculation, we identified polarization dependent tune-out wavelengths at which the dynamic polarizabilities reduces to zero individually with different M_F sub-levels in both $F = 0$ state of $[4f^{14}6s]\ ^2S_{1/2}$ and $F = 2$ state of $[4f^{14}5d]\ ^2D_{3/2}$. These λ_T values are listed in Table 2.3 together with the M_F values against wavelengths of light with linear and circular polarizations. We have also identified four tune-out wavelengths for the $[4f^{14}5d]\ ^2D_{3/2}$ state at 1734.2(2), 1533.2(1), 993.5(5), and 753(3) nm, which could be useful for carrying out measurements irrespective of choice for hyperfine sub-levels, as given in Tab. 2.3

2.5. Conclusion

We have calculated polarizability of ground state $[4f^{14}6s]\ ^2S_{1/2}$ and metastable $[4f^{14}5d]\ ^2D_{3/2}$ states of Yb^+. In this calculation, we have used few theoretical techniques like DHF, MBPT, RPA CCSD, RCC and CI and experimental data like branching ratio and life time of the excited state, for estimating the magnitude of E1 transition matrix, which are contributing in polarization. The polarizability of states is used for estimation of systematic shifts like Stark shifts and BBR shifts for clock transition $6S_{1/2} \rightarrow 5D_{3/2}$ of Yb ion. The summarized values for our calculation and compared with the experimental values are tabulated in Tab. 3.6. We have also calculated the dynamic polarizability for wavelength range from 200 nm to 2000 nm, which gives the values of magic wavelengths and tune out wavelengths for the clock states. In these calculations, we also searched for magic and tune out wavelength for comprehensive trapping, where, in this type of trapping, the polarizability is independent of magnetic quantum number of the atomic state. After all these calculations, we found that there are possibilities of trapping ion in optical lattice and the lattice laser wavelength is equal to one of the magic wavelength, which gives zero Stark shift during clock transition. Our results will be of interest for carrying out precision measurements in the $[4f^{14}6s]\ ^2S_{1/2} \rightarrow [4f^{14}5d]\ ^2D_{3/2}$ transition of Yb^+ for attaining high accuracy clock frequency and investigating many fundamental physics.

Chapter 3

Low Noise Computer Controlled DC Voltage Source

Publication: A. Roy, N. Batra, S. Majhi, S. Panja, A. Sen Gupta, and S. De, Design of a Stable DC Voltage Source and Computer Controlling of It Using an Indigenously Developed All-Digital Addressing-Cum-Control Hardware, MAPAN-Journal of Metrology Society of India, **33**, 139 (2017).

3.1. Introduction

In every precision experiment a series of processes are being carried out following a prescribed sequence. The outcome of which depends on execution of a particular protocol and synchronous operation of the modules associated to it. Manual control restricts the achievable accuracy due to human errors introduced in the protocol and its shot-to-shot variation which also disturbs the repeatability and reproducibility of the data. Due to this reason, automation is required which minimizes the manual errors such as, input errors, delays in simultaneous operation, shot-to-shot variations and so on. Thus, state-of-the-art experiments as the one going on in our laboratory for building optical frequency standard using single trapped Ytterbium-ion [61, 62] needs to be automated so that it can operate uninterruptedly over a period of weeks. This also helps in self-diagnosis of any malfunctioning in modules associated to the experimental system. To give a figure of merit, in our experiment we will use five voltage sources for trapping ions [63, 64]; three current sources for producing magnetic fields; five lasers for photoionization, laser cooling and probing the clock transition; twenty optical modulators for generating desired laser frequencies [65]; ten servo controls for frequency and power stabilization of the laser beams [66, 67]; twenty mechanical shutters for blocking-unblocking laser beams [68] and so on as shown in Fig. 3.1. Apart from the large number of control knobs, operation of all the devices are time dependent and needs to be synchronized with each other in a single experimental run. This will be repeated over few days in order to achieve better statistics.

Worldwide many labs have indigenously developed hardware and software to incorporate automation, which are required for sequencing, interfacing and controlling their experiments remotely, which are given in the references [70, 71, 72, 73, 74, 75, 76]. As per the requirement in our experiment, we have also developed a digitally operated addressing and control module (DACM) which is capable of automating our indigenously developed modules. The module is fabricated using off-the-shelf parts and the design is simple to construct, as described in this chapter.

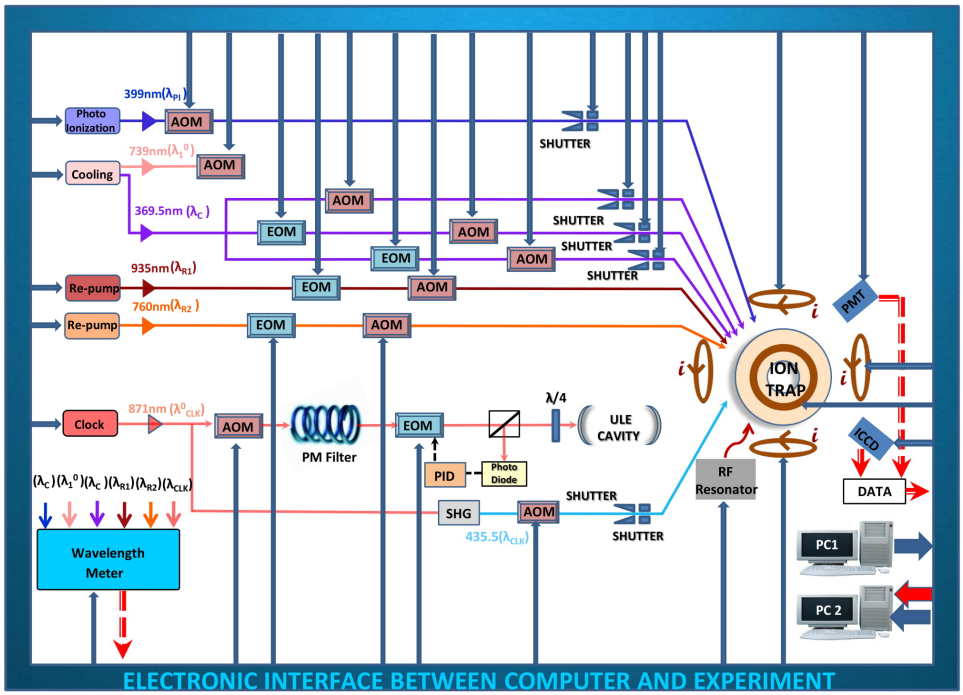

Fig. 3.1: A schematic of our experiment which shows the requirement of automation [69].

We have also developed a multipurpose computer programmable, low noise voltage source and verified its operation by controlling our DACM. The use of DACMs are universal but not limited to operate the voltage sources. We use these to computer control a wide variety of instruments in our lab, such as current source, AOM drivers, EOM drivers, and so on. Some of their other applications, such as AOM/EOM drivers using DACM is described in Chapter 4. Detailed description and characteristics study of this voltage source is given in the following sections. Since this voltage source is programmable, it is also used as an arbitrary waveform generator for low frequency operations. Such computer controlled and stable high voltage sources have many applications at low frequencies. As for example, our voltage source can be used to drive the piezo in an extended cavity diode laser (ECDL) for smooth scanning or ramping of the laser frequency from a computer or tuning length of a Fabry-Perot cavity.

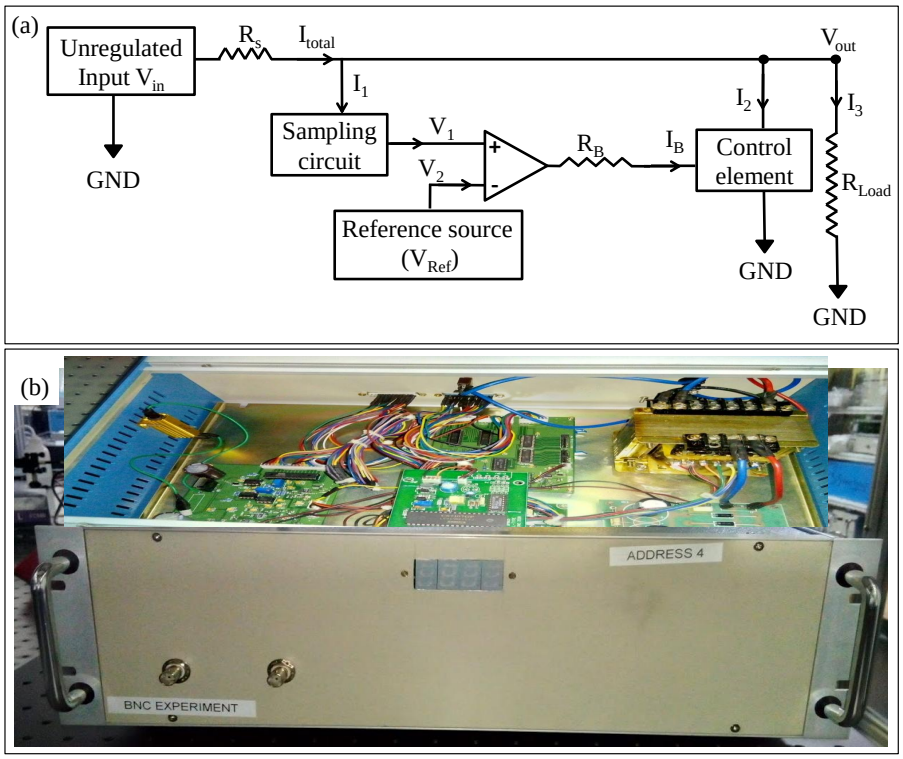

Fig. 3.2: (a)Block diagram of discrete transistor shunt voltage regulator use for design a low noise computer control regulated voltage source.(b) Front view of the voltage source and its internal circuit assemblies

Of particular interest, we have developed this voltage source for biasing the electrodes of our ion-trap [61, 63].

3.2. Theory

Automation is one of the main requirements in any kind of sophisticated experiments as it improves the repeatability and reproducibility of the data of the measurement. In our experiment, we have many different modules which are connected through a common digital bus. Remote control of all modules through common digital bus serially requires a communication protocol. In our experiment, we use a new type of protocol which consists of three stages: trigger, decoded address and data transfer. In this protocol, pulse width of the trigger is decided by the time for the events to occur *i.e* it decides the speed of the communication. In our system, there are many modules, which are used simultaneously to perform experiment. When we impart address to any module from the computer in terms of digital bits, the same has to be decoded at the other end for which we use decoders. The decoders have one active high pin

and other active low corresponding to input digital bits and its functional equation is

$$O_n = X_0 \times D_i \tag{3.1}$$

where O_n is n^{th} output pin, X_o is condition for decoding and D_i is input digital number. When we give the correct condition to the decoder and send a digital number D with corresponding binary number i, then i^{th} number of pin of output is active high. Using the active High pin, we setup the following logic for data transfer from computer to module:

$$O_{cn} = O_n \times I_{cn} \tag{3.2}$$

where O_{cn} and I_{cn} are output and input control bits used for controlling modules used in the experiment. The used protocol is faster than the conventional serial communication because all bits are transferred parallelly using data bus; only trigger pulse goes serially.

Other than automation module, we have also developed a low noise computer controlled regulated voltage source, which is used for controlling ion motion inside the trap. The regulated low noise voltage source has four main parts: AC to DC convertor, reference source, feedback amplifier and control element. In AC-DC convertor, we use bridge rectifier with RC type filter which is able to produce an unregulated DC voltage with small ripples of the form,

$$\gamma = \sqrt{\frac{{V_{rms}}^2}{V_{DC}} - 1} \tag{3.3}$$

where γ is ripple factor, V_{rms} and V_{DC} is input AC and output DC voltage, respectively. As per our requirement of voltage source in our experiment, the ripple factor is very high, so we need an additional low noise DC voltage circuit. In our case, we use a discrete transistor shunt voltage regulator which is used to further minimize the ripples and make a regulated, low noise voltage source. The corresponding block diagram is shown in Fig. 3.2. For feedback amplifier, we use Opamp for comparing the reference and unregulated voltage which gives feedback to control element, so that the final output is a regulated voltage. In this kind of circuit, the output noise mainly depends upon the reference source which is responsible for the stability and uncertainty of the output voltage. As shown in Fig. 3.2, total current drawn from the unregulated source is

$$I_{total} = I_1 + I_2 + I_3 \tag{3.4}$$

Tab. 3.1: Truth table of DEC-1 when $\{\overline{E}_{i1}; \overline{E}_{i2}; \overline{E}_{i3}\}$ operates at $\{0; 0; 1\}$. The'→' indicates operating state of DEC-1 as shown in Fig. 3.3 (a) which can further generate 8 different addresses after DEC-2.[77]

	Input			Output							
	I_1	I_2	I_3	$\overline{o}_{17}$	$\overline{o}_{16}$	$\overline{o}_{15}$	$\overline{o}_{14}$	$\overline{o}_{13}$	$\overline{o}_{12}$	$\overline{o}_{11}$	$\overline{o}_{10}$
	0	0	0	1	1	1	1	1	1	1	0
	0	0	1	1	1	1	1	1	1	0	1
	0	1	0	1	1	1	1	1	0	1	1
	0	1	1	1	1	1	1	0	1	1	1
	1	0	0	1	1	1	0	1	1	1	1
	1	0	1	1	1	0	1	1	1	1	1
→	1	1	0	1	0	1	1	1	1	1	1
	1	1	1	0	1	1	1	1	1	1	1

Here, we are designing a voltage source with no output current requirement, so we assume $I_3 = 0$; the feedback voltage connected to control element is

$$V_F = A(V_1 - V_2) - I_B R_B \tag{3.5}$$

where,V_F is feedback voltage, A is opamp open loop gain, I_B is current from opamp to control element and V_1 is a fraction of output voltage (V_{out}/x), so final equation is

$$V_{out} = x\left[V_2 + \frac{(V_F + I_B R_B)}{A}\right] \tag{3.6}$$

where $1/x$ is fraction of output voltage taken from sample circuit. It is clear from this equation that the output voltage depends upon reference voltage when the open loop gain of the opamp is high. It also shows that designing a linear low noise voltage source requires low noise, linear regulated reference source with an opamp which has low noise, low offset voltage.

3.3. Circuit Design

This section gives a complete description of our voltage source that includes the DACM that provides unique address to module for its control through a computer and complete description of the hardware of the DC voltage source. Controlling the DC voltage source through computer using common data bus requires a unique address to each module. Due to this requirement, we have indigenously developed DACM, that interfaces to the equipment with the PC by using a commercially available data acquisition card which is programmed in the Laboratory Virtual Instrument Engineering Workbench(LabVIEW) platform. This module is designed in such a way that it can control 64 devices, which can be multiplexed further if necessary. The DACM circuit consists of a dual re-triggerable monoshot (Mono)74LS123, a dual input quad NAND gates(N) 7400, and a pair of three input-eight output decoder (DEC)74LS138, as shown in

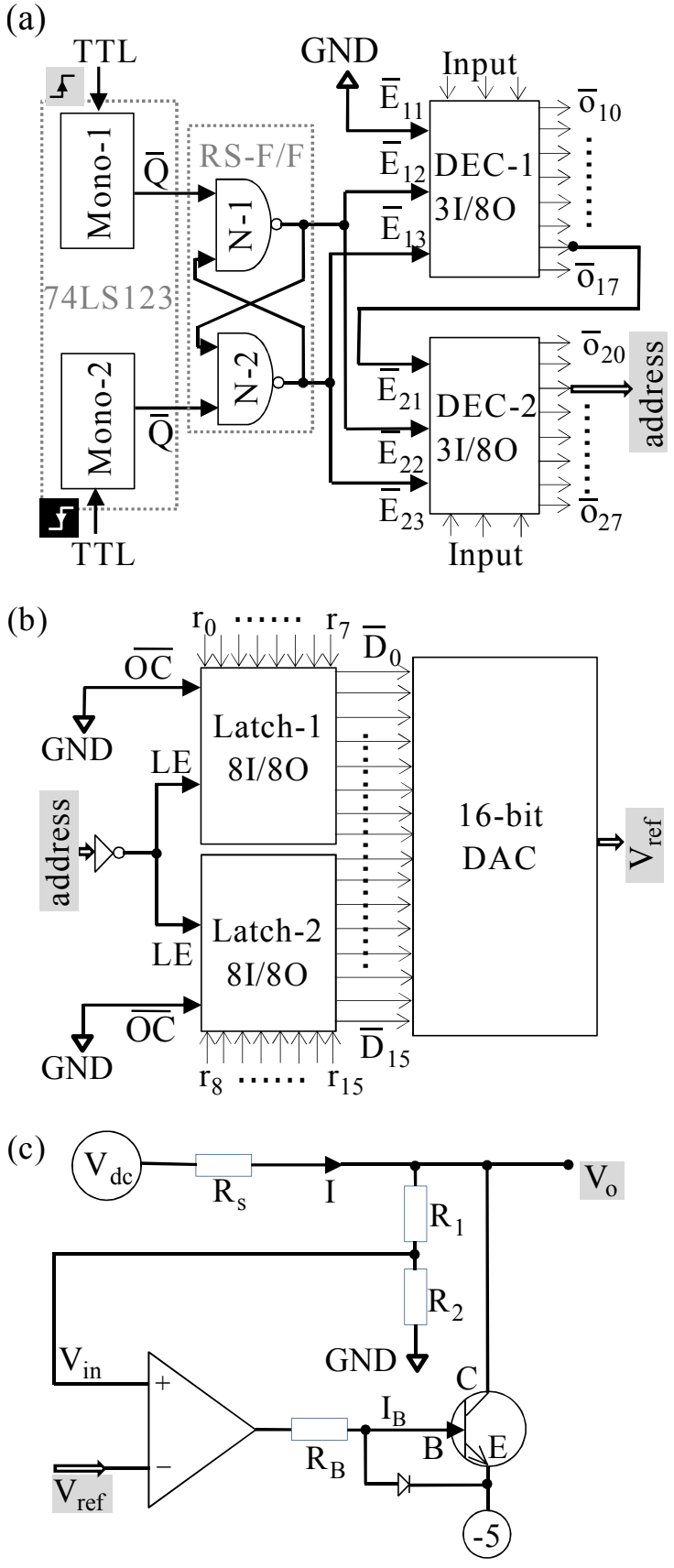

Fig. 3.3: Circuit diagrams for: (a) generating unique individual address for an equipment which is required for reading them from a PC, (b) DACM for writing data to the particular equipment, and (c) constant dc voltage source. [77]

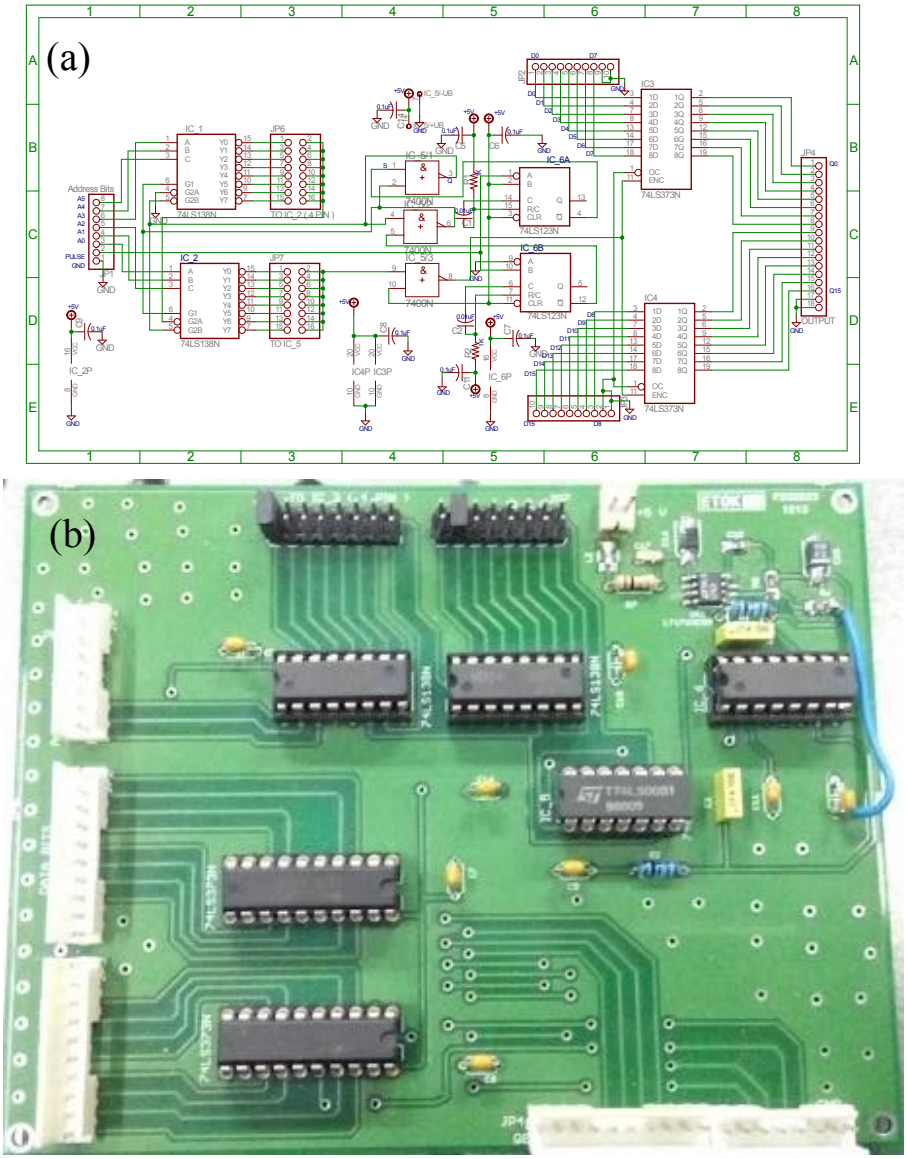

Fig. 3.4: (a) Schematic of DACM which is designed in Eagle v6.4 and (b) Populated PCB board.

Fig. 3.3(a). This module gets activated upon receiving of a trigger pulse (in the form of TTL) which by default comes from the data acquisition (DAQ) card or can also be received from an external precise pulse generator such as atomic clock. We design this module in such a way that it triggers the process of generating desired address and transfers control data only at the rising edge of the trigger pulse. At rising edge and falling edge, mono 1 and mono 2 are activated one by one, respectively for a short interval of time. The pulse width of the Monos is set to 2.8 μs, which is very less than the pulse width of trigger pulse t_w. The complement output of the Monos are connected to the two input of RS-flip flop, that is constructed using N-1 and 2 of a quad NAND gate and is used as a state shifter. These flip flops change their

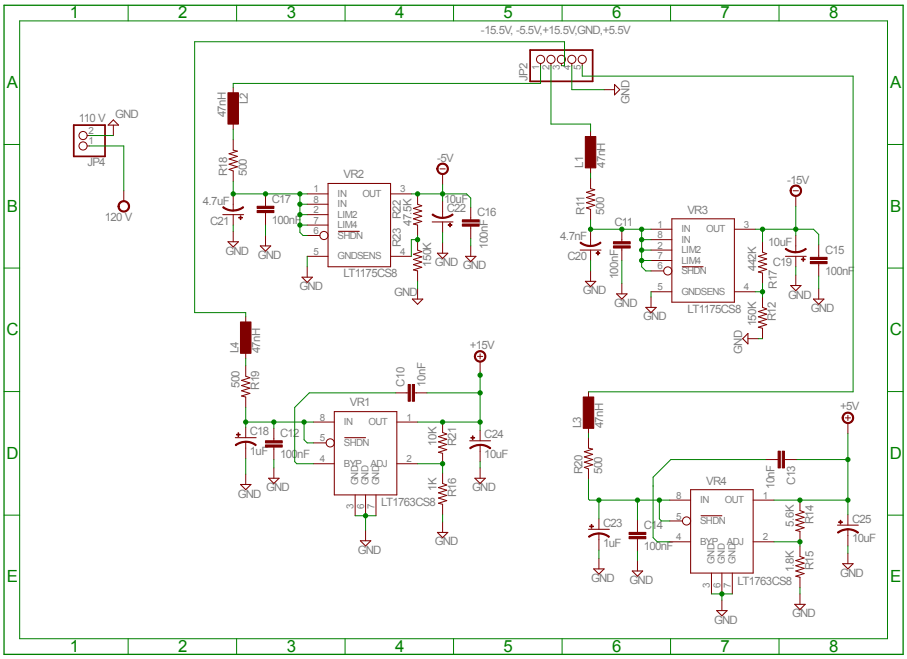

Fig. 3.5: Schematic of power supply section used to design low noise voltage source.

states only at the rising and falling edges if the pulse width of clock is larger than pulse generated by the Monos. In this RS-flip flop, there is invalid condition when all inputs are in low state. To avoid this condition, we connect the input of RS-flip flop with complement of the monostable multivibrators. The output of flip flop is then connected to two decoders in such a way that it only enables decoders when trigger pulse is active high as shown in Fig. 3.3(a). The decoder DEC-i (for i=1 and 2) decodes three inputs-to-eight outputs o_{i0};. . . ,o_{i7} based on the binary inputs I_1; I_2; I_3 and the conditions applied on the three enabling pins $\bar{E}_{i1}$; $\bar{E}_{i2}$; $\bar{E}_{i3}$. The DEC enables only when $\bar{E}_{i1}$; $\bar{E}_{i2}$; $\bar{E}_{i3}$operates at 0; 0; 1. For that, outputs of the RS-flip flop are used for enabling $\bar{E}_{i2}$, $\bar{E}_{i3}$ of both the DECs and $\bar{E}_{11}$is kept at low. Since the outputs of the DEC are inverted, only the decoded address bit stays at low, following the truth table as given in Tab.3.1. In this configuration, DEC-1 can assign eight addresses only. We use a pair of DECs in such a way that when a particular output $\bar{o}_{1n}$ (for any n = 0 to 7) of DEC-1 is at low, it gets connected to $\bar{E}_{21}$ of the DEC-2 for multiplexing the addressing output to sixty four. The schematic of the DACM is also shown in Fig. 3.4. In order to control the output, a reference voltage is given in a 16-bit digital format r_0;. . . r_{15} to a pair of eight input-and-eight output Latches, SN74HC373, which are connected in parallel within the DACM as shown in Fig. 1 (b). The particular address bit $\bar{o}_{2n}$, which is at low, is inverted using a NOT-gate and connected to LE of Latch-1 and 2. The latches become transparent only when their output control ($\bar{OC}$) and latch enabled LE terminals are 0 and 1, respectively. The duration over which the latch remains enabled depends on the TTL pulse width. Here, since

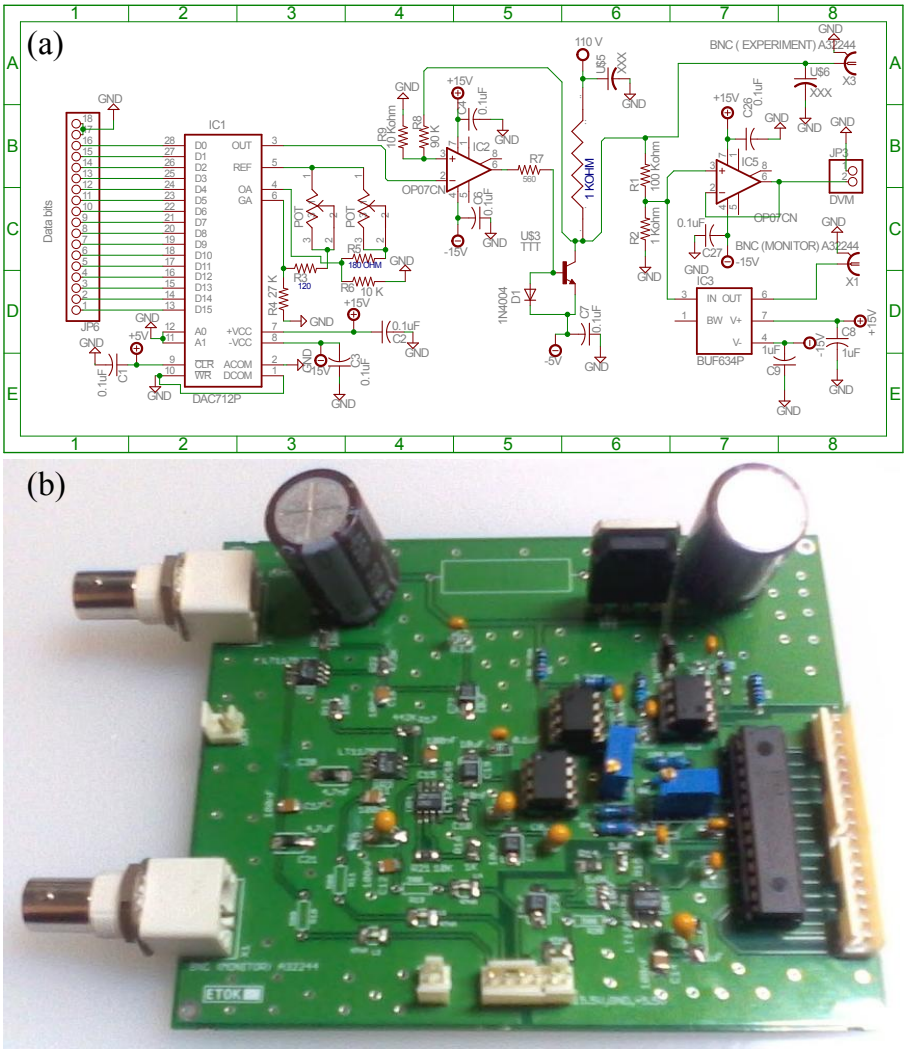

Fig. 3.6: (a) Schematic of voltage source which is designed in EAGLE V6.4 software and (b) populated PCB board.

OC are grounded, outputs $\bar{D}_0,\ldots\bar{D}_{15}$ of the Latch-1 and 2 follow their reference inputs in real time only when LE becomes high. Once the data bits pass through the enabled latches, an analog reference voltage is generated corresponding to $r_0,\ldots r_{15}$ by a 16-bit digital-to-analog converter, DAC712. For giving a different reference voltage, a new set of $r_0;\ldots r_{15}$ is sent from PC along with its address. The data bits reach to all DACMs that are attached to the data acquisition system but the ones that are addressed can only read it. This addressing module is versatile for all those equipment that require an analog electronic signal for controlling. The DACM allows a significant reduction in a lab's cable infrastructure: instead of point-to-point connections with individual cables, all equipment may be connected via a single digital bus that runs throughout the lab.

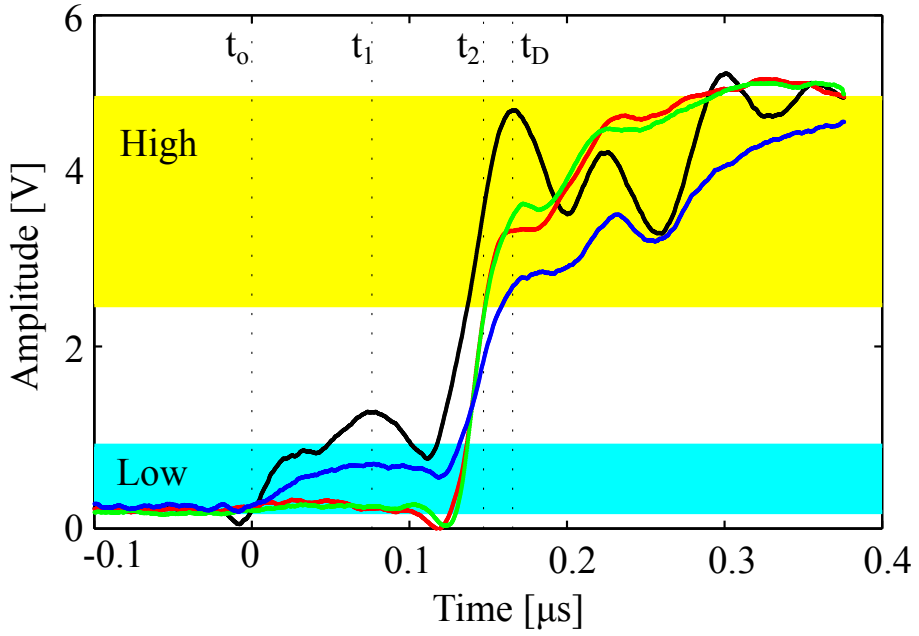

Fig. 3.7: Behavior of a digital BUS (black; red; green; blue) which is propagated through different strings of a 30 m long cable. Digital bits are at Low between 0 to 0.8 V and high between 2.5 to 5 V. At the end of 30 m cable the time dependent BUS are 0; 0; 0; 0 at t = t0; false; 0; 0; 0 at t = t1; 1; 1; 1; 0 at t = t2 and the desired 1; 1; 1; 1 at t $\geq$ tD.[77]

For the DC voltage source, the 220 V, 50 Hz AC is first converted to an unregulated DC voltage, V_{dc} = 120 V using combination of a step down transformer, bridge-wave rectifier and a filter. Further regulation and rectification of the ripples is obtained by using a discrete transistor shunt voltage regulator type configuration, as shown in Fig. 3.3(c). This unregulated DC consists of AC ripples which are typically on the order of few 100 mV. In this circuit, tuning of the output is done by varying the reference voltage rather than by varying any active component in it. The analog reference voltage V_{ref} which is generated by a 16 bit DAC-712 is compared with the rectified DC and the final output is self-corrected with the help of a transistor which is used as a control element. Output of the rectifier V_{dc} is current limited to 21 mA using a series resistance R_s with it. Since the range of V_{ref} is limited to 0-10 V, the comparator is established for the full range of V_{dc} by stepping it down to a factor. This scaling is done by using $R1$ and $R2$ in a voltage divider configuration which is like a sampling circuit. The $V_{in} = V_{dc}/10$ is compared with V_{ref} at the non-inverting and inverting terminals of an OPAMP and OP-07, respectively. Output of the OPAMP which is proportional to V_{in} - V_{ref}, is applied onto the base B of an NPN-transistor, BU-508, in common emitter configuration. A fraction of the maximum allowed current, V_{dc}/R_s gets diverted through the shunt voltage regulator which is proportional to V_{in} - V_{ref} . If $V_{in} > V_{ref}$, the current passing through the transistor increases which results in decrease of V_o since V_{dc}/R_s is constant, or vice-versa.

Tab. 3.2: Bill of materials to construct the DACM and voltage source

S.No	Items	Quantity
1.	LT1175	2
2.	LT1763	3
3.	Step down transformer	1
4.	Rectifier	5
5.	NPN transistor BU508	1
6.	OP07	2
7.	BU508	1
8.	16 bit DAC-712	1
9.	Monostable multivibrator 74LS123	1
10.	3 to 8 Decoder 74LS138	2
11.	Quad NAND Gate 7400	1
12.	8 bit Latch 74LS373N	2
13.	Right angle BNC PCB mount	2
14.	DB-25	1 pair
15.	8 pin header PCB mount	1
16.	18 pin header PCB mount	3
17.	Dual 8 pin header PCB mount	2
18.	Jumper	2
19.	2 pin header PCB mount	3
20.	6 pin header PCB mount	2
21.	Digital voltmeter	1
22.	3 pin power panel	1
23.	18 pin flat cable 0.5 m	2
24.	8 pin flat cable	1
25.	2 pin flat cable	2
26.	6 pin flat cable	1
27.	100k POT PCB mount	2
28.	10k resistance	5
29.	100k resistance	2
30.	90 k resistance	1
31.	1 k resistance	4
32.	500 resistance	2
33.	2 k resistance	2
34.	6k resistance	2
35.	150k resistance	2
36.	442k resistance	1
37.	50k resistance	1
38.	100 nF capacitor	50
39.	10 nf	10
40.	1μF	4
41.	10μF	2
42.	Power cable	1
43.	Toggle switch	1
44.	50 pin flat ribbon cable	1
45.	NI DAQ card with 50 PIN Digital I/O	1
46.	22 μF bypass capacitor for final output	2

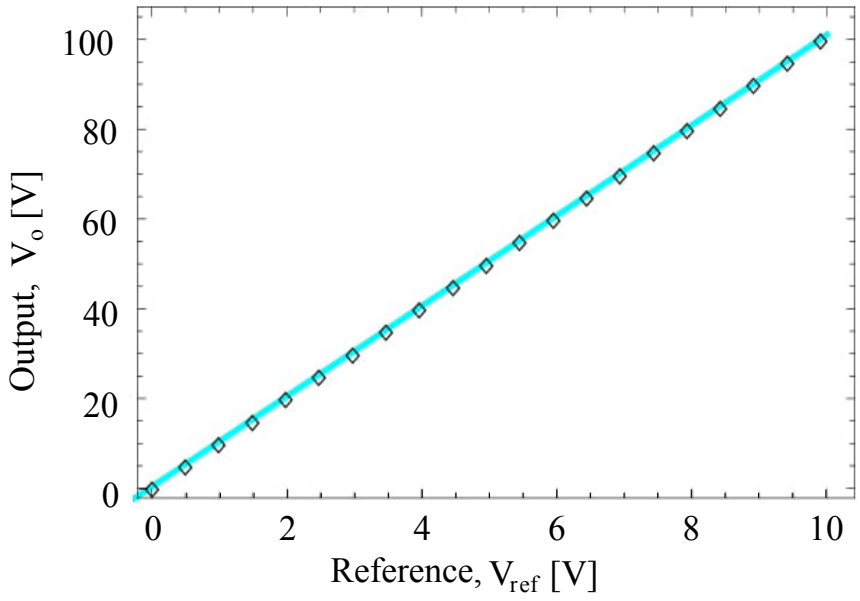

Fig. 3.8: Change of voltage source output with the reference voltage which is tuned from a PC. A linear fit to the data establishes our model. We use R_1 = 91kΩ, R_2 = 10kΩ, R_B = 3.9kΩ, R_s = 5.7kΩ, V_{dc} = 119 V, V_{BE} = 0.7 V, V_E = -4.9 V, β= 5 and A = 450 × 103. [77]

The emitter, E, of the transistor is biased at -5 V in order to keep it active in the vicinity of output voltage, $V_o = 0$ V. A diode is connected in between $B-E$ for protecting the comparator output current to pass through the transistor. In this way, the comparator equilibrates at V_o according to the V_{ref} within a transient time to produce an ultra-stable regulated output. For generating V_{ref}, we have used a 16-bit DAC, DAC-712, in order to achieve sub mV resolution at the output. In order to get a stable output of the DAC and hence a stable output of the voltage source, we separate the digital and analog grounds which are interconnected at one place. This resolution can be further improved by using an 18 or 32 bit DAC, but this will also require special arrangement for reducing fluctuation in the ground level. In our design we take care of the noise reduction in power supply which is connected to transistor and comparator and responsible for the system noise. In our power supply section, we first used unregulated DC voltage ±18V and ±7V from a bridge rectifier by using small tapping in transformer which generates 120 V from main output voltage. Then we use low noise adjustable voltage regulator LT1175 and LT1763 for negative and positive voltages for biasing the active components in the circuit. For further reduction of noise, we use LC filter in input and for output we use two type of bypass capacitors, one is polar high capacitance for low frequency noise and other is small ceramic capacitor for high frequency noise; the schematic of power supply section is shown in Fig. 3.5. Our module is simple in terms of design and uses off the shelf components in com-

parison to the commercially available FPGA based voltage sources, however provides similar stability and resolution. The schematic of the voltage source designed using EAGLE software, using which the PCB has been architectured is also shown in Fig. 3.6. List of components required for designing of the DACM and voltage source are given in Tab. 2.

3.4. Result and Discussion

The DACM uses a common address BUS consisting of 6 digital outputs (DOs) from DAQ card for reading a particular device, a data BUS consisting of 16 DO for writing data and a trigger pulse to start the bit transfer from DAQ to module. Fast sampling of data causes errors in output due to bit slip, which is mainly due to random propagation delay in Data BUS from DAQ to module through 50 pin flat ribbon cable. We first measured delays of four digital bits array after they propagated through 30 m long cables which are shown in Fig. 3.7. This data gives the limiting speed of our communication protocol because the trigger pulse width t_w used to provide discrete data to DACM is always greater than that of propagation delay. To ensure that no such data slips occur, we use pulse width timing 10 times more than the random delay. In this measurement, the approximated delay is 0.4(1) μs when using 30 m wire. If we extrapolate this result linearly, rough estimation of the speed of our DACM for delivering data to module is approximately 1.4 μ/m.

In Eq.3.6, it is clear that the output of the voltage source follows V_{ref} and their linear dependency can be established from simple analysis of the circuit as shown in Fig. 3.3 (c). Potential from feedback amplifier connected to transistor, which acts as a control element is equivalent to

$$V_{BE} + V_E = A(V_{in}–V_{ref})–I_B R_B, \tag{3.7}$$

where A is open loop gain of the OPAMP, V_{BE}, V_E are potentials across the base-emitter and emitter-ground, respectively, $V_{in} = V_0 \frac{R_2}{(R_1+R_2)}$ and $I_B = \mathrm{I}R_1$ - V_o + $\frac{V_A}{R_1\beta}$ for collector-to-emitter current ratio β of the transistor. The current $I = \frac{(V_{dc}-V_o)}{R_s}$ flowing through the circuit establishes the linear relation between V_o and V_{ref} as

$$V_o = \left[V_{ref} + \frac{V_{BE} + V_E + V_{dc} + \frac{\alpha}{\beta}}{A}\right]\left(\alpha_1 + \frac{\alpha_4}{A}\right)^{-1} \tag{3.8}$$

where $\alpha_1 = \frac{R_2}{(R_1+R_2)} R2/(R1 + R2)$, $\alpha_2 = \frac{R_B}{R_s}$, $\alpha_3 = \frac{R_B}{R_1}$ and $\alpha_4 = \frac{(\alpha_2+\alpha_3}{\beta}$ - $\alpha_1\alpha_3$.

Figure 3.8 shows operation of the voltage source which follows Eq. 3.8. Linearity percentage was calculated using values from experimental output and values obtained by using Eq.3.8

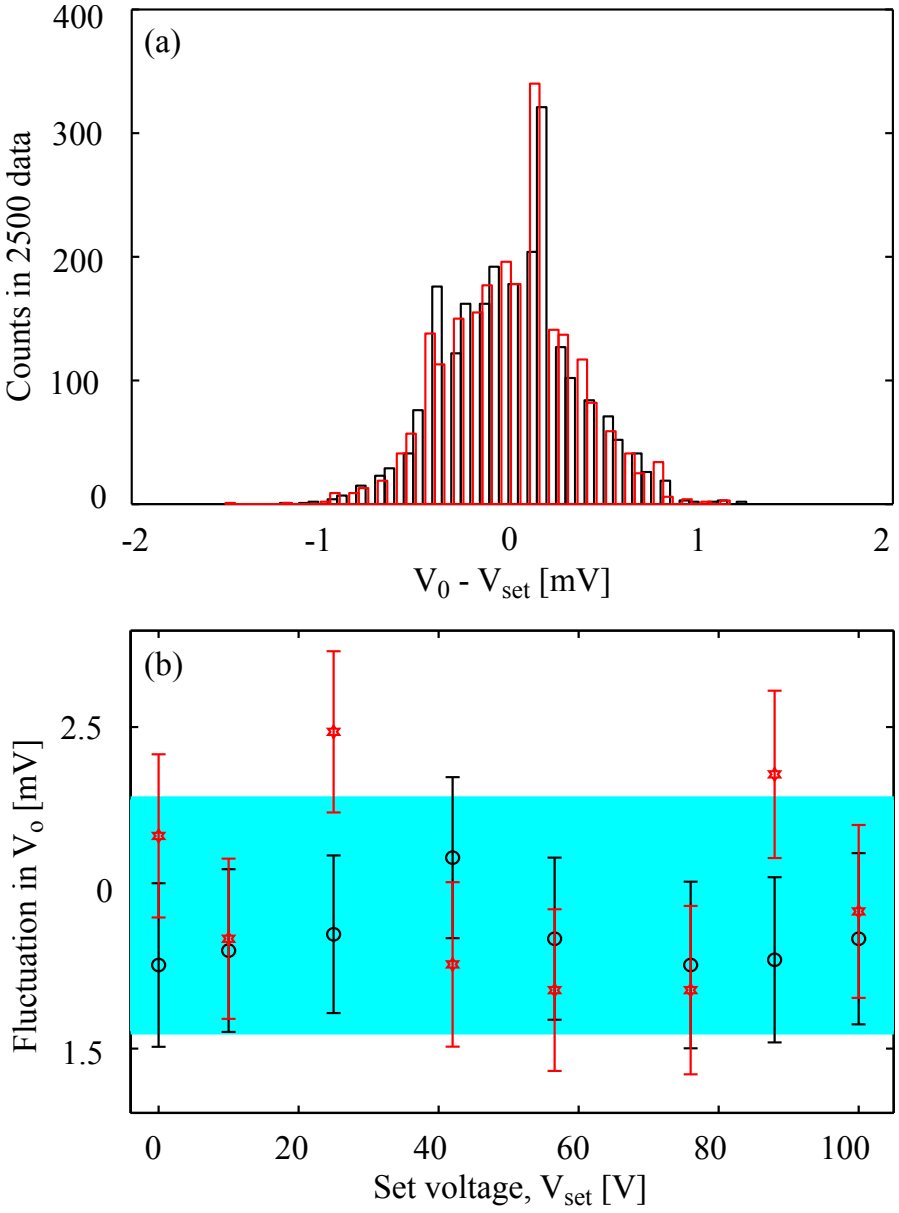

Fig. 3.9: Stability of the output after starting the voltage source (black) and after five hours of continuous operation (red). (a) Distribution of the output in 2500 data points during 500 s run time. This measures deviation of V_o from a desired set voltage. (b) Magnitude of the average fluctuation at different set voltages. The band (cyan) depicts mean magnitude of all the fluctuations over the range of operation, which is 1.90(36) V.[77]

and was found to be 99.52%. We also calculated linearity correlation of our experimental input and output data and we found that these data are correlated linearly with correlation coefficient 1.00007. These voltage sources have been operated for days to investigate their short and long term stabilities. The output voltages are averaged over 500 s, immediately after switching on

the sources and after 5 hours of operation as shown in Fig. 3.9. These Gaussian-shaped plots shows that the output voltage fluctuation arises due to random noise which is inherent in any module. The random noises in the figure are due to pickup noises arising during measurement. The outputs were recorded at intervals of 200 ms for a fixed set voltage V_{set} from a graphical user interface (GUI) in the PC and the corresponding V_{ref} $V_{set}/10$ was also recorded. The measured load regulation at different V_o is shown in Fig. 3.10. The value of resistance below which the approximation $I_3 = 0$ becomes invalid is termed as "critical resistance". The critical resistance, R_c, below which the voltage source is unable to produce the desired V_o is also depicted in the same figure. We have characterized the line regulation for a variation of input AC between 200 V - 240 V. The regulation is 0.001% for $V_o = 0$ to 86 V and increases up to 35% at $V_o = 100$ V due to limited supply of V_dc. The improvement of line regulation in region near 100 V is possible by decreasing the source resistance R_s which causes large current to pass through the transistor and it gets heated which increases the inherent noise of the transistor and causes error in final output voltage. In our experiment we not require any current and also our AC voltage supply in our lab is stabilized by central UPS, which gives reason for no further improvement required in this design. Figure 3.9(a) shows an example distribution for the deviation of V_o from the desired output. Full width half maxima of these histograms depict stability of V_o. The magnitude of the average fluctuation of the voltage source is determined to be 1.90(36) mV over its operating range 0-100 V. The transient behavior of the voltage source at switching on/off for different values of V_o has been investigated, which is shown in Fig. 3.11. For acquiring this transient behavior we operated the voltage source in switching mode at different frequencies up to 10 Hz. It has been observed that during switching ON, the voltage source overshoots before stabilizing at V_o (Fig. 3.11a). The transient switching ON/OFF times are independent of the switching frequencies within the resolved accuracy of our measurement. The average transient times for different outputs, at switching frequencies up to 10 Hz are shown in Fig. 3.11(b). In this module, the transient time is improved by decreasing the value of bypass capacitors which are used in output channel and by using fast DACs. Increase in the speed of our module however increases the noise level which decreases the stability of the output but as we use this module as a DC source, such modification is not required.

3.5. Application

Such a computer controlled voltage source has many applications mainly in high voltage region. From Eq.3.8, it is clear that the maximum output voltage is dependent upon the maximum DC unregulated voltage and the fractional part of the voltage used in sampling circuit. Hence, to achieve higher output voltage, no major changes has to be brought about in the circuit. As for example, to achieve 0-1000 V regulated output, 1/100 of the output voltage from a transformer

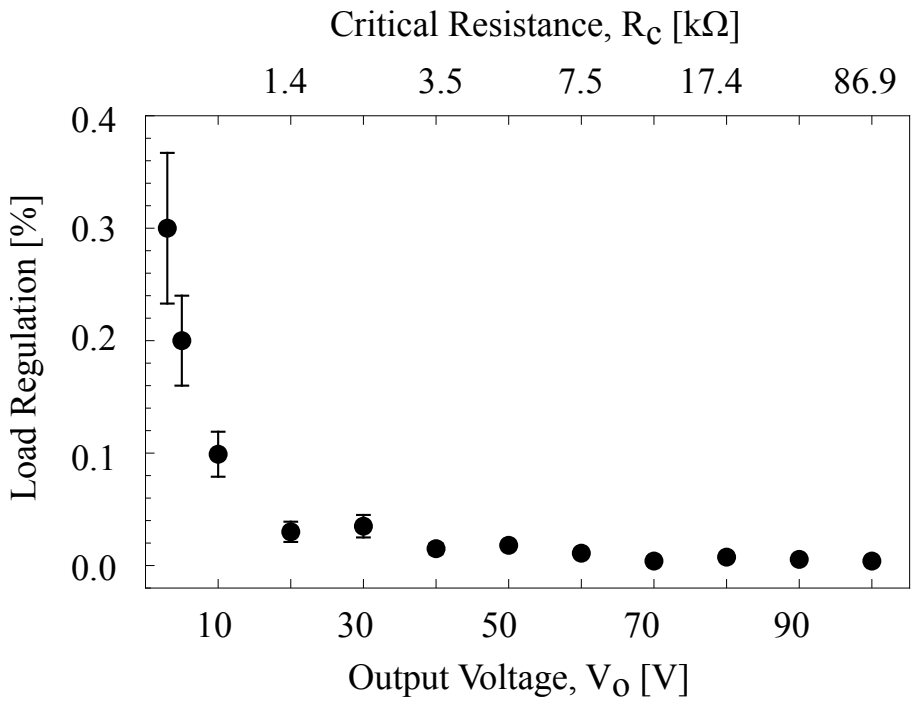

Fig. 3.10: Characteristic load regulation of the voltage source. The critical load below which the voltage source is unable to maintain a constant output is also depicted. [77]

with 1000 V output is transferred to the feedback to get the regulated output. This kind of universal and easy updating feature in the system makes it user friendly. It can therefore be used for high voltage biasing applications, such as, Geiger-Muller (GM) counter, Photo multiplier tube (PMT), ion traps, plasma related or discharge tube based experiments *etc.* This module is also able to generate any arbitrary waveforms such as, triangular, sinusoidal, sawtooth as shown in Fig. 3.12. In this figure, amplitude of the waveforms are kept at 0-40 V in order to measure the voltages in the available oscilloscope. The response of the waveforms is limited to a bandwidth of 0-10 Hz as it is also shown in Fig. 3.11. The minimum increment of the output is 3 mV which is limited due to 16-bit DAC. This resolution can be improved further by using 18 or 32-bit DACs. Such high voltage sources have wide range of applications, such as, driving of the piezos attached to an ECDL laser or biasing electrodes of an ion trap and so on. The triangular or sawtooth voltages are useful for smooth scanning of the laser frequencies in the ECDL lasers. On the other hand, position of the ions confined in an ion trap can be adiabatically tuned using our voltage sources.

3.6. Conclusion

We have discussed about the design and working principle of DACM in this chapter, which hooks up with every indigenously developed electronic module. Using this module, we make

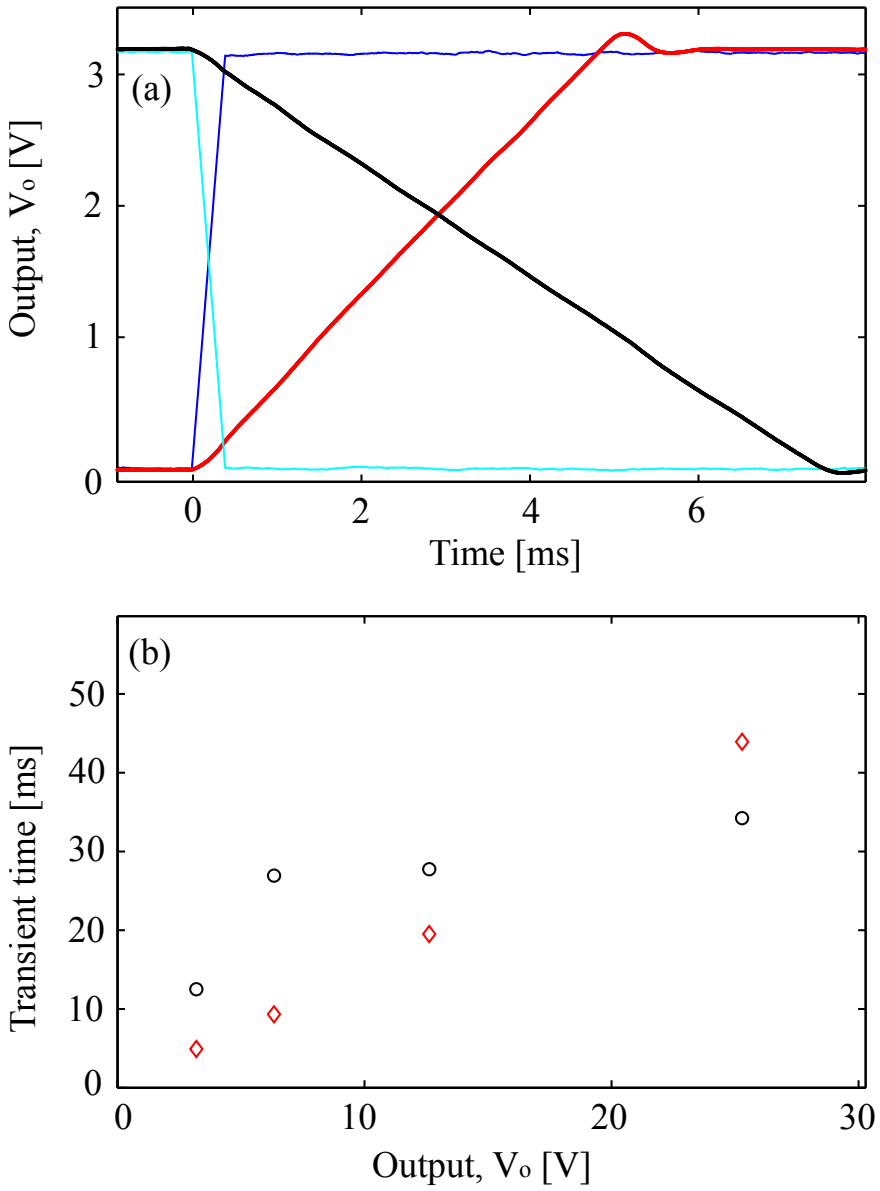

Fig. 3.11: (a) Characteristics of the switching on (red)/ off (black) of the voltage source corresponding to a V_{ref} which changes from zero-to-max (blue) and max-to-zero (cyan), respectively. (b) Mean transient times during switching on (red)/ off(black) at different switching frequencies of V_{ref} up to 10 Hz.[77]

our system fully computer controlled via single universal data bus, which avoids any extra mesh of wire in our laboratory for performing experiment. We have also developed a low noise DC voltage source which is used for biasing electrodes of the ion trap for controlling the motion of the trapped ion. This voltage source is able to generate 0 to 100 V with a resolution of 3 mV with a stability of $\pm 1.90(36)$ mV. The design of the voltage source permits the facility of changing its voltage range just by altering the voltage divider circuit keeping the other parts

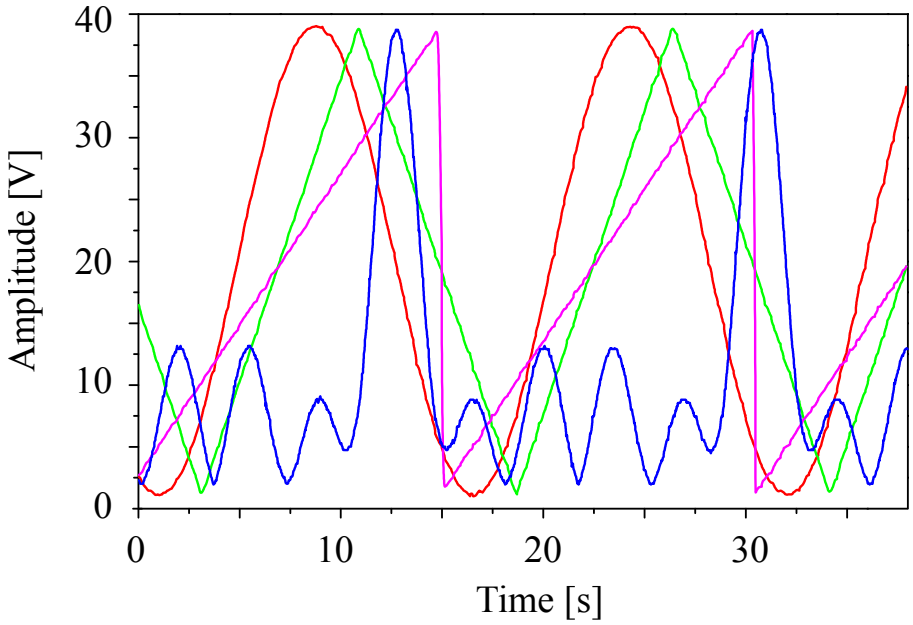

Fig. 3.12: Example waveforms: sinusoidal (red), triangle (green), sawtooth (purple) and arbitrary (blue)generated from the DC voltage source.[77]

intact. This voltage source is also a programmable one and thus can also be used as a low frequency waveform generator. This kind of multipurpose voltage source has many applications like tuning piezos, scanning length of a Fabry-Perot cavity, biasing of Photo multiplier tube *etc.* A comparison with the commercial high voltage sources show that they have lower voltage stability as compared to ours and also long term voltage stability depend upon the output voltage of the source, which makes our system better.

Chapter 4

All Digital Universal Automatic Relockable Servo Controller: FPGA Based Lock-in Amplifier & PID Systems

Publication: A. Roy, Lakhi Sharma, I. Chakraborty, S. Panja, V. N. Ojha, and S. De, An FPGA based all-in-one function generator, lock-in amplifier and auto-relockable PID system, JINST **14**, 05012 (2019).

4.1. Introduction

Many experiments related to atom- photon interaction require a stable laser frequency source. Stabilization of laser frequency is done via a servo controller which locks a desired frequency setpoint with respect to a stable reference point. Stability of the locked point therefore depends upon the stability of reference point, bandwidth of the servo control and the locking technique used. According to modified Schawlow and Townes formula [78] by Melvin Lax, the linewidth of a laser is

$$\Delta\nu = \frac{\pi h f(\delta\nu_c)^2}{P_{out}}, \tag{4.1}$$

where, f is central frequency of laser light, P_{out} is output power from laser and $\delta\nu_c$ is FWHM of the laser's cavity linewidth. This formula is modified for diode laser, where we add a factor (1 + α^2) to this eq. 4.1, where α is linewidth enhancement factor of the gain medium. Equation 4.1 is based on the assumption that spontaneous emissions into laser mode introduce noise amplitude during each round trip which causes change in amplitude and phase. Due to the phase fluctuation in system and absence of restoring force, phase undergo random walk and lead to phase noise power spectral density and causes linewidth. However, while performing experiments, additional noise sources such as instability in cavity length, electrical noise, *etc.* increase the line width of laser.

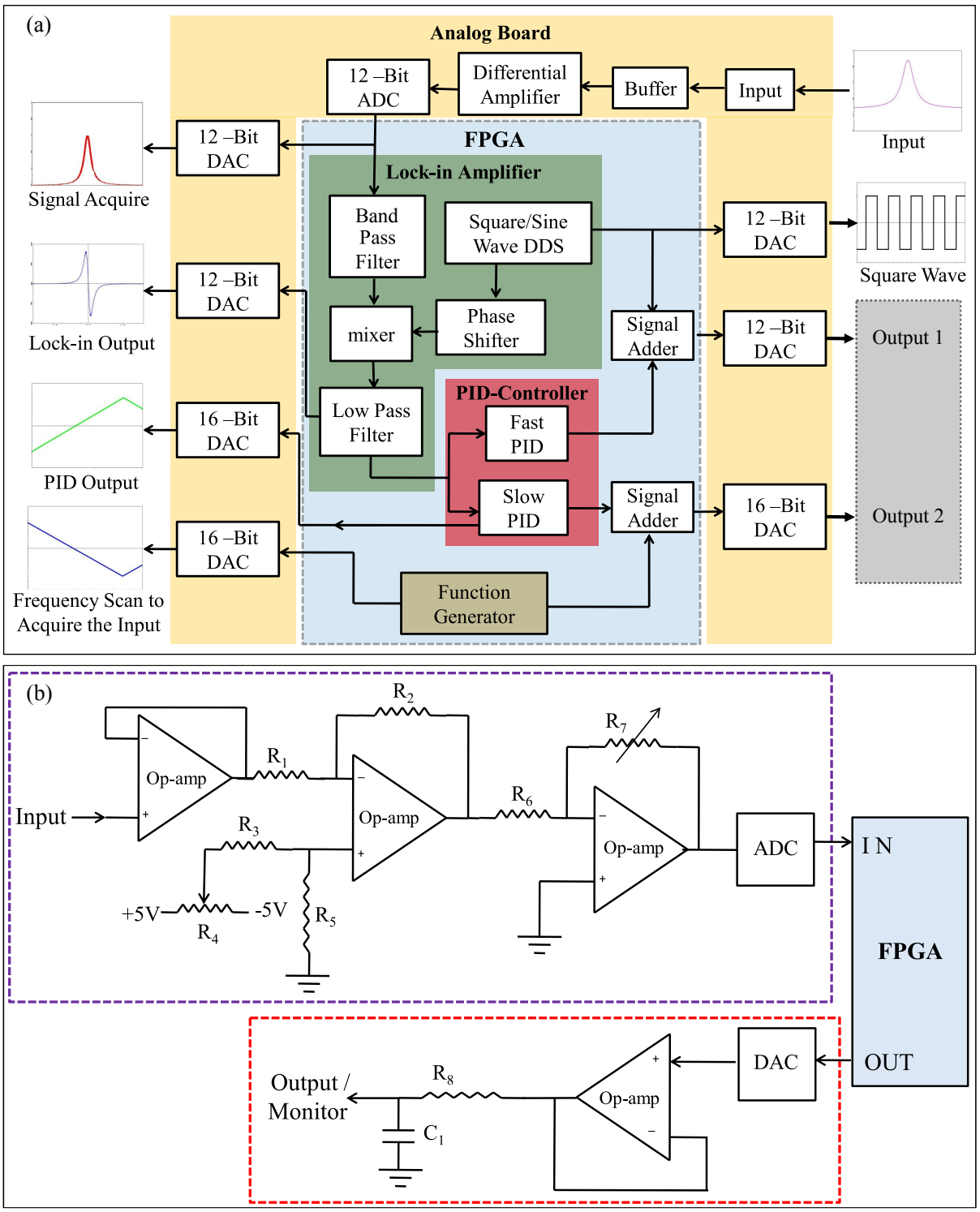

Fig. 4.1: (a) Block diagram of the instrument showing constituent of the external interfacing hardware, lock-in amplifier, PID and function generator, (b) schematic of the interfacing hardware.

Our experiment requires External cavity diode lasers (ECDL) at precise frequencies for different purposes. ECDLs have a spectral linewidth of few hundreds of kHz and therefore require a frequency stabilizer to lessen the instabilities of its external cavity length and diode laser current noise. Change in cavity length (optical length) due to environmental changes can be compensated by feeding the required feedback voltage to the piezo driver of the crystal attached to the cavity mirrors, using a servo controller. The same can also be employed for suppression of current noise by feeding the feedback signal to laser's current driver which is responsible for providing current to laser diode, thus stabilizing fast frequency fluctuations and reducing the laser linewidth. Several techniques and modules for servo controller for stabilizing the laser frequency are discussed in Refs. [79, 80, 81, 82]. Among these techniques, we use Pound Drever Hall technique, which encompasses different modules like function generator, lock-in amplifier,Proportional-Integral-Derivative (PID) controller, photodiode amplifier, filters, *etc.* In our experiment, we have five different lasers and three Fabry Perot cavities to be stabilized using this technique. To lock them, we require eight lock-in amplifiers, eight photodiode amplifiers, sixteen function generators and sixteen PID controllers in total. These components will introduce electrical noise during the signal transmission from one module to another, enhance space problem and mesh of wires around the modules in the lab. To avoid these issues, we use Field Programmable Gate Array (FPGA) so that all the said components can be programmed on a single chip, thus giving a compact and cost-effective solution.

Field-Programmable Gate Array [83, 84] can process digital signals following the user specified algorithms to implement various gate operations, filters, mixer *etc.* In new series, FPGA has Random Access Memory (RAM) and First-In First-Out (FIFO) for data buffering, large digital signal processing (DSP) slices for high performance filtering, clock management tiles for direct digital synthesis (DDS) implementation and large number of input/output (I/O) pins for performing fast data interface. Due to versatility, FPGA has gained immense boost because it is easily configurable and reconfigurable without any hassles of soldering or desoldering. Digital signal processing is insensitive to noise pickup during execution of the algorithms, which enhances overall performance of the device. Nowadays, FPGA based devices are popular as their customization enable the experiment to reach beyond the level of standard analog devices, where high bandwidth is not a requisite. FPGA implementation of photon counting [85], real time data acquisition [86], arbitrary waveform generation [87], high quality filter [88] and so on are thus widely used. In particular to the lock-in amplifier and PID controller, which are focus of this article, Morris et al. first conceptualized the digital phase sensitive detection [89, 90]. In the area of lasers and optics, Sparkes et al. first showed scalable system for locking multiple optic parameters [91] and at the same time, laser frequency stabilization was demonstrated by Schwettmann et al. [92]. Since then, many groups have developed such systems [93, 94, 95, 96, 97] for improving the feedback quality [96].

Keeping these wide range of applications in mind, particularly for low bandwidth general applications [98], we have developed a compact, computer controlled instrument that integrates scan generator, lock-in and PID. A simple PID, in case of deviation beyond the servo's limit, becomes incapable to lock any more at the setpoint. In order to retrieve the lock without any human intervention, we have also developed an automatic relocking mechanism, which enhances effectiveness of an experiment with minimum interruption. Earlier, analog as well as digital control circuits have been demonstrated for automatic relocking laser frequency to transmission spectrum of a resonant Fabry-Perot cavity [99, 100]. Laser frequency stabilization is also demonstrated by using a complex pattern matching algorithm of atomic absorption spectrum programmed in a digital auto lock controller [101]. Such algorithm relies on proper fitting to the spectral feature as the instrument can be inefficient due to improper fit. In comparison to these, our relock mechanism is simpler, robust, faster and generalized, which as a whole decreases the dead time upon unlocking of the set parameter. In this chapter, we have therefore given description of hardware, software and user interface of the instrument along with detailed characterization of each programmed module. The indigenously designed and developed device not only serves for our purpose but is also universally applicable in other experiments as well where there is a requirement of PID, lock-in amplifier an function generator. To justify the universality of our device we have demonstrated its use in two other experiments, Auger spectroscopy and low coherence optical tomography.

4.2. Design

The layout and arrangement of modules and submodules programmed inside the FPGA are shown in Fig. 4.1(a). The analog signal coming from an experiment (input) is first needs to be digitized for further Digital Signal Processing (DSP) inside the FPGA. It is first passed through an analog to digital convertors (ADC), after processing, it then goes through digital-to-analog conversion followed by low pass filter for noise suppression to make it useful (output 1 and 2). The hardware part of the device therefore performs digitization of the input analog signals, analog output generation and suppression of the high frequency noise. Suitable logics and proper algorithms are programmed in the gate-array circuit to make it a unique and fast operational device. A Python based user-friendly Graphical User Interface (GUI) is enrooted for remote controlling of the instrument and plotting the acquired data almost in real time. The following subsections describe the hardware, firmware and GUI designs in detail.

4.2.1 Hardware

The hardware part of module consists of two printed circuit boards (PCB), an FPGA evaluation board (Digilent CMOD A7 35T) and an interface board for bridging the gap between analog

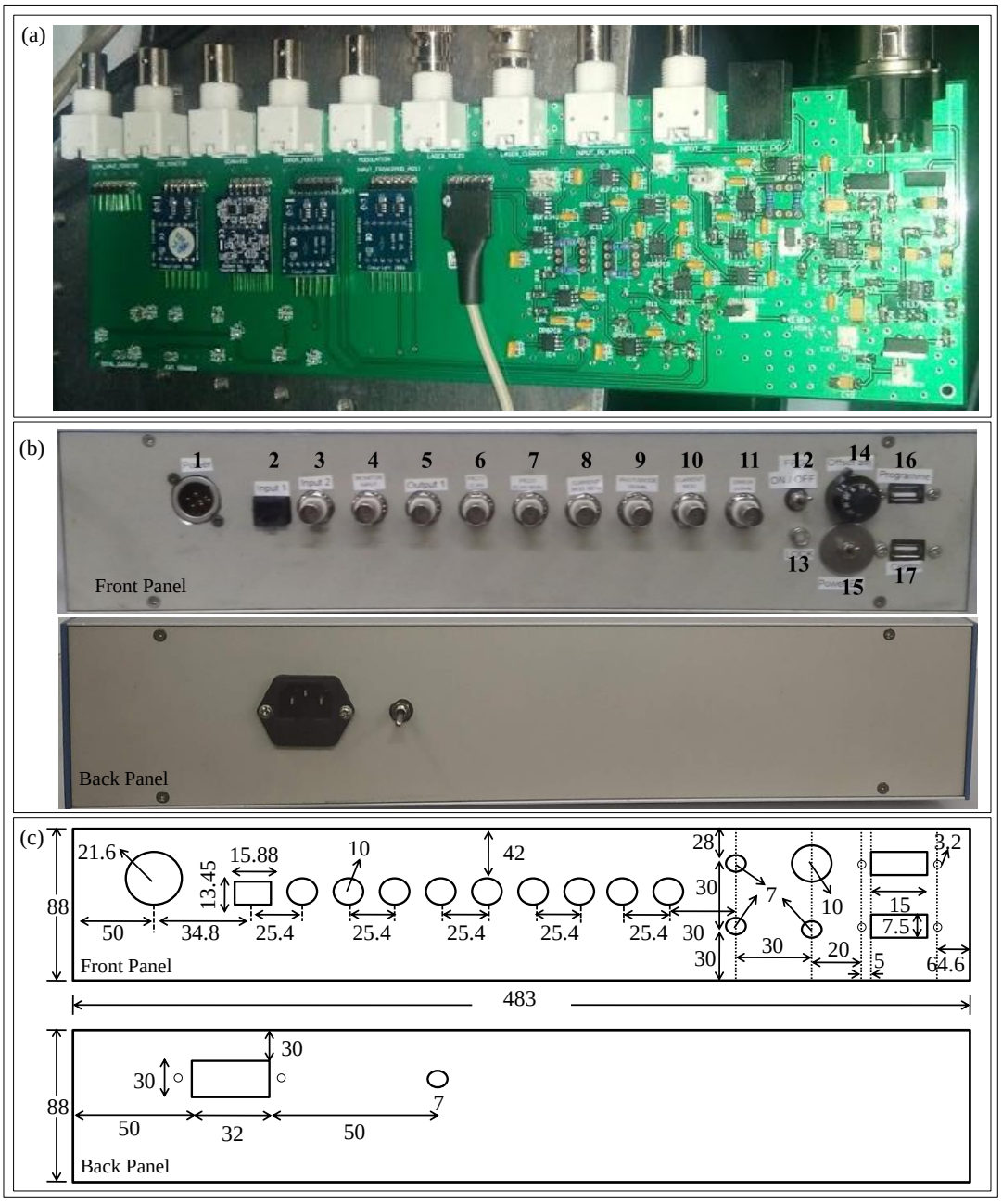

Fig. 4.2: (a) Populated PCB of analog interface board between analog signals and FPGA, consisting of DACs, ADCs and amplifiers. (b) Front and back panel of developed instrument containing the assembled interface PCB and FPGA evaluation board (front panel contains (1) Power, (2-4) Input, (5) Monitoring the PID output, (6) Output of scan generator, (7) Feedback output, (8) Output of lock-in amplifier, (9) Monitoring of the input, (10) Output of the AC coupled feedback, (11) Function generator, (12) FPGA On/Off switch, (13) Dual colour LED for indicator, (14) DC offset adjustment, (15) Power management switch, (16) USB for programming the FPGA and (17) USB for remote controlling the instrument). (c) Schematic drawing of front and back panel of the box along with dimensions for fabricating the complete servo controller.

and digital signals. The evaluation board has 48 digital I/O for signal processing; 2 channel Universal Asynchronous Receiver-Transmitter (UART), one for programming and other for communication between computer and FPGA, a 12 MHz clock and an optional slot for 100 MHz clock if required. For fast processing, we have inserted and used a 100 MHz clock (ASEM1-100.000MHZ-LC-T). The interface board which decides factors such as noise, bandwidth and gain of input and output signals used for laser locking, consists of differential amplifier, buffer amplifier, RC type filters, ADCs and DACs. The board is designed such that no ground loops are formed due to interface of digital and analog signals. To avoid added noise in the circuit, separated ground planes for digital and analog signals have been built. The input signal first passes through a low noise buffer amplifier (MAX4200) and successively through an opamp based differential amplifier (MAX4304). The later fulfills two purposes of changing the DC voltage offset of - 5V to +5V and providing gain of 0 to 1000 to the input signal. The subsequent signal then leaps over a 12 bit 1 MSPS ADC which has a detection limit of 0 to 3.3 V and 1 mV resolution. The differential amplifier puts the input signal into that limit, making it compatible for the ADC so that no information is lost by ADC. The ADCs used in the circuit is a commercially available two channel Digilent PMOD AD1 which uses IC AD7476A and a 20 MHz clock for sampling. The digitized and processed output from FPGA is passed through a 12-bit DAC (DAC121S101) at 1.8 MSPS and 30 MHz clock speed for fast servoing. Another 16-bit bipolar converter DAC714 with a resolution of 0.1 mV and speed 85 kSPS is also available in the circuitry for precise but slow operation, such as waveform generation for laser frequency scan via tuning its piezo. The components used to design this FPGA module are listed in Tab. 6.2. The populated Printed Circuit Board (PCB) of the analog interface where all these components have been soldered and the 2U box with the front and back panel, where this board has been assembled has been shown in Fig. 4.2 along with the relevant dimensions.

4.2.2 Firmware

The modules used for Pound Drever Hall technique locking are programmed on the FPGA using VHDL *i.e.*, very high speed integrated circuit + Hardware description language in Xilinx platform (Vivado 2017). Implementation of various modules such as, function generator, lock-in amplifier, PID controller, IIR based high and low pass filters onto the FPGA have been accomplished using VHDL programme. All the modules are programmed to be triggered at rising edge of the system clock which give a controlled manner for DSP. The details of the algorithms are discussed in this section.

Tab. 4.1: List of items required and the parts number that we made for designing this servo controller.

S.No	Items	Quantity
1.	CMOD A7 35T	1
2.	19 inch 2U Rack mount Box	1
3.	± 15 V and ± 5 V SMPS	1
4.	6 Pin Female connecting wire	6
5.	USB-UART cable 1 m	1
6.	USB Female-Male adapter	1
7.	USB cable 5m	1
8.	Three color low power panel mount LED light	1
9.	10 K panel mount potentiometer	1
10.	Toggle Switch	1
11.	LT1175 SMD	2
12.	LT1763 SMD	2
13.	Buf-634 SMD	3
14.	MAX-4204	11
15.	MAX-4304	2
16.	DAC714	3
17.	PMOD AD1	1
18.	PMOD DA2	2
19.	6 pin header	6
20.	47 nH Inductor	4
21.	100 nF ceramic capacitor	50
22.	4.7 μF polar capacitor	4
23.	1 μF polar capacitor	4
24.	10 μF polar capacitor	4
25.	10 nF ceramic capacitor	10
26.	1 μF polar capacitor	4
27.	100k POT PCB mount	5
28.	27k SMD resistance	6
29.	100 SMD resistance	8
30.	1k SMD resistance	8
31.	150k SMD resistance	2
32.	47k SMD resistance	1
33.	10k SMD resistance	4
34.	12k SMD resistance	1
35.	3.2k SMD resistance	1
36.	442k SMD resistance	1
37.	Female BNC right angle PCB mount	9
38.	XLR Male PCB mount (Optional)	1
39.	Ethernet port PCB mount(Optional)	1

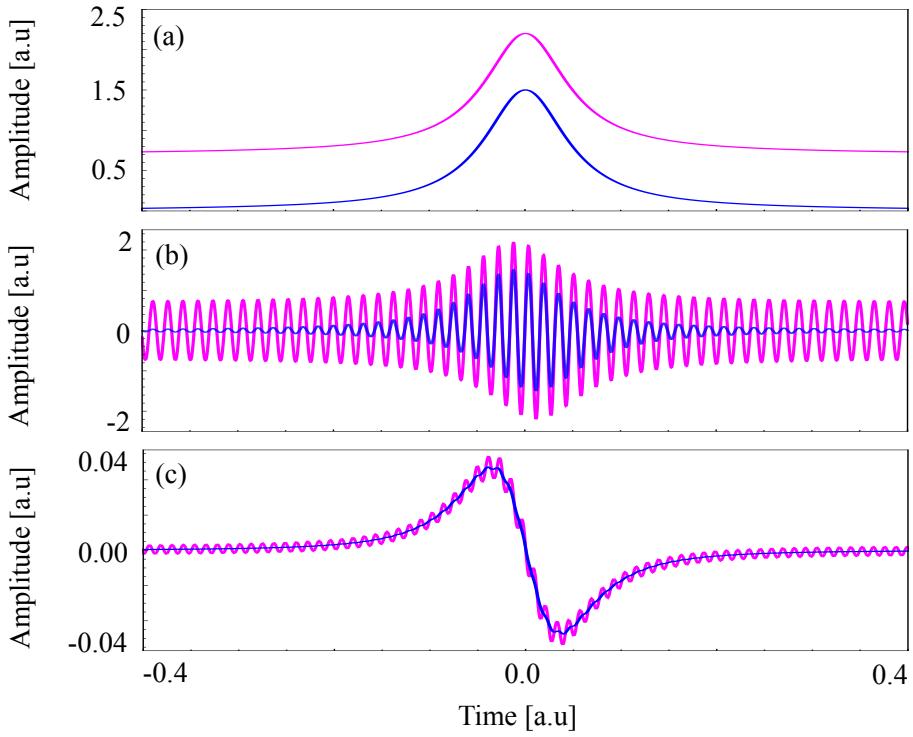

Fig. 4.3: Simulation results showing a Lorentzian signal with (Magenta) and without(Blue) DC offset being used as (a) input signal to the lock-in amplifier module. (b) After mixing the signal with the bipolar reference signal (c) After passing through a low pass filter.

Function Generator

A high frequency sine/square wave is required in the locking technique for current modulation which is used for generating phase sensitive detection through lock-in amplifier. There is also a requirement of slow triangular/sawtooth wave for scanning/tuning the laser frequency and searching for resonance peak to be used as reference peak for stabilization. These required waveforms at different frequencies are generated via the module programmed in the FPGA using its internal clock and programmable counters. Different algorithms are used for generation of these waveforms. For square wave generation, we use a counter that repeatedly counts every tick of master clock upto the quotient of the master clock frequency to the square wave frequency. To generate the desired frequencies, we setup state logic that goes active HIGH and active LOW in every successive counting. This technique is also used for sinusoidal and triangular wave generation but there it counts the output for the triangular wave and a numerical value taken from the sine-table for the sinusoidal wave.

Tab. 4.2: Values of coefficients and total bits allocated to parameters associated with the filters

Parameters	Low Pass Filter	High Pass Filter	PID Controller
ΔT	$1/2^{21}$	$1/2^{19}$	$1/2^{22}$
Filter coefficient	$\alpha_L = f_c/2^{21}$	$\alpha_H = f_c/2^{19}$	
Input	(i) 24 bits (ii) 16 bits	16 bits	16 bits
Equation Output	61 bits	61 bits	61 bits
Main Output	(i)16 bits - 43 downto 28 (ii) 16 bits - 35 downto 20	16 bits - 35 downto 20	16 bits - 35 downto 20

Lock-in amplifier

The new generation lock-in amplifier generally requires a reference frequency which splits into two parts with a phase difference of 90^o for complete quadrature study. When any input signal, the Fourier components of which is not known, is fed to the lock-in amplifier, multiplied with these two reference frequencies and passed through a low pass filter, two outputs, X known as in phase component and Y called as quadrature component are obtained. The spherical polar coordinates $R = \sqrt{X^2 + Y^2}$ and $\theta = tan^{-1}\frac{Y}{X}$ along with X and Y then gives complete information about the input. In our experiment, the input signal has only single fourier component ($cos\theta$ or $sin\theta$) and so single mixer and filters are required for phase sensitive detection, thus making it simpler. For digital implementation of these modules, a 12-bit signal is multiplied with a 12-bit reference produced by the function generator giving a 24-bit output, which passes through a low pass filter. The logic used for the IIR type filter is

$$O_n = I_n \times \alpha_L + O_{n-1}(1 - \alpha_L), \tag{4.2}$$

where, O_n and I_n are the n^{th} sample of the output and input data, respectively. Here, α_L $= 2\pi f_c \Delta T(2\pi f_c \Delta T + 1)^{-1}$ with f_c being the cutoff frequency of the filter and ΔT is sample interval of the input, which is processing time of single input sample for the programming. For performance test of the lock-in amplifier, a frequency modulated Lorentzian signal of the form

$$F(t) = F_o + \frac{a}{b^2 + [c - (d\,t + e\,\sin(\omega_m t))]^2}, \tag{4.3}$$

is propagated and processed through various sub-modules. Here, *a, b, c, d* are the numerical constants, $\sin(\omega_m\, t)$ is used to modulate the signal at frequency ω_m, F_o is the DC offset.

The effect of DC offset on output of lock-in amplifier is shown in Fig. 4.3, where two input signals with and without DC offset are considered in Fig. 4.3(a). On multiplication with a reference signal, the signal with DC offset gets amplified as compared to the one with null offset (Fig. 4.3(b)). Due to this extra amplification, additional noise ripples arise in its output signal, whereas the output of the signal with zero offset is smoother as shown in (Fig. 4.3(c)). The extra noise ripples are reduced by using a lower cutoff frequency low pass filter. In lock-in amplifier measurement, use of lower cutoff frequency low pass filter in output decreases the bandwidth of the measurement thus causing information loss. In our experiment, the signal input to the module has a small DC offset which creates noise in the output. If the DC offset is quite high, it is also responsible for data overflow during DSP. To avoid these complications, we use a bandpass filter using a combination of high and low pass filters before the digital mixer. The signal on passing through a high pass filter gets rid of any DC offset intrinsic to the signal and after that it pass through a low pass filter for smoothing the signal. The high pass filter is implemented using the equation,

$$O_n = \alpha_H O_{n-1} + \alpha_H (I_n - I_{n-1}), \tag{4.4}$$

where $\alpha_H = (2\pi f_c \Delta T + 1)^{-1}$. We use fourth order highpass filter where each of them follows Eq. 4.4. After this, the signal is multiplied to a reference $A_o \sin(\omega_m t + \phi)$, where ϕ is the additional phase relative to the reference. The modulated signal passes through a fourth order low pass filter, where the first stage is configured in 24-bit and three successive stages are in 16 bit, for efficient removing of the high frequency component. The rolloff of the filters do not have significant improvement with further higher orders. At the end of the lock-in amplifier's operation, the signal has the form,

$$F_1(t) = \frac{e\, A_o}{2} \frac{dF(t)}{dt} \cos(\phi). \tag{4.5}$$

This output of the equation is also called phase sensitive detection (PSD), which gives information about the derivative of the spectra. ϕ has to be optimized for better results. Algorithm to execute the low and high pass filters requires 1-8 and 1-13 rising edges, respectively, of the FPGA's clock pulse that operates at 100 MHz. This gives $\Delta T_L = 8/10^8$ s and $\Delta T_H = 13/10^8$ s for low and high pass filters, which are negligible as compared to $1/2\pi f_c$. Hence, α_L can be approximated to $2\pi f_c \Delta T_L \cong f_c/2^{21}$ and similarly $\alpha_H \cong 1 - 2\pi f_c \Delta T_H \cong 1 - f_c/2^{19}$. The bits allocation of parameters associated with the filters are given in Table 4.2.

PID Controller with Relock mechanism

The mathematical description to programme a PID controller is described in Ref. [102], where as per the user's requirement, there are three kinds of algorithms used for programming three

Tab. 4.3: Values of coefficient in different PID types

Type	α	β	γ
A	$(e_n - e_{n-1})$	$\Delta T\, e_n$	$\frac{(e_n - 2e_{n-1} + e_{n-2})}{\Delta T}$
B	$(e_n - e_{n-1})$	$\Delta T\, e_n$	$-\frac{(I_n - 2I_{n-1} + I_{n-2})}{\Delta T}$
C	$-(I_n - I_{n-1})$	$\Delta T\, e_n$	$-\frac{(I_n - 2I_{n-1} + I_{n-2})}{\Delta T}$

PID controller types *viz.* A, B and C type. These three types have been programmed in the FPGA using VHDL language [103]. The choice of PID is specific to their performances in an environmental disturbance as well as to the user's specific requirement. As for example, in type C PID, whenever there is a change in the setpoint, integrator (I) part of the controller gets activated first, followed by proportional (P) and derivative (D) modules. This avoids any overshoot during setpoint stabilization. Type C PID is therefore useful for our requirement. The general equation for PID controller is,

$$O_n = O_{n-1} + \alpha K_P + \beta K_I + \gamma K_D, \tag{4.6}$$

where values of α, β, γ for all PID types are given in Table 4.3 and the bit allocation for various parameters and input and output data intervals are given in Table 4.2. X_o is the set-point and $e_n = (X_o$ - $I_n)$ is the error signal, K_P, K_I, K_D are the proportional, integral and derivative gains coefficients, respectively. As in Eq.4.6, each submodule in PID require its gain coefficient and the choice of the gain coefficients is critical for obtaining a reliable and stable lock, which can be tuned from the PC, in our instrument. Dual stages of PID with DC & AC coupled operations and possibility of reversing their polarity have been implemented, which can be utilized as per the requirement. As an example, for laser frequency stabilization, dual stage PID is used for servo controlling of both piezo and current. In the AC coupled PID, we use an additional high pass filter at the output and a large K_I which prevents the system from sudden fluctuations and suppress the current controller noise.

We have also developed a simple additional algorithm in PID for those experiment where more than one setpoints are available in the experiment like laser frequency stabilization where the zero point in error signal is present for all spectra. A new relock mechanism feature is introduced in the PID, which records the uniqueness of the initial state, where PID is first locked. If during experiment, the lock point changes from one state to another with same setpoint value, then the corresponding algorithm helps the system to identify its initial state and stabilize/lock to it. In relock mechanism, plant output is used as reference when system is initially locked,

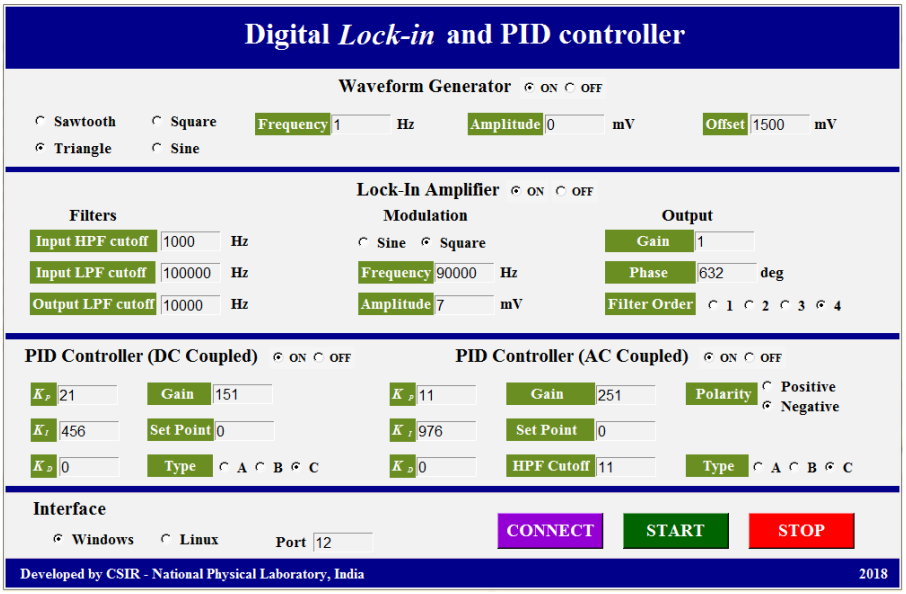

Fig. 4.4: The graphical user interface (GUI) panel for remote operation of the designed instrument. The GUI display consists of four sections which gives the option to (a) choose type of waveform, (b) operate the lock-in amplifier by controlling various parameters for filters, modulation and output, (c) optimize the controlling parameters of a PID, and (d) choose operating system and COM port.

then it is compared with the present value. There is a possibility that some small electronic fluctuations like DC offset or AC pickup noise may interrupt during the monitoring event of the relock module (RM) is going on, in such cases, the relock mechanism checks and compares the previous values and changes the reference plant value with respect to time. If there is large change in plant output with respect to present value then it switches OFF the PID controller and ON the Scan generator and searches for the initial lock state by changing the offset of the scan. During each scan of RM, it locks the system and takes the plant output and compares it to the reference. If it does not match, then it changes the offset of scan and again locks to another point until the plant output matches with the reference value. In this way it searches the initial state and if it not able to find it due to voltage limitation then it switches OFF all the PID controller used for stabilizing the system.

4.2.3 Graphical User Interface

In our servo controller, there are many modules and submodules which require input parameters for waveform generator, lock-in, PID once at a time or simultaneously for stabilization of the system. The parameters input to the module is given through computer using a user friendly GUI. The designing of the GUI is done in Python 3.7 platform, and serial communication protocol is used between computer and FPGA with 9600 baud rate (depends on user

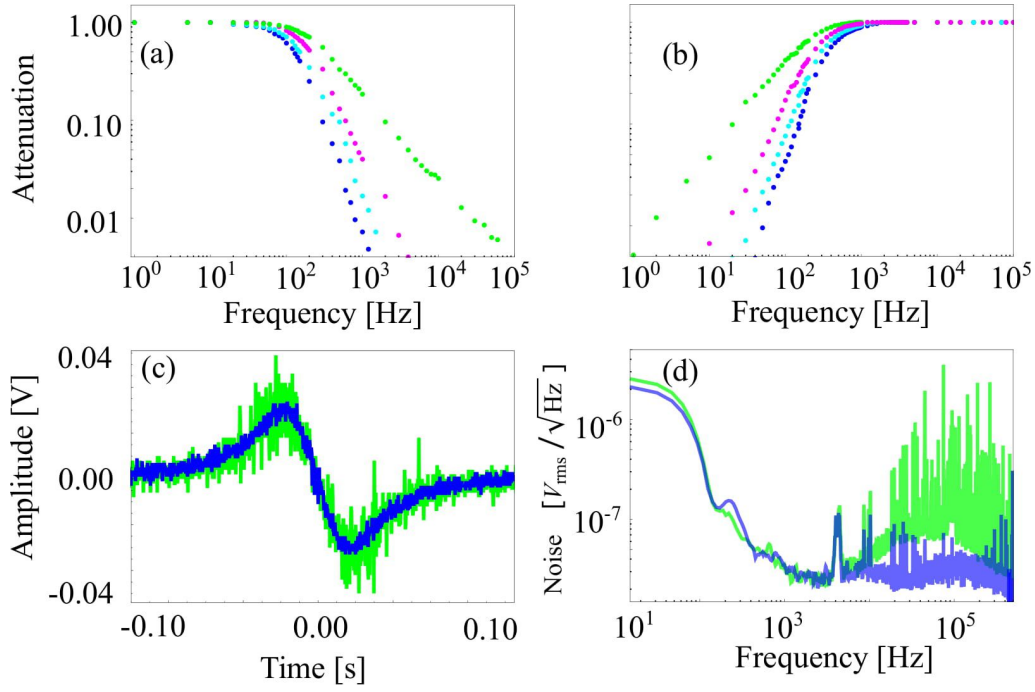

Fig. 4.5: Frequency response of the first (green), second (magenta), third (cyan) and fourth (blue) order of (a) low and (b) high pass filters. (c) Lock-in amplifier's output using the first (green) and fourth (blue) order filters and (d) its corresponding noise density.

requirement) as shown in Fig. 4.4. An FTDI chip is present in the FPGA board which converts USB signal to RS232 using USB-UART connectivity wire. The bit allocation for each input in GUI is 32 bit which is further divided into four equal parts and each part is 8 bit which is one of the necessary conditions for serial communication. As soon as the parameters are received by FPGA, they are restored as 32 bits and finally passed to the respective module. The important part for programming the GUI in serial communication is to follow the same pattern serially for transmitting data from computer to FPGA and receiving it back from FPGA to respective modules.

4.3. Characterization and Discussion

Various modules and submodules in the developed servo controller need to be characterized for better measurement and stabilization of the system. All modules are programmed to be triggered at rising edge of the master clock and the input data are sampled through a 1 MSPS, 12 bit ADC of resolution 1 mV which is able to detect signal upto 100 kHz with a noise bandwidth of 500 kHz as per the Nyquist theorem [104] giving a quantum noise 12 μV. The system's bandwidth and noise during the DSP is completely dependent on these ADCs; for improving these parameters for use in other application, PMOD AD1s are to be replaced by other ADCs

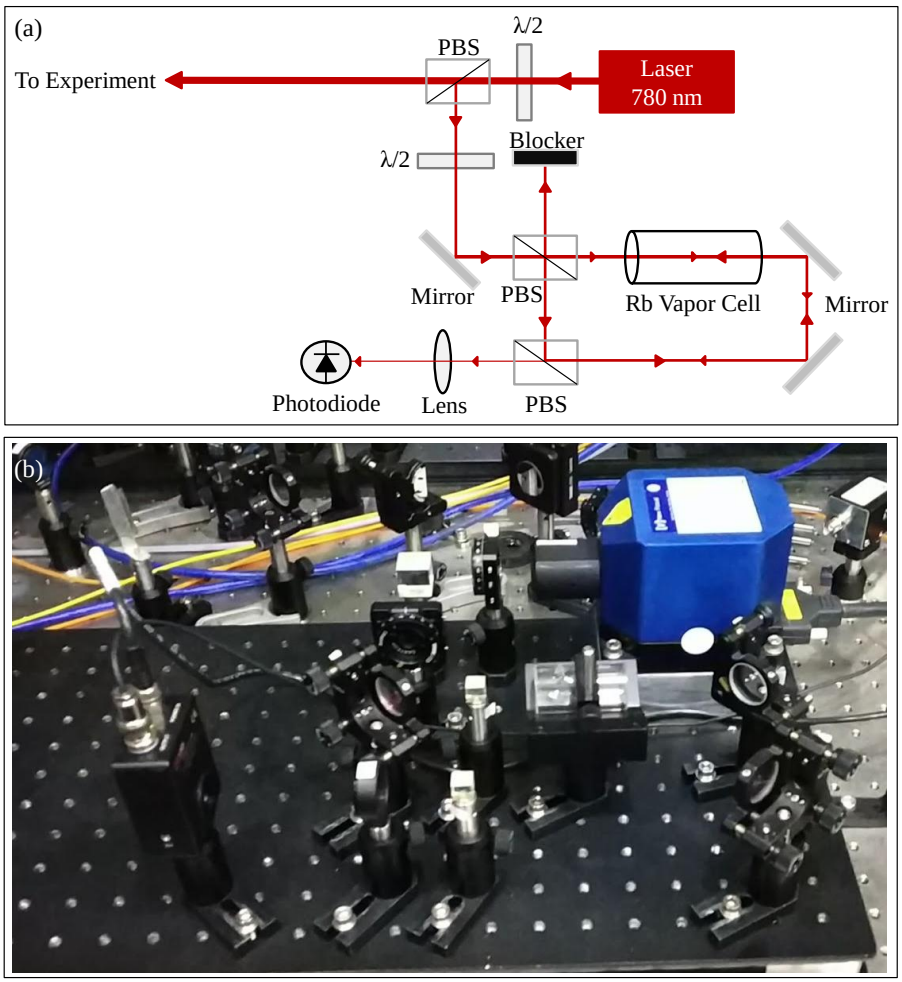

Fig. 4.6: (a)Schematic of optical setup for Rb saturation absorption spectroscopy (b) Optical setup use in experiment to characterize the servo controller

having serial peripheral interface (SPI).

The waveform generator in the servo controller can generate square, sinusoidal and sawtooth waves of frequencies of 0-100 kHz, with 1 Hz resolution and at an amplitude 0-3.3 V with 0.8 mV resolution. The noise density is measured to be $15\,\mathrm{nV}/\sqrt{\mathrm{Hz}}$ @ 10 kHz and harmonic distortion is 10 dB lower than the original signal strength. There is also another slow and precise DAC present in servo system which generates frequencies of upto 10 kHz with peak-to-peak amplitude of 5 V and a resolution of 0.1 mV. The slow and fast functioning frequency generators are used for scanning laser piezo to search resonance spectra and current driver for measurement of PSD or error signal, respectively.

Characterization of IIR filter is an important part in our servo system, and the quality of

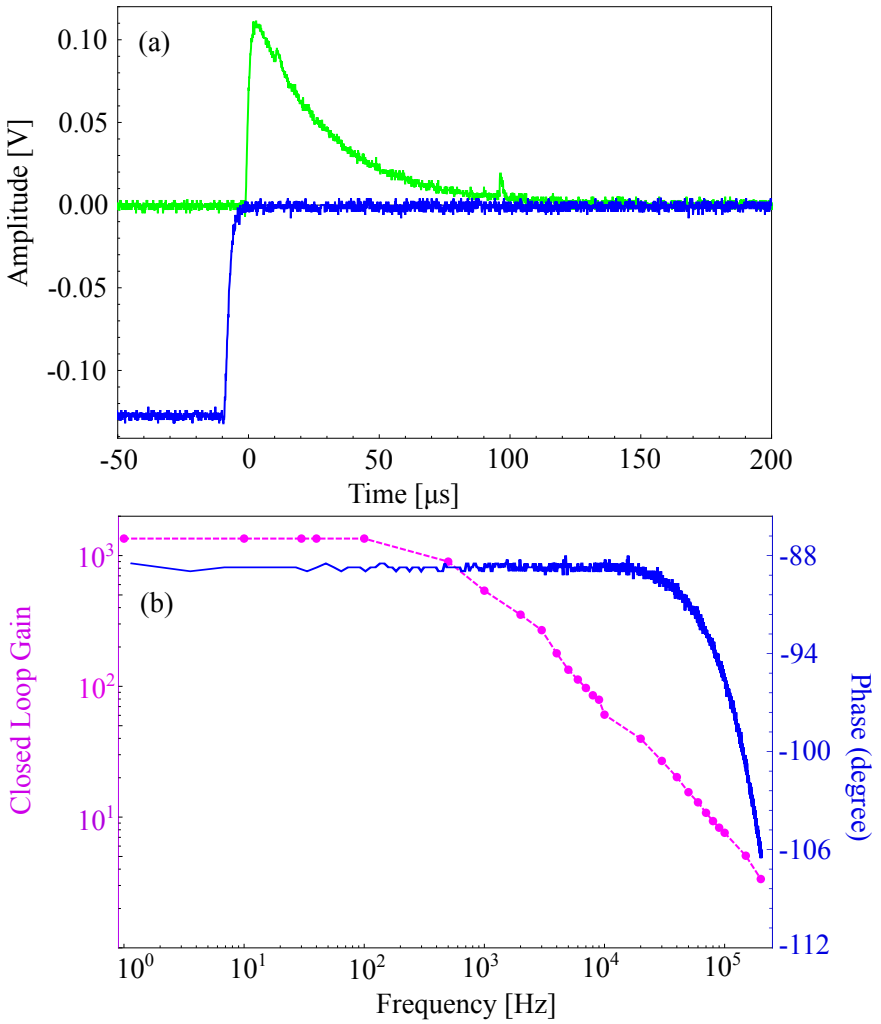

Fig. 4.7: (a) Characteristic response of the type-C PID (green) due to insertion of a square wave (blue) as an external disturbance. (b) PID closed loop gain (magenta) and its corresponding phase change due to insertion of noise (blue).

filter completely depends upon its transfer function which is used to program any filter. The programmed transfer function of IIR type first order filter is given in [105], which shows that the amplitude of any frequency passed through a filter gets changed by an amount $L = 10 \log(1+(\omega)^2)$ called loss. The difference in loss between the fundamental frequency and its second harmonic is given by $\Delta L = 20 \log (2\omega/\omega)$ (if $\omega > 1$). We use this calculation as a characterization parameter, for example if we use a sinusoidal wave of frequency ω and pass it through a first order low pass filter of cutoff frequency $\omega < \omega_{cutoff} < 2\omega$, then as per the given theoretical formula, $\Delta\ L = 6$ dB. According to our calculation, if we implement the correct higher order transfer function, the losses will be multiples of 6 dB/octave *i.e.* 12 dB/octave and 18 dB/octave for second and third order filter, respectively. These losses give information about the steepness of the bode plot, also called as roll off of the filter. In our module, we

Tab. 4.4: Specification of our FPGA based frequency generator, lock-in amplifier and PID controller

S.No	Parameters	Waveform Generator	Lock-in Amplifier	PID
1.	Damage threshold	± 6 V	± 6 V	± 6 V
2.	Resolution (I/O)	12 bit	12 bit	12 bit
3.	Output	0-3.3 V	0-3.3 V	0-3.3 V
4.	Roll off		6 dB/Octave and 24 dB/Octave	
5.	Phase shift		0 to 360 deg	
6.	Phase resolution		0.02 deg	
7.	Noise @ 10 kHz		$49\,\mathrm{nV}/\sqrt{\mathrm{Hz}}$	
8.	Modulation frequency	DC to 100 kHz	DC to 100 kHz	
9.	Modulation type	Square, Sine, Triangle, Sawtooth	Square and Sine	
10.	Bandwidth			100 kHz with relock mechanism
11.	Signal latency			5.7(1) μs
12.	PI corner frequency			10 kHz
13.	K_P, K_I and K_D gain			upto 60 dB

programmed upto fourth order filter, the Bode plots for first, second, third and fourth order low and high pass filters are shown in Fig. 4.5 (a,b), respectively. The fourth order filter enhances the roll off to 20.16(1) dB/Octave (theoretically 24 dB/Octave) as compared to 5.2(1) dB/Octave (theoretically 6 dB/Octave) in first order filter. The difference between theoretical and experimental value arises as all the coefficients for implementing the filter transfer function are approximated in digital logic as also mentioned in Tab. 4.2.

The detailed performance of the lock-in amplifier is tested in a Rubidium (Rb) Saturation Absorption Spectroscopy (SAS) [106]. In the SAS experiment, we use a 780 nm laser (output power 30 mW) which excites D_2 transition of the Rb atom. The schematic for SAS and the optical setup used for performing the experiment are shown in Fig. 4.6. On passing through a polarizing beam splitter (PBS) and half-waveplate, we get two parts of 29.5 mW and 0.3 mW. For SAS out of the 0.3 mW light, a probe beam of 25 μW and a pump beam of 270 μW are being used, with probe beam being monitored on the oscilloscope via a photodiode amplifier. A 1 Hz triangular wave is fed to the piezo driver as per which the laser frequency gets scanned. The SAS spectra of Rb atom can be detected on the oscilloscope as shown in Fig. 4.8(a). During tuning of laser frequency using piezo driver, we connect a 95 kHz sine wave of amplitude 25 mV to laser current driver for high frequency modulation. When laser is scanned and photodiode gives a voltage variation in form of a spectrum, then using this high frequency modulation and lock-in amplifier, we get the phase sensitive detection of the corresponding spectra. When SAS signal is detected through photodiode and digitized using ADC, it first

Tab. 4.5: Comparison of our module to different commercially available devices

S. No.	Parameters	Our Module	Stanford Research Lock-in SR830	Zurich Instrument HF2LI	Toptica Digilock
1	Input voltage limit	±5	1 V	± 3.3	± 3.5
2	Bandwidth	100 kHz	102 kHz	50 MHz	21 MHz
3	Input voltage sensitivity	1μ V	2 nV	1 nV	
4	Input gain	10^3	10^6	auto gain	digital gain
5	Filter Roll off	24 dB/octave	24 dB/octave	48 dB/octave	12 dB/octave
6	Function generator	Sine, Square, Triangle, sawtooth	Sine	Sine	Sine , triangle, square, sawtooth
7	PID controller	PID bandwidth 100 kHz and auto relocking	NA	PID bandwidth 5 kHz	PID bandwidth 1 MHz and auto relocking
8	Interface	RS232	RS232	RS232	RS232
9	Updates	Easily updates	No	Easily updates	Easily updates
10	Noise	$30nV/\sqrt{Hz}$ @10kHz	$6nV/\sqrt{Hz}$ @1kHz	$5nV/\sqrt{Hz}$ @10kHz	$140nV/\sqrt{Hz}$ @1kHz
11	Application	Universal	Universal	Universal	Only for Toptica laser controller

passes through a band pass filter in lock-in amplifier for smoothening the signal by removing all low frequency terms. This signal is passed through a mixer where it gets multiplied to a reference signal of frequency same as that of the high frequency modulation and then passed through low pass filter of cutoff at 1 kHz. The lock-in amplifier's performance and their noise density while using first and fourth order filters are shown in Fig. 4.5 (c,d). It is clear that the fourth order filter enhances S/N and the noise density is reduced to $30\,\mathrm{nV}/\sqrt{\mathrm{Hz}}$ @10 kHz. The additional peaks at higher frequencies, as visible in the noise spectra shown in Figure 4.5 (d) are characteristic of the DAC, pickup noises by the internal circuit and due to the clock jitter.

In our module, we programmed three different PID controller types, A, B and C, for generating feedback signal for setpoint stabilization. Among these, we are using the C type owing to its ability to avoid overshoot during laser stabilization. For characterizing the programmed PID, a square wave is used as an input disturbance signal and the PID is set such that the output is a DC voltage *i.e.*, the PID produces another square wave of different amplitude and 180^o out of phase. It is observed in Fig. 4.7(a) that the PID flicks out of the lock with a noise

pulse appearance but relocks in due course of time based on the amplitude and frequency of the introduced disturbance. As for example, PID relocks within 135(2)μs for a noise pulse of 131 mV at 1 kHz. The linear response of PID briefs that it fails to relock if the noise is $>$ 1 mV at 1 MHz, which is actually the resolution and speed of the ADC. Therefore, the PID speed is limited by that of the ADC's. The Bode plot of the PID controller in Fig. 4.7(b) shows that the closed loop gain decreases due to ADC, and the phase changes suddenly near 100 kHZ frequency. The detailed specification of the servo controller and its modules are given in Tab. 4.4. Further, in Tab. 4.5 we show some of the essential parameters of our developed system and compare them with few commercially available similar systems. In brief, even though performance wise our system is similar to commercially available systems, it lacks in input voltage sensitivity, which is mostly not so much important other than few specific applications.

4.4. Laser frequency stabilization

Even though the instrument is universal, in our experiment that is developing single ion based optical frequency standard, we plan to use this to stabilize laser frequency with respect to any reference point. The reference point in our experiment is a Doppler free spectrum obtained SAS of Rb atom using 780 nm New Focus vortex TLB6800 ECDL laser which probes its D_2 line. Optical setup for saturation absorption spectroscopy for Rb is shown in Fig. 4.6(a) and the arrangement of optical items in optical breadboard are also shown in Fig. 4.6(b). The laser has a piezo and current driver bandwidth of 1 kHz and 1 MHz, respectively which is used for providing feedback signal to stabilize the laser frequency. In the SAS spectroscopy, the 26 μW probe beam passes through Rb vapour cell in presence of the counterpropagating pump beam of 290 μW and is detected on a fast photodiode. For laser frequency stabilization, a 1 Hz, 500 mV triangular wave and a 96 kHz, 20 mV sinusoidal wave is fed to the laser piezo driver and current driver, respectively from the servo controller. The signal connected to piezo is used to tune the laser frequency and the DC offset to search for the resonance peak of Rb atom. The absorption spectra and the SAS signal with error signal corresponding to each spectra is shown. A suitable peak is chosen as reference point for locking and is scanned, eventually the PID is set ON and the laser frequency is locked at top of the peak of our reference spectra. The error signal which is the output of the lock-in amplifier is first characterised. If the modulation frequency is changed after error signal generation, we observe an increment/decrement occurring in its amplitude due to phase change between reference signal and the modulation signal. Some of the previous works state that low frequency modulation has been used for laser frequency stabilization because it gives maximum slope of error signal *i.e.* larger slope near the zero crossing which results in a tight locking but Eq. 4.5 theoretically states that the slope of error signal and modulation frequency is completely independent of each other. Experimentally, we found that for a certain change of modulation frequency, there is a change in slope

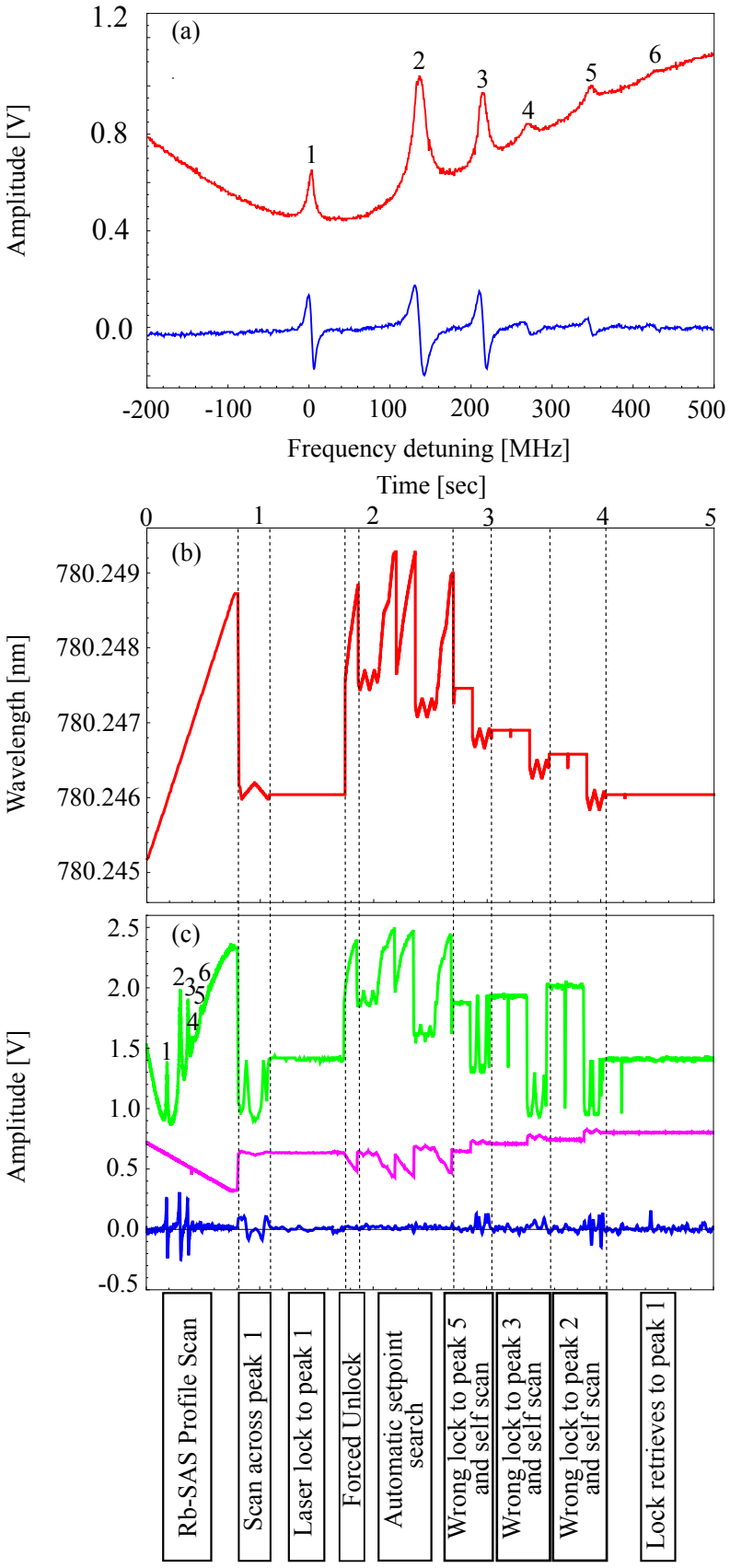

Fig. 4.8: (a) Doppler broadened Rb-Saturation absorption spectrum consisting hyperfine transitions of the D2-line (red) and their lock-in detection (blue). (b) Laser wavelength during lock-unlock-autolock demonstration (red). (c) Demonstration of self finding automatic relocking to a desired setpoint where photodiode voltage (green), laser piezo voltage (magenta) and corresponding error signal (blue) are shown.

of the error signal near zero crossing as calculated and plotted in Fig. 4.9 but just by using a phase shifter, the slope can be corrected and maximized by phase optimization. Therefore, Fig. 4.9 reveals the independency of error signal slope to modulation frequency provided the phase is corrected.

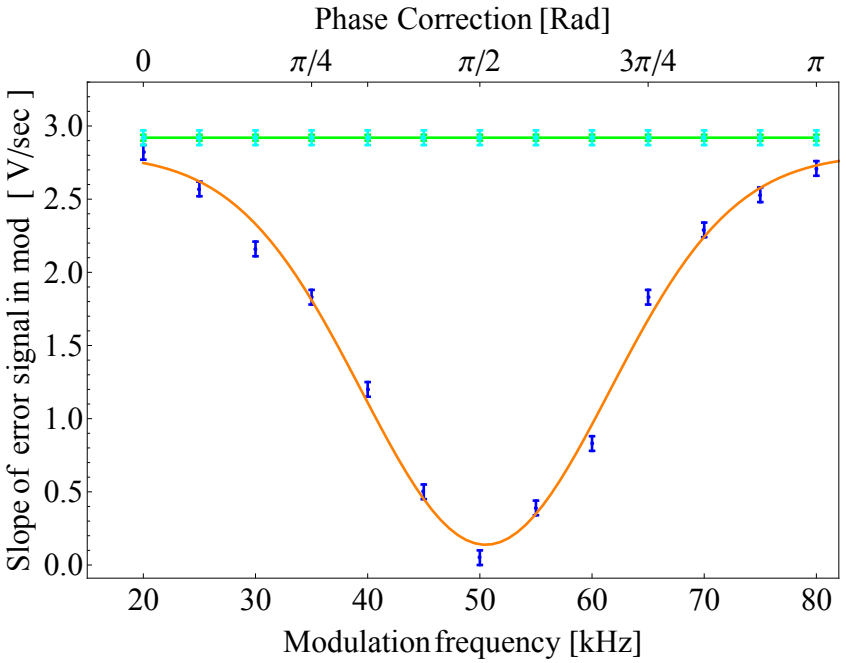

Fig. 4.9: Slope of error signal changes with respect to change in modulation frequency (blue) but is corrected (cyan)using phase shifter. A gaussian function is also fitted to show the variation of slope of error signal with respect to frequency (orange) due to phase change between reference and modulated signal. Theoretically the change of error signal slope is independent of modulation frequency which is fitted in the plot (green).

The modulation frequency gives a way to increase the bandwidth of the PID controller. Increase in the modulation frequency increases the cutoff frequency of low pass filters thus increasing the bandwidth of PID controller. The bandwidth of the PID controller in laser frequency stabilization is nearly equal to cutoff frequency of low pass filter used in lock-in amplifier's output to generate error signal. As we increase the bandwidth of the PID we increase the locking time for the module but decrease the tightness of the lock point. The error signal which is used for locking becomes more noisy which is clearly observable in noise spectra of error signal. When an error signal is generated at a given modulation frequency, then we ON the PID controller and observe the noise fluctuation of error signal and tune the gain coefficient of the submodule in PID controller to minimize these fluctuations and make system stable. For further minimizing the error signal and photodiode voltage fluctuation we use a second AC coupled fast

PID controller which gives feedback to current driver to prevent fast pickup noise to the laser and avoid unlocking from its initial state. When laser is locked and error signal fluctuation is minimized, we take the data of power spectral density for error signal and photodiode signal at a cutoff frequency of 10 kHZ for generating error signal as shown in Fig. 4.10. By analysing the error signal using rectangular noise density approximation, we find that the linewidth of the laser is 0.5(1) MHz.

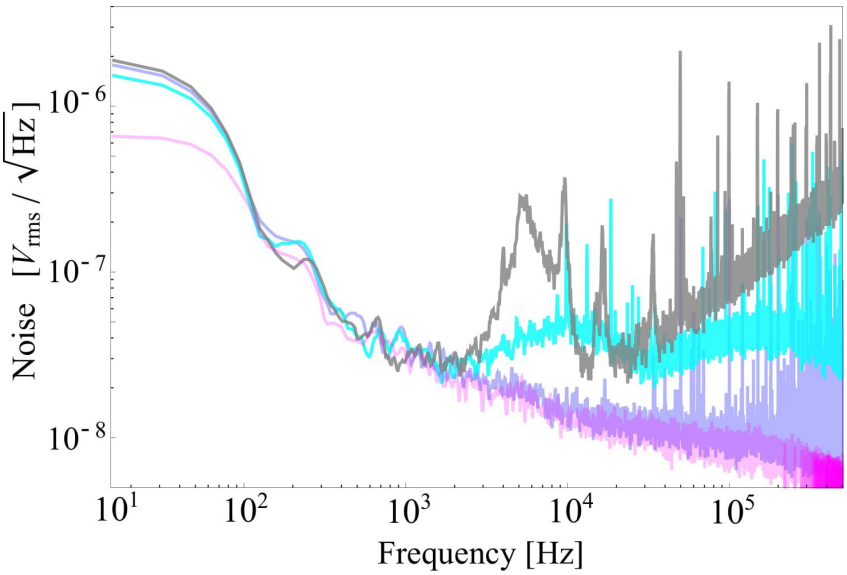

Fig. 4.10: Noise Spectral Densities of input signal (grey) and Lock-in amplifier's output (cyan), DAC output (blue) and spectrum analyser's noise floor (magenta).

Once the laser is tightly locked, the next measurement is for the durability of the lock state. The durability of lock state is completely dependent upon the environmental conditions. If laser frequency gets drifted such that the voltage required for stabilizing it back to the setpoint is beyond its limit, then it gets unlocked or may be locked to another peak. At such instances, a smart relock module is required which relocks the laser back to its initial reference point. In this servo system we developed a simple and fast relocking module, which is activated when laser is locked. In locked condition, the photodiode signal shows a stable DC voltage which is continuously monitored by the relock module, by using the difference between present and past value. If the difference is large, the PID turns OFF and scan gets ON to research for the peak. In every scan process it turns the PID ON to compare the value of photodiode signal to the previous one when laser was initially locked. If this value matches, scanning is stopped. The process of lock and relock is shown in Fig. 4.8(b) and (c) where we show the data of wavelength-meter and oscilloscope during the relock process. In this particular example, to start with, the laser was locked to peak-1 and in due course of time it jumped to lock at peak-4. In this case,

it was externally forced to set the laser unlocked to demonstrate automatic relocking, since otherwise experimentalists will be occupied round the clock and wait for laser to get unlocked. In the successive steps, as described earlier, the instrument itself starts to search for the defined lock point which goes on until the difference between the changed photodiode signal and the reference is null and the laser comes back to the initial lock point.

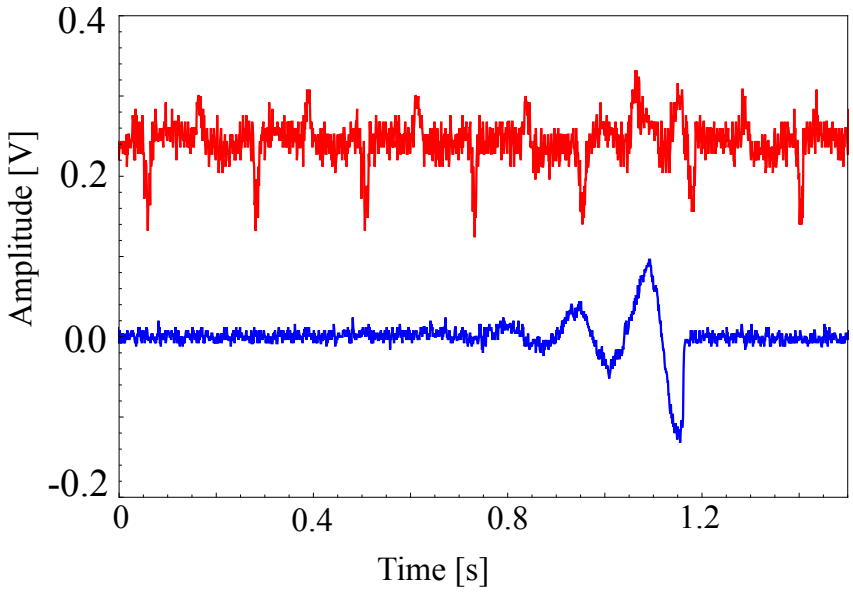

Fig. 4.11: Measured signal showing performance of the instrument in Auger spectroscopy where input (red), output via lock-in detection (blue)

4.5. Auger electron spectroscopy

To prove experimentally that our lock-in amplifier module can detect signals buried deep under noise, we tested this instrument's performance in Auger spectroscopy, where the required signals are in range of few tens of μ V to nV. In this experiment, weak signal of Auger electrons emerging from a silicon substrate Si (III)- 7×7 is detected using the lock-in amplifier. The electron beam of 2 keV and the current at 2 μA with 1 V peak-to-peak multiplier voltage is used. We used 17 kHz square wave with 10 V peak-to-peak to modulate current of the electron gun. The detected voltage corresponding to the Auger current is used as the input to our instrument after the DC offset cancellation and 100 times amplification. The input to the lock-in amplifier and the processed output are shown in Fig. 4.11. The input consists of modulation frequency as well as noise inartistic to the signal coming from the detection system and electron gun [107]. As visible in the Figure 4.11, the desired signal appears with very good S/N through the lock-in detection, which is otherwise not resolvable.

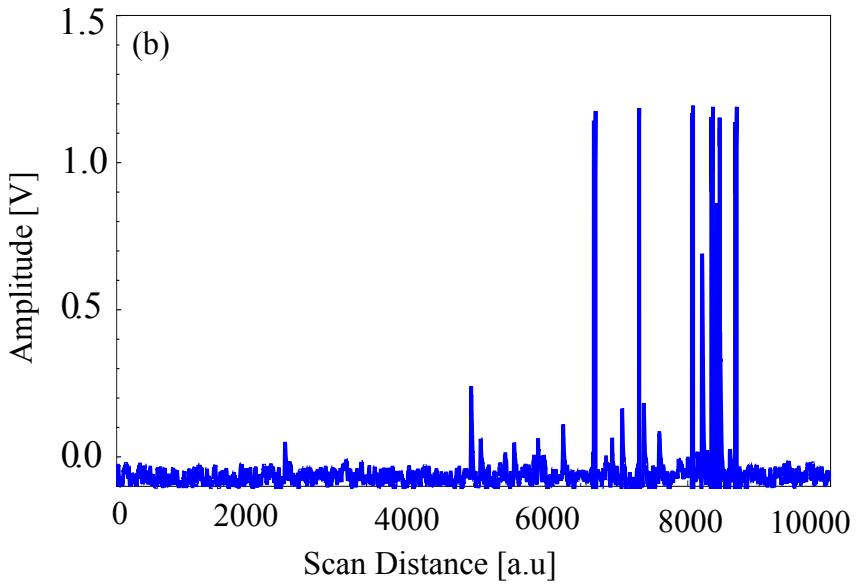

Fig. 4.12: Measured signal showing performance of the instrument in Low coherence optical tomography.

4.6. Low coherence optical tomography

The instrument is used in a low coherence optical tomography setup for surface and sub-surface imaging of materials and biological samples. The detailed protocol of the experiment can be found in Ref. [108]. In this experiment, photons scattered due to impinging of light on the sample surface (solid curved metal used in nuclear reactor) are detected by our servo controller. The speed of scanning the surface of the sample creates a modulation in the output signal which is amplified using an analog amplifier which provides variable gain from 1-1000. Due to this amplification, ADC used in our servo controller is able to detect weak signals upto > 50 μV. This signal is multiplied with the reference signal whose frequency is theoretically calculated using speed of the scanning system. The demodulated signal obtained by the lock-in amplifier of our module, as shown in Fig. 4.12 is used for imaging the surface of the sample. The process of reconstruction of the surface image is described in Ref. [108].

4.7. Conclusion

In this chapter, we describe the design, performance, characterization and universality of the FPGA based servo controller. In this servo controller, we have programmed function generator, lock-in amplifier and PID controller with its unique feature of self finding of a defined setpoint and auto relocking. The digital implementation and software processing not only makes the instrument compact and cost effective but opens up possibility to customize by reconfiguring it for some specific application. A Python based graphical user interface is developed for

controlling of the instrument from a remote PC and monitoring it almost in real time. The waveform generator is capable to generate sawtooth, square, triangle and sinusoidal waves upto 100 kHz, which does not drift with environmental parameters and is free from harmonics due to digital implementation of the modules. This system incorporates low and high pass digital filters having 24 dB/octave roll-off that brings down the lock-in amplifier's noise density to $49\,\mathrm{nV}/\sqrt{\mathrm{Hz}}$ @ 100 kHz. This instrument is designed in such a way that it gives freedom to connect any of the modules to the other without getting any conversion delay or noise introduction. Selection of the devices can be done from the GUI itself without reconfiguring the firmware. Performance of the instrument is demonstrated for laser frequency stabilization, where we use the function generator and lock-in amplifier for generating the error signal and the PID controller to lock the laser frequency. The instrument is capable of resolving $> 1\%$ Rb saturation absorption signal relative to the doppler broadened spectrum, which was used as the frequency reference. Further, to check universality of the instrument, we used it in Auger spectroscopy and low coherence optical tomography experiments, as well.

Chapter 5

Frequency Stabilization of Multiple Laser Wavelengths to a Common Atomic Reference via Transfer Cavity Locking

Publication: A. Roy, L. Sharma, S. Panja and S. De, Multiple laser frequency using a single actively stabilized Fabry-Perot cavity, manuscript is under preparation (2019).

5.1. Introduction

The atom-photon (laser) interaction is a versatile way to perform experiments, such as, precision spectroscopy, laser cooling and trapping, production of degenerate gases, quantum optics, quantum enhanced technology, preparing qubits and interconnecting them and so on. Reproducibility of the measurand that are obtained through any of these experiments rely strongly on the lasers frequency and its stability together with other associated parameters. Therefore, continuous efforts have been made not only to improve quality for the laser frequency stabilization but also to achieve longer-term stability. Depending on the stringent requirement, various methods starting from very complex to rather simple techniques have been tried. Few experiments need ultimate frequency stability [111], e.g., 10^{-19} per s [112], where as few 10 MHz - GHz per day stability serves for most of the cases. Thus, for the laser applications, a simple system that is easy to operate and maintain is more desired. Commonly used techniques are, Saturation Absorption Spectroscopy (SAS) of an atomic or molecular transition and referencing the laser frequency with respect to that [113]. Pound-Drever-Hall (PDH) is an another simple technique to frequency stabilize a laser with respect to a stable resonant Fabry-Perot (FP) cavity transmitted spectrum [114]. Using this approach, stability can be further enhanced to a state-of-the-art level by using a ultra-stable FP cavity [115], which consists of a more complex setup. Upon availability of an optical frequency comb, lasers of different wavelengths can be frequency locked with respect to the nearby comb lines, by measuring their beat frequency and servo-ing that to the experimenting laser [116]. In recent times, software based signal process-

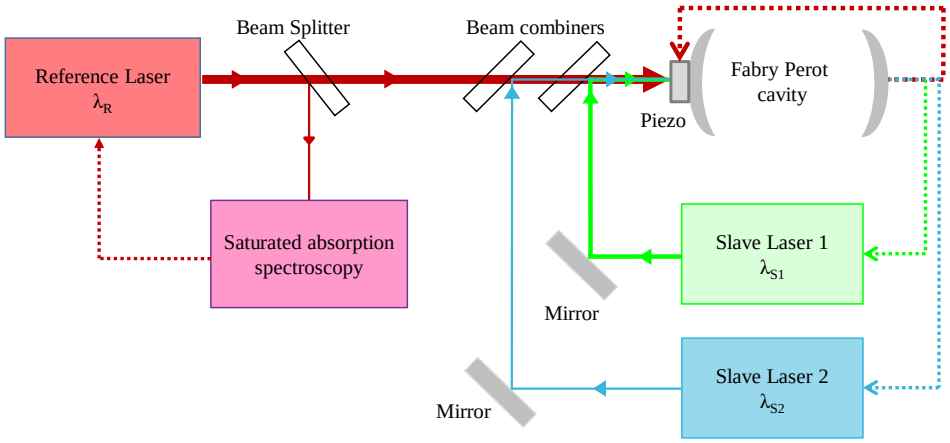

Fig. 5.1: Block diagram of the transfer cavity locking, where λ_R is the reference laser and frequency stabilized by saturation absorption spectroscopy and λ_{Si} (for i = 1,2..) are the slave lasers that are to be frequency stabilized with respect to the stable Fabrt Perot cavity. The setup allows multiplexing so that several wavelength can be stabilized using single reference.

ing to stabilize the laser frequency by using a wavelength-meter is also available now-a-days, which is maintenance free and very user friendly [117]. All of these above mentioned techniques have their Pros & Cons, which are not discussed here as that is not focus of this article.

Many experiments involve multiple lasers at different wavelengths, such as laser cooling of atoms with complex energy level structure, multi photon optical spectroscopy and so on. There, frequency stabilization of the individual lasers are generally achieved by individual techniques, which elaborates the overall setup and extend complexity of the workhorse. As for example, laser cooling of barium [118], radium [119], ytterbium [120], strontium [121], strontium-ion [122], ytterbium-ion [20] and so on involve multiple laser wavelengths. As an example, for ytterbium-ion, transitions at 369.5 nm, 935.2 nm and 638.6 nm/760 nm wavelengths form a closed cycle for laser cooling where as forbidden transitions at 435.5 nm and 467 nm wavelength are used to prepare optical qubit or as the clock transitions. Laser systems at these wavelengths are commercially available. Out of these lasers, Extended Cavity Diode Lasers (ECDLs) at 369.5 nm, 435 nm and 467 nm are typically frequency-doubled systems hence their fundamental wavelengths at 739 nm, 870 nm and 934 nm, respectively, lies within possible anti-reflection coatings of an FP mirrors together with the others. For such applications, frequency stabilization of all lasers to a common reference will simplify nitty-gritty of the system by manifold. Keeping that in mind, in this article, we show a proof of concept of possible multiple laser frequency locking with respect to D2 transition of radium atom using the transfer cavity locking technique [123]. In this setup, we further demonstrate co-scanning of the laser(s) frequency just by tuning the reference lasers frequency and fine tuning of the individual lasers frequency

by tuning their reference point. These simple techniques allow to shift detuning of the lasers in an experimental sequence that typically follows photoionization, laser cooing, state initialization by optical pumping, state detection and so on. In this chapter we give experimental demonstration of the described technique.

5.2. Theory

In transfer cavity technique, frequency stabilization of a slave laser involves three steps: locking the reference laser with respect to a relevant atomic transition followed by coupling that frequency stabilized laser to a FP cavity and stabilizing the optical distance between the cavity mirrors so that reference laser is perfectly mode matched to it and finally locking the slave laser's frequency that can be mode matched to the locked cavity length. Thus, in this technique, characteristic stabilization of the reference laser is transferred to a slave laser using an intermediate FP cavity, schematic of the transfer cavity locking is shown in Fig. 5.1 . Stability of the slave laser's frequency and noise incorporates characteristics of the reference laser and the FP cavity.

In this locking technique, frequency stabilization of the slave laser depends completely on the stability of the modes formed in the FP cavity. The modes are formed inside the cavity due to the constructive interference of light oscillating inside the cavity. The condition for constructive interference inside the cavity is

$$n\,d\,\cos\theta = m\frac{\lambda}{2}, \tag{5.1}$$

where n is refractive index of the medium, d is separation between the mirrors inside the cavity, θ is angle between incoming light direction to the normal of the mirror, m is integer and λ is wavelength of the light. It is clear from this equation that mode stability depends upon dynamicity of optical distance between cavity mirrors and stability of the alignment of light to the cavity. For both short and long term stability, refractive index within the cavity, geometric separation between the mirrors and overall alignment ought to be stabilized. Depending on their geometry and the type of mirrors used, optical cavities are of five types: plane-parallel cavity formed by using plane mirrors; concentric, confocal, hemispherical and concave-convex type optical cavities made by using different arrangements of concave, convex and plane mirrors. The stability of these cavities are determined using the equation

$$0 < g_1 * g_2 < 1, \tag{5.2}$$

where, g_i = 1 - L/R_i, L is cavity length and R_i is the radius of curvature of the i^{th} mirror used in the cavity [124]. Equation 5.2 shows that the convex-concave type cavity is comparatively more stable and for easier alignment of laser light and cavity, convex-convex type confocal

optical cavities are preferable but use of parabolic mirrors for better alignment purposes is the best choice due to their convergence properties. It is very sensitive to small changes in distance between the mirrors. The frequency modes of the cavity made of parabolic mirror is

$$f_{q,m,n} = \frac{c}{2L}(q + \frac{m+0.5}{\pi} arccos\sqrt{g_{1x}g_{2x}} + \frac{n+0.5}{\pi} arccos\sqrt{g_{1y}g_{2y}}), \tag{5.3}$$

where, c is speed of light, L is length of the cavity, g_{ij} = 1- L/R_{ij} and R_{ij} is radius of curvature of i^{th} mirror in j^{th} direction and q, m, n are integers. The cavity length is a major factor which decides system's stability. The material chosen for building the cavity should therefore have nearly zero ultra low expansion (ULE) coefficient at a particular temperature (T_c) and small variation of it with respect to temperature change in the vicinity of that T_c. Using a servo controller to give a feedback voltage to the piezo crystal of the cavity can also help in stabilizing the cavity length. Refractive index plays its role specifically if the medium is air because temperature, pressure and humidity fluctuations may also lead to frequency instabilities. If the modes formed in the cavity are in the same position, then the fluctuation of the slave laser frequency due to change in environmental conditions is

$$\frac{\delta f_s}{\delta \alpha} = \left[\frac{(\frac{\delta n_r}{\delta \alpha})n_s - (\frac{\delta n_s}{\delta \alpha})n_r}{(n_s)^2}\right]\frac{n_s}{n_r} f_s, \tag{5.4}$$

where, α represents environment parameters, f_s is frequency of slave laser, n_r and n_s are refractive indices of medium with respect to reference and slave laser, respectively. To avoid the frequency instabilities due to refractive index, the cavity should be placed in vacuum or the reference laser wavelength should be chosen as close as possible to that of the slave laser to avoid frequency instabilities due to change in refractive index. In our experiment, we use 780 nm as the reference laser and plan to stabilize 739, 760 and 935 nm as slave lasers for laser cooling of Yb ion following the scheme as shown in Fig. 5.1. Here as a proof of concept we describe frequency stabilization of the 739 nm laser via transfer cavity lock technique. After stabilization of slave laser frequency, an important parameter to be measured is the linewidth of the locked laser which gives the tightness of our locking system. Details of different techniques for measurement of laser linewidth via self heterodyne method, rectangular noise spectrum and arbitrary noise spectrum are given in Ref. [125, 126]. Using these, we can measure the laser linewidth as well as carry out fine-tuning of the PID and lock-in amplifier parameters to frequency uncertainty.

5.3. Experimental requirements

In this experiment, the reference laser at wavelength 780 nm is an ECDL laser (Vortex Plus 6800 TLB -6813, New Focus) with a wavelength tunability from 779 nm to 781 nm. To stabilize

Fig. 5.2: (a) 780 nm reference laser, (b) Slave laser 760 nm/ 935 nm, (c) 739 nm slave laser which generates 369 nm using SHG, (d) Fast photodiode with ethernet connectivity, (e) Toptica FPI 100 FP cavity, (f) Servo controller for cavity, (g) Rb vapour cell, (h) Servo controller for reference laser.

its frequency we perform SAS in a Rb vapour cell and the FP cavity is stabilized with respect to this reference laser. At present, to demonstrate the technique, we use the slave laser (Toptica SHG pro laser) of fundamental wavelength at 739 nm. The transfer cavity used for stabilizing 739 nm is a FP cavity (Model No. FPI 100, Toptica). The cavity has a cutoff frequency of 79 kHz and a Free Spectral Range (FSR) is 1 GHz. For signal detection of modes and SAS spectra, we use our indigenously developed fast photodiodes circuits whereas an in-house developed FPGA based lock-in amplifier and PID controller is used for servo controlling (described in Chapter 4). The instruments and devices used in the experiment are shown in Fig 5.3. Along with that, various standard commercially available optics and opto-mechanical components like PBS, mirrors, polarizers, *etc.* have also been used for setting up the experiment.

5.4. Experimental setup

Figure 5.3 shows the optical setup of the transfer cavity locking. Its first part depicts stabilization of reference laser frequency with respect to the D2 line of Rb by employing SAS. The output laser at wavelength 780.02 nm has 30 mW power in total when laser current is 84 mA and temperature is 27 ^oC. This output beam is passed through approximately a 90:10 beam splitter (BS). The reflected light of 2.7 mW is used in the SAS set-up while the transmitted beam of 27 mW is further splitted into two parts using a combination of half waveplate and a polarising beam splitter (PBS), of which the reflected part of 8 mW is double passed through an Acousto Optical Modulator (AOM) operated at 200 MHz and 1 W RF power. Output from the AOM is then coupled to a single mode polarization maintaining optical fiber and used it as input to the FP cavity. The purpose of AOM here is to generate high frequency modulation use for stabilization of FP cavity and tunability in the 780 nm laser frequency. The setups of SAS and Fabry-Perot cavity are assembled on two separate 600 mm $\times$ 300 mm size optical bread boards for transportability and then breadboards are firmly mounted on the optics table. The intermediate single mode polarization maintaining fiber ensures redundant optical alignment between them. In SAS spectroscopy setup, using a half waveplate, the power of the 2.7 mW reflected light is adjusted to 290 μW and is used as the pump beam. The p-polarized pump beam after single pass through the Rb-vapour cell further passes through a Neutral Density (ND) filter followed by a quarter waveplate and a plane mirror. Then the s-polarized light with reduced power of 26 μW is reflected back to the Rb cell as the probe beam and counterpropagating to the pump beam which is then detected by one of our indigenously developed fast photodetectors made of silicon pin photodiodes. For a closed feedback loop for laser frequency stabilization, the photodiode signal is connected to the FPGA based lock-in and servo controller, the output of which is then sent to the laser controller. The indigenous FPGA based servo controller is described in Chapter 4. The fiber coupled light of 780 nm and power 2.7 mW is sent into the FP cavity through a half waveplate and a PBS.

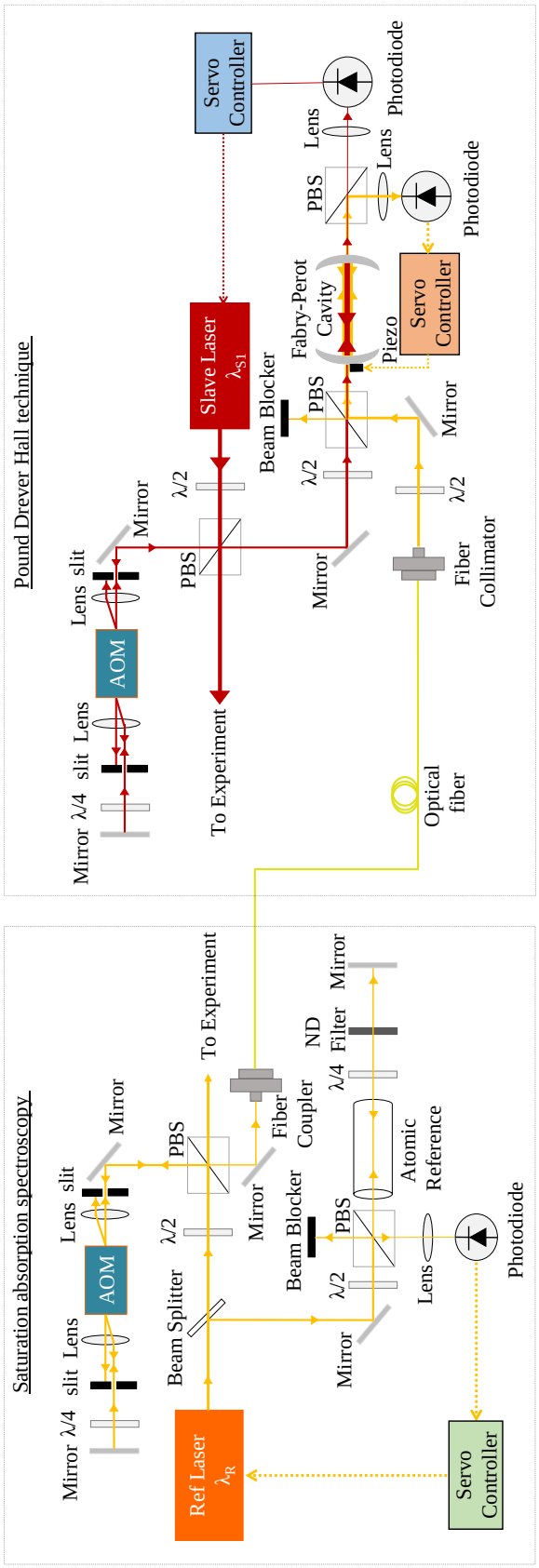

Fig. 5.3: Optical setup for transfer cavity locking consisting of SAS and FP cavity setup

The reflected light coupled to the scanning FP cavity falls on a commercial fast photodiode, the output signal of which is sent to the piezo driver circuit of the FP cavity via the servo controller, thus completing the feedback loop for stabilization of optical distance between the cavity mirrors using pre-stabilized 780 nm laser via SAS. The next part is to couple the slave laser (in this case 739 nm) to the same FP cavity for which its 30 mW laser output is adjusted to 10 mW using a combination of halfwave plate and a PBS. The 10 mW laser beam is passed through an AOM that operates in double pass configuration, which is operated at 200 MHz with 1 W RF power. The first order diffracted light from this AOM is double passed through the quarter waveplate, reflected back to the AOM and then sent through a halfwave plate and PBS to couple it into the FP cavity. In this commercial laser system, current modulation is used for stabilizing the SHG (second harmonic generation) cavity that generates the 369.5 nm light. Due to this reason, we opted to use an additional AOM for fast frequency modulation in laser light without disturbing the main laser system to generate error signal which is used to stabilize the 739 nm laser frequency. Use of an additional AOM also increases the range of tunability. Transmitted light from the FP cavity decouples from the 780 nm reference laser by a PBS and finally falls on a second photodiode. The corresponding electronic signal becomes a part of the feedback loop to stabilize the frequency of the slave laser. Figure 5.3 shows that three servo controllers are required for operating the entire transfer cavity locking technique. An indigenously developed FPGA based device serves for this purpose where all the three servo controllers are modeled onto a single FPGA chip, whose characterization and working principle of each module has been described in Chapter 4.

Figure. 5.4 illustrate the block diagram of the entire FPGA based servo controller that is used for transfer cavity locking experiment. Out of three, each of these servo controllers consist of lock-in amplifier, function generator and PID system. Details of the modules construction and the signal processing within the controller has already been discussed in Chapter 4. In this module we use 1 MSPS speed analog to digital convertor (ADC) and digital to analog convertor (DAC) AD7476A and DAC121S101, respectively. Additionally we use a high voltage low noise amplifier using OPA189, which is able to generate $\pm$15 V with 1 MHz speed for stabilizing FP cavity, because drifting speed of FP cavity is large and have 10 V/ FSR. We have used the Pound Drever Hall type of locking technique which requires a high frequency modulation for generation of the error signal out of the cavity transmission spectra. For generation of error signal out of the SAS spectra, via lock-in detection technique, the laser's current controller is fed with a 89 kHz, 20 mV peak to peak sinusoidal wave, which is also used as reference for the lock-in amplifier. Our FPGA based instrument is capable of generating this frequency internally, hence additional frequency generator is not needed. This makes the entire system cost effective and low noise. Similarly, for stabilization of the cavity, an external frequency modulation is performed by feeding the AOM driver with a 96 kHz, 30 mV peak to peak sinusoidal

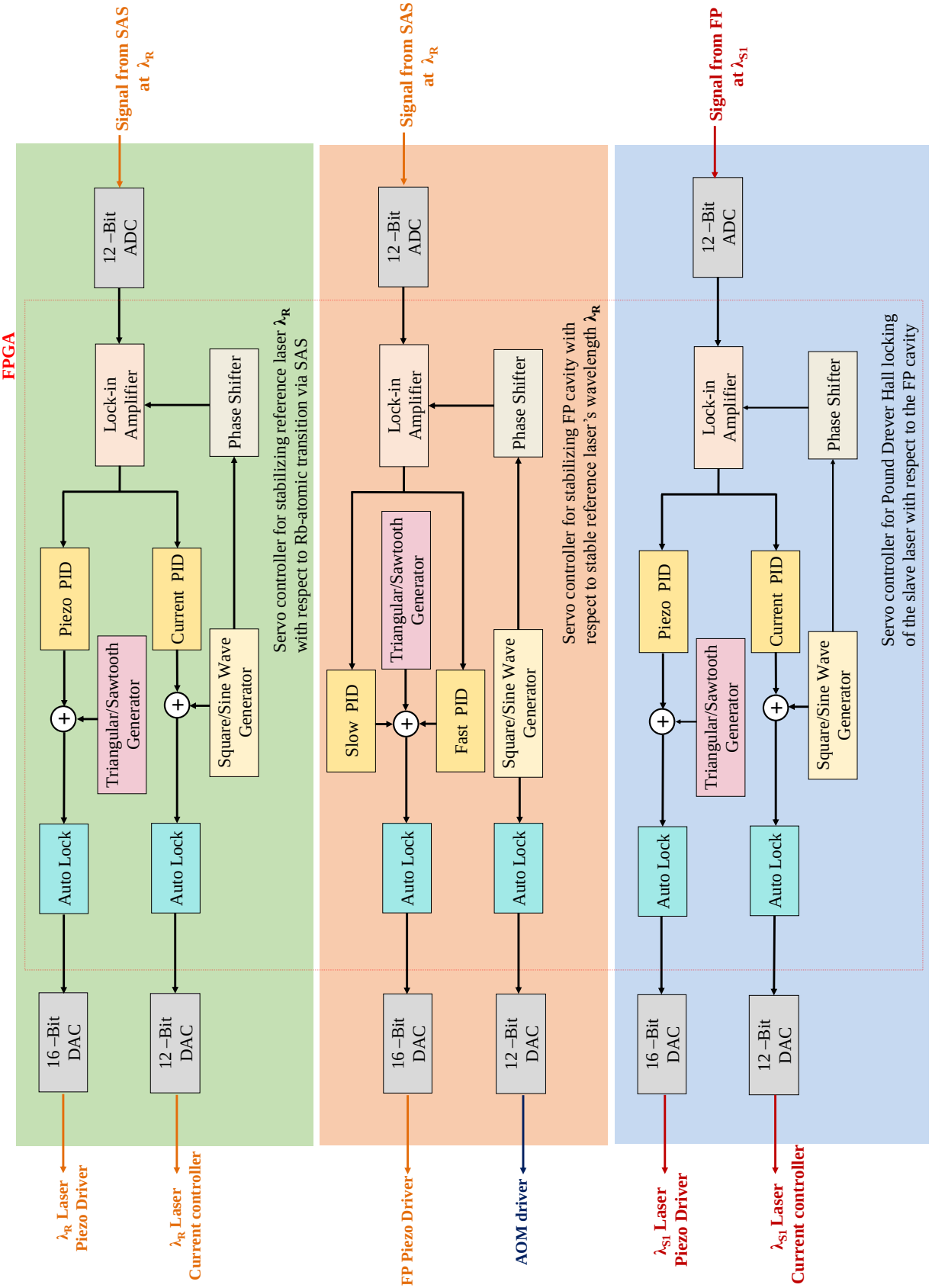

Fig. 5.4: Block diagram of servo controller used for transfer cavity locking technique that is constructed on a single FPGA.

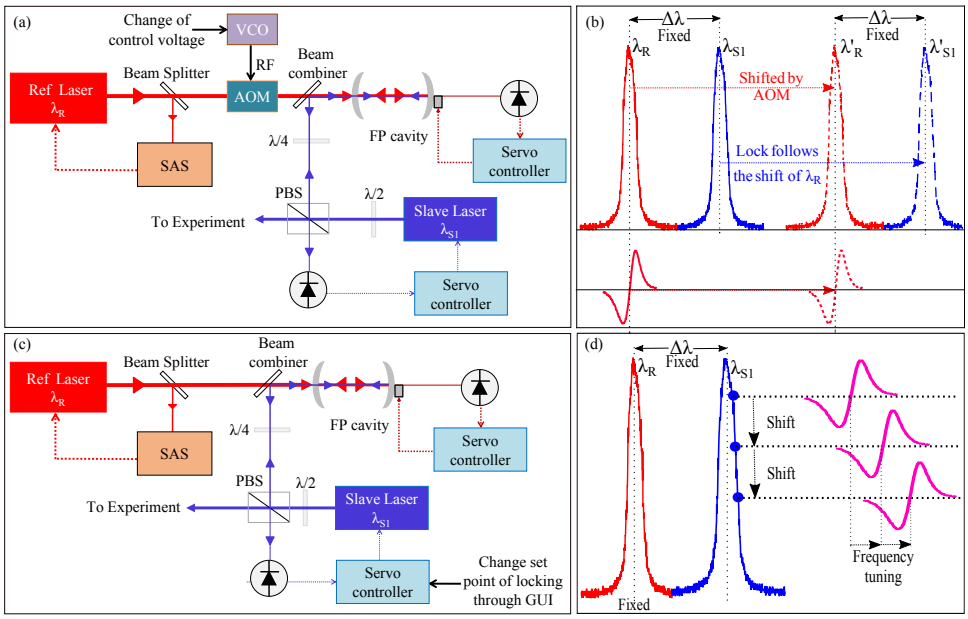

Fig. 5.5: (a) Optical setup of transfer cavity locking and for tuning the length of cavity is done by AOM by changing its RF frequency using change in voltage pin of the VCO. (b) The effect for changing the RF frequency of AOM, there is a shift arise in reference laser (red) transmitted mode which cause shift in slave laser mode (blue) and change in frequency of slave laser in control manner. In this process, the complete error signal shifted but the lock point is remain constant. (c) Optical setup of transfer cavity and for fine tuning the length of the cavity is done by side of the fringe locking technique. In this technique we change the setpoint of servo controller which makes a shift in locked frequency in control manner. (d) The effect during the transmitted modes of reference (red) and slave (blue) laser are shown. In this process reference laser is locked at tip of the peak of transmitted mode and we change the setpoint of transmitted mode of slave laser, which causes change in error signal offset and result a small change in frequency of slave laser without change in reference laser.

wave, which modulates the first order diffracted light. Apart from frequency modulation, use of AOM in this case also gives the advantage of drifting the length of the stabilized cavity by changing its operating RF frequency, thus providing freedom of tunability in our system. In Fig. 5.4, we only show the stabilization of 739 nm laser using transfer cavity locking technique, to demonstrate the proof of concept of the multiple lasers' frequency stabilization with respect to a common atomic reference.

5.5. Results and Discussion

In transfer cavity locking system, frequency stability of the slave laser(s) depends on frequency stabilizations of reference laser, optical length of intermediate FP cavity and the intrinsic stability of the slave laser. The noise associated to the slave laser's output frequency is not only limited by its intrinsic system noise but also by that of the frequency stabilized reference laser and intermediate FP cavity, which propagates all the way and adds up. Digital implementation

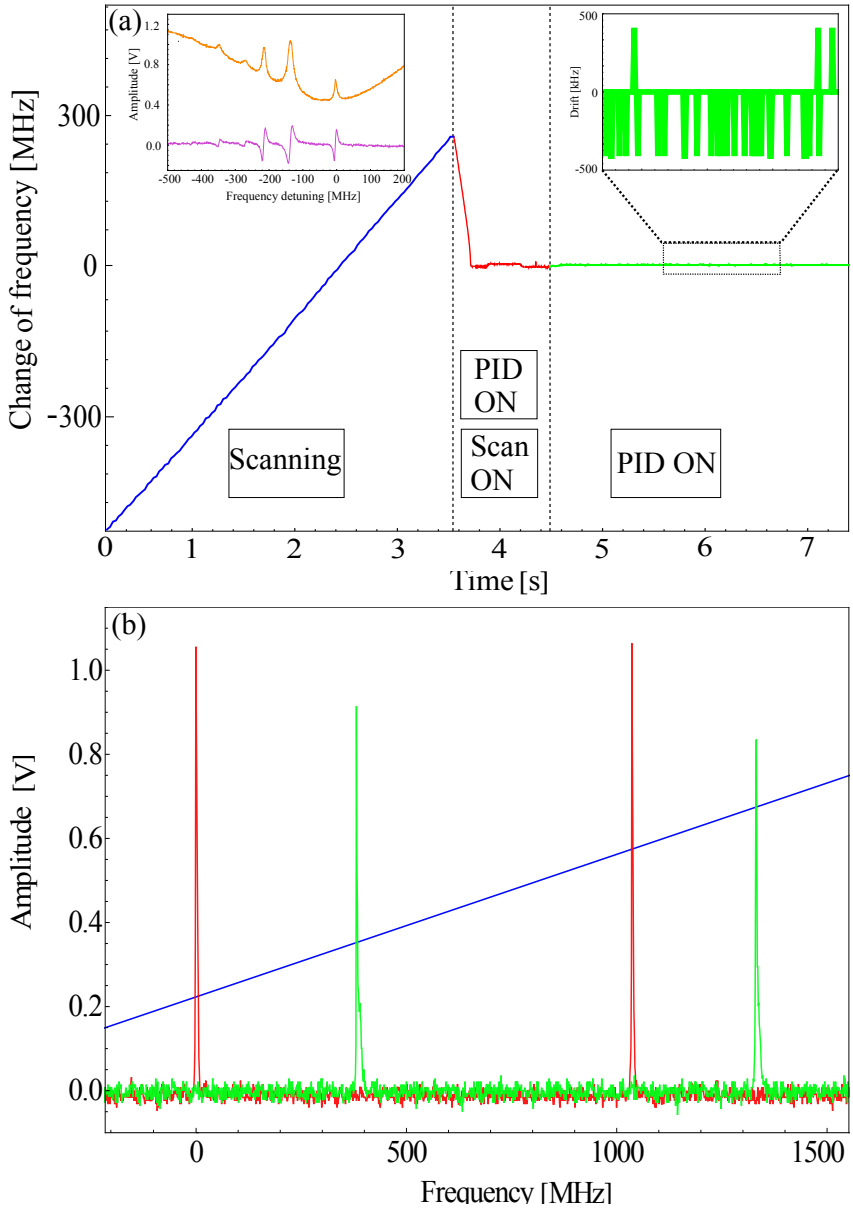

Fig. 5.6: (a) Wavelength meter data shows the steps for laser frequency stabilization of 780 nm laser using Rb SAS. The inset shows Rb SAS profile (orange) and corresponding lock-in detection (magenta) and blue line shows the situation when only SCAN controller is ON in servo controller, red line shows when SCAN and PID both are in ON state and green line shows when only PID is ON and SCAN is OFF. The inset figure shows the fluctuation of data in wavelength meter which estimates frequency stability of the locked laser. (b) Transmission mode profile of the optical cavity when 780 nm laser (red) and 739 nm laser (green) are coupled inside it and a triangular signal is connected to piezo driver (blue) which changes the length of the cavity.

Tab. 5.1: Comparison of parameters measured experimentally for optical cavity used for transfer cavity locking with those provided in the specification sheet.

Wavelength	FSR (GHz)	Finesse	$\triangle\nu_{fringe}$ MHz
805 nm (Spec sheet)	1	400	2
780 nm (λ_M)	0.985(8)	205(23)	4.8(5)
739 nm (λ_S)	1.007(8)	183 (18)	5.5(5)

of the required electronic hardware particularly incorporating all the modules entirely in a single FPGA is therefore done to reduce picking up of the environmental noises. In transfer cavity locking system, there is requirement of tunability in laser frequency for employing frequency modulation. This can be achieved by using optical modulators like AOM and EOM which requires RF source, amplifier and various optics which increase the complexity of the experiment. In our transfer cavity locking technique, we demonstrate use of side of the fringe locking for tuning the laser frequency during stabilization process. In this technique, we are able to tune the laser frequency in a similar fashion as can be done by AOM. Figure 5.5 (a) and (c) shows the optical setups used for tuning the frequency of slave laser in transfer cavity locking when using AOM and side of the fringe locking, respectively and the difference in principle between tunability using AOM shifted lockpoint of the λ_R and side of the fringe is shown in Fig. 5.5 (b) and (d). These figures show the effect on transmitted mode and error signal during the locking process in both cases. In AOM control, change in RF frequency applied to the AO crystal shifts only the absolute wavelength of reference laser; the setpoint of error signal in the transmitted spectrum of FP cavity remains constant, hence the reference lock point gets shifted. Both the reference and slave laser frequencies change in this process keeping their relative frequency difference constant. In side of the fringe locking, frequency tuning of the slave laser is done by varying the setpoints along its transmitted mode locked with respect to the stabilized FP cavity.

The initial process of the transfer cavity locking technique is to stabilize the reference laser (780 nm) with respect to any of the atomic transition of the Rb atom. In Rb Saturation absorption spectroscopy, scanning the laser frequency gives two Doppler broadened absorption dips of ^{85}Rb and ^{87}Rb resulting from its D2 line, among which ^{87}Rb spectra is chosen as its corresponding SAS spectra are clearly resolved with greater separation between each hyperfine spectra compared to that of ^{85}Rb SAS spectra. In ^{87}Rb absorption dip, we get six such dips, three for transition and other three for crossover transitions. Among these, we choose the spec-

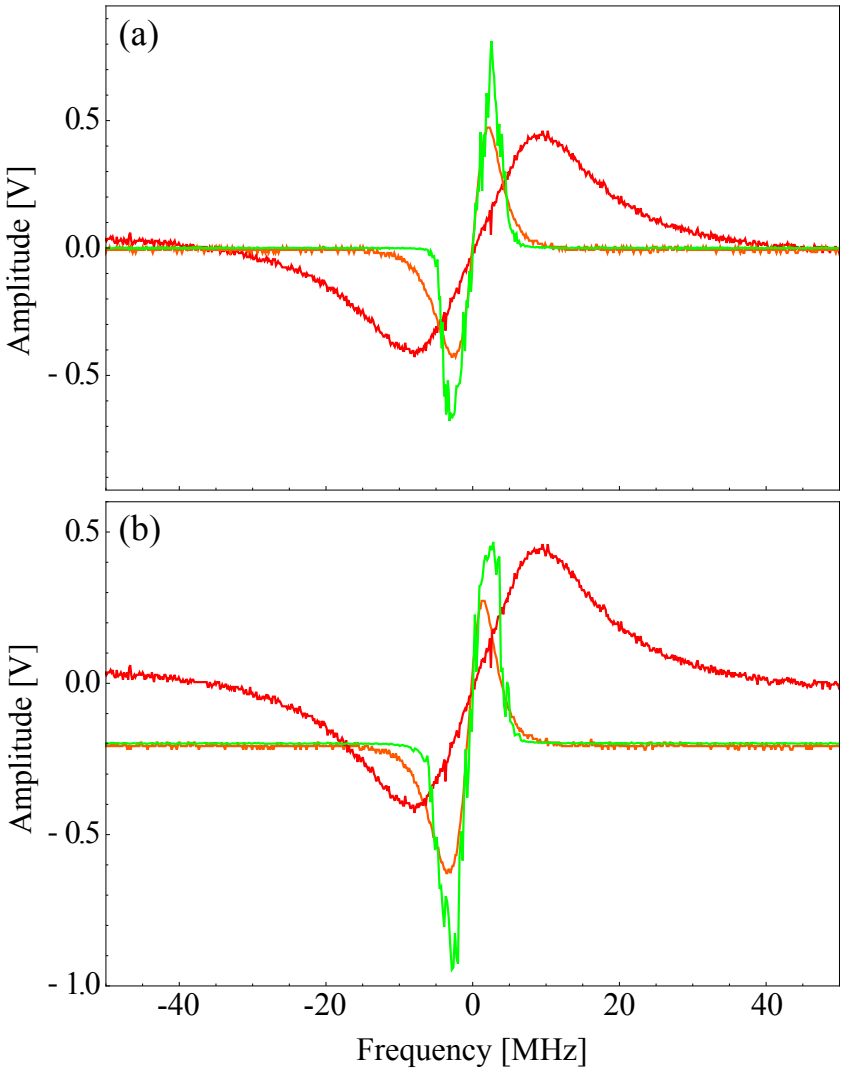

Fig. 5.7: Error signal generation from SAS (red), transmission mode of the cavity for reference laser (orange) and slave laser (green) for (a) top of the fringe and (b) side of the fringe methods.

tra corresponding to the transition F = 2 → F' = 3 hyperfine transition for reference locking. In our setup, we do not use any balanced photodiode or modulation transfer spectroscopy, so the slope or shape of the error signal depends on the position of the Doppler free spectra lying inside the absorption dip. The chosen spectrum lies within the nearly flat region of the absorption dip, so there is negligible effect coming from the slope of the absorption dip. The natural line-width of the chosen SAS spectra is 5 MHz but due to power broadening of the pump beam light power and pressure broadening resulting from environmental fluctuations, obtained FWHM of this spectra is 20(1) MHz. Decreasing the power of pump beam in this cannot be a solution as that would further lower the signal to noise ratio. To stabilize laser frequency with respect to this spectra, we first reduce the scan amplitude of the laser, so that

it scans only the single peak of chosen spectra. In this locking process, we want to stabilize laser frequency at top of the fringe which requires generation of an error signal of the chosen spectrum. The error signal is generated by using 89 kHz sine wave with 25 mV to current driver of the laser for fast frequency modulation during slow scanning of piezo driver using 1 Hz, 500 mV triangular signal. The SAS signal now detected on photodiode is passed through the lock-in amplifier to get the error signal as shown in the inset of Fig. 5.6(a). The slope of this error signal is maximized by optimizing the phase difference between reference signal and modulated signal in the lock-in amplifier; this in turn enhances the tightness of the locking point. The PID controller then takes in the error signal and generates a feedback signal which goes to the piezo driver and current controller to further stabilize the frequency at peak of the chosen SAS spectra. The relevant electronics for stabilization of reference laser with respect to Rb SAS is already discussed in detail in Chapter 4 and shown in Fig. 5.4. In Fig. 5.6(a), the process of locking reference laser is demonstrated where 780 nm laser is locked to one of the hyperfine transitions: F = 2 $\rightarrow$ F' = 3 of ^{85}Rb. Once the laser gets locked, the scan signal which is responsible for tuning the laser frequency automatically stops and PID gets active to stabilize laser frequency and prevent it from environmental disturbance. As shown in the inset of Fig. 5.6(a), the frequency fluctuation data is recorded using highfinesse WS-7 wavelength-meter which is calibrated to its internal neon lamp reference. Tuning the parameters of electronics module decreases these fluctuations and increases the locking stability. The stabilized laser frequency with respect to Rb atom hyperfine transition is then used as reference frequency and the laser is called reference laser in our transfer cavity locking system.

In our transfer cavity system we use 780 nm laser as reference laser and 739 nm as slave laser, where our aim is to stabilize 739 nm laser with respect to 780 nm laser. In this process we first couple the reference and slave laser to a common FP cavity and detect their transmitted modes during scanning of the FP cavity length using 20 V and 1 Hz triangular wave. The optical setup for detecting transmitted modes is shown in Fig. 5.3. The FP cavity used here for transfer cavity locking technique is made of aluminium and uses a pair of confocal mirrors for generating transmitted/ reflected modes. One of the mirrors is put on an adjustable platform for manual tuning of the cavity length whereas for fine tuning in its length, a piezo crystal is attached to the other mirror. As per the voltage biasing on the piezo crystal, the attached mirror's position can be tuned from a few nm to a few μm. As per the specification sheet, the FP cavity's FSR is approximately 1 GHz @ 805 nm with 8V/FSR and finesse $>$ 400. The transmitted modes generated are plotted in Fig. 5.6(b), which gives the measurement of FSR and finesse of the cavity for these wavelengths. The measurement of these parameters are done by comparing data between wavelength meter and oscilloscope. When laser frequency is scanned, the wavelength meter shows the drift of wavelength and oscilloscope shows the transmitted modes; superposition of these data gives frequency interval after which transmitted modes are

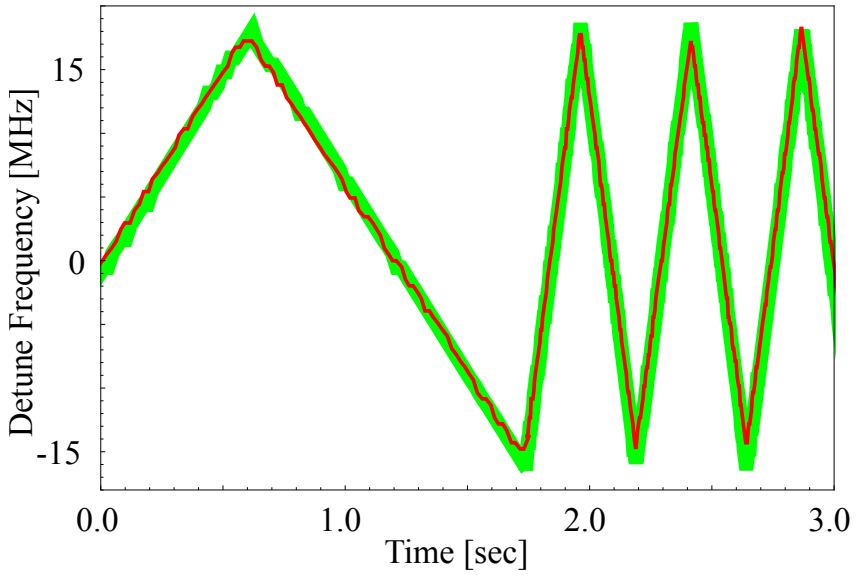

Fig. 5.8: The mode of the slave laser (green) follows that of the reference laser (red) on scanning the reference laser frequency.

generated which gives the FSR of the cavity. The measured FSR of the cavity for 780 nm and 739 nm are 0.985(8) GHz and 1.007(8) GHz, respectively. Using this measurement, we also calculate the FWHM of the transmitted mode to be 4.8(5) MHz and 5.5(5) MHz and the finesse as 205(23) and 183(18) for the reference and slave lasers, respectively. The measured parameters of the FP cavity are tabulated in Tab. 5.1.

When reference laser is locked with respect to D2 line of Rb atom hyperfine transition, it is used to stabilize the optical length of the FP cavity. Peak of the transmitted mode of the reference laser formed in the cavity is used as reference point of locking. Locking the length of cavity requires error signal of the transmitted mode which requires high frequency modulation at the time of slow scanning of the length using piezo driver of the cavity. The high frequency modulation already present in reference laser for generating error signal corresponding to SAS spectrum may be used as an option but the symmetry of the error signal depends on modulation depth. As both the spectra have different FWHM, different modulation depths are required for generation of corresponding error signals. Due to this reason, we use an additional AOM in double pass configuration for frequency modulation of part of the reference laser which couples into the FP cavity. For driving the AOM, frequency modulated 200 MHz RF signal is generated by adding 96 kHz and 50 mV sine wave to the voltage controlled oscillator (VCO) control pin of the AOM driver. When reference light is passed through the AOM, it generates frequency modulated 1st order diffracted signal which is coupled to the cavity. The transmitted mode signal detected on photodiode is passed through the lock-in amplifier to get the error signal.

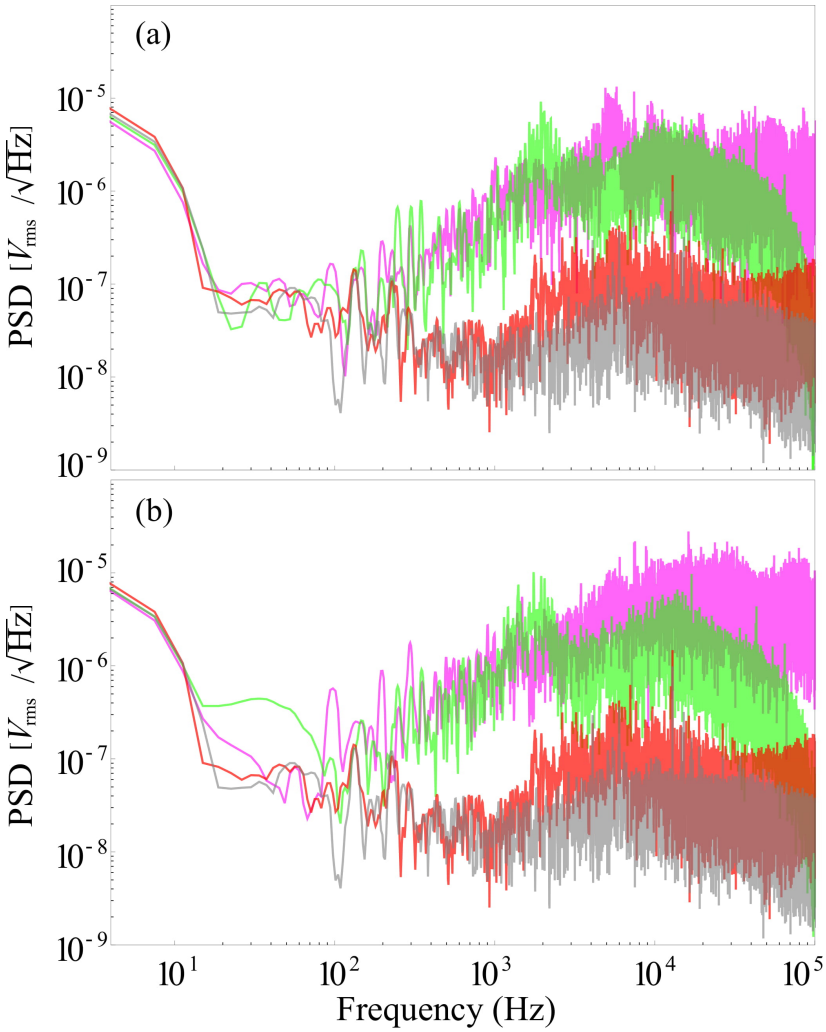

Fig. 5.9: Power spectral density of error signal in locked condition for SAS signal (red), error signals obtained from PDH lock of the FP cavity transmitted spectra for the reference (magenta), slave laser (green) and the DAC intrinsic noise (grey) for (a) top of the fringe and (b) side of the fringe

Generation of error signal for slave laser is also done by using the same technique, the optical setup for using AOM and coupling light frequency to FP cavity is shown in Fig. 5.3. The generated error signals of SAS, transmitted mode of reference and slave lasers are shown in Fig. 5.7(a). It is clear from this figure that the slope of error signal near zero crossing is small for SAS and large for FP cavity, which is equal to 0.018(2) V/MHz for SAS spectra and 0.091(2) V/MHz and 0.101(2) V/MHz for transmitted modes for reference and slave laser, respectively. The slope of the error signal is maximized by optimizing the change in phase difference between the modulated signal detected and the reference frequency inside the lock-in amplifier. The linear region of the error signal is also used for side of the fringe locking which additionally gives a small tunability in our system. For side of the fringe locking, we change the offset of

the error signal which causes change in zero point position of the signal thus causing change in setpoint of the servo controller. The change in offset for the error signal used for side of the fringe locking is shown is Fig. 5.7(b). In this figure, the offset of error signal for SAS has not changed because SAS spectra depends on the MB distribution of atomic gas inside the vapor cell, so the intensity fluctuation of the spectra depends on the surrounding temperature and magnetic field fluctuations around the vapor cell, which makes side of the fringe locking very unstable.

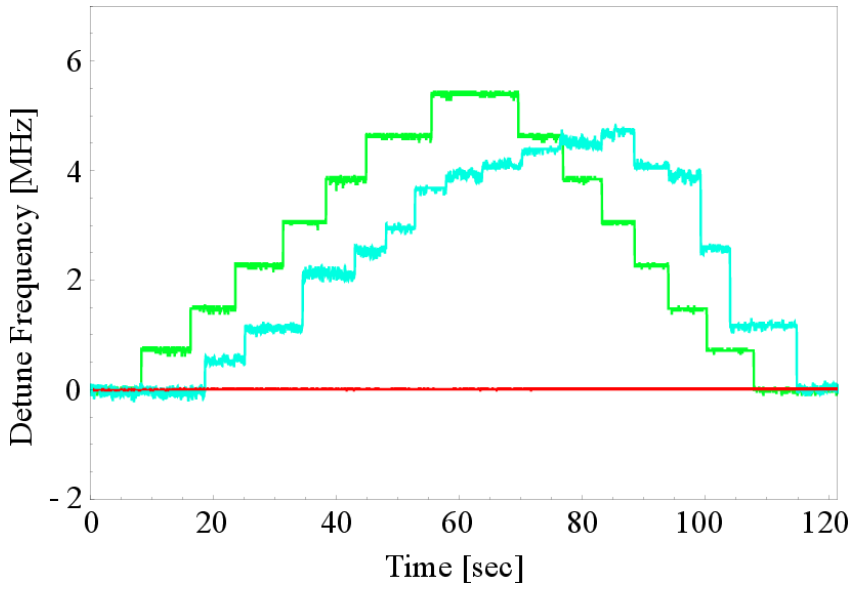

Fig. 5.10: Tunability of slave laser obtained by scanning part of the reference laser frequency that is going to the FP cavity by an AOM (green) and hence tuning the slave laser frequency using side of the fringe locking (cyan) when reference laser is locked at top of the peak of SAS signal (red). By this technique, slave laser's frequency follow scanning od the reference laser's frequency in locked condition.

Error signal generation is necessary for stabilizing the system as its slope and bandwidth of the servo controller decides tightness of the locking. Bandwidth of the servo controller depends upon the cutoff frequency of the low pass filter inside the lock-in amplifier. When the error signals for both master and slave laser are generated, we connect the error signal corresponding to reference laser to PID controller which generates the feedback signal and feeds it to the piezo driver of the FP cavity to lock its optical length. The fluctuations in the transmitted mode signal detected on the photodiode during the stabilized condition of FP cavity, are minimized using fine tuning of PID parameters and gain of error signal. Once the cavity is stabilized with respect to reference laser, the slave laser is scanned using 1 Hz, 200 mV triangular wave to slave laser piezo driver. The offset of the piezo driver voltage is tuned to search for transmitted mode in the locked FP cavity and then the corresponding error signal is generated. The

error signal of slave laser is then sent to the PID for feedback signal generation and locking of the slave laser. When reference laser, FP cavity and slave laser are locked, we scan the reference laser frequency using its AOM and observe that the slave laser follows the reference laser frequency thus confirming the transfer cavity locking technique, as shown in Fig. 5.8. The stability of slave laser decreases with increasing tuning of the reference laser and infact gets locked at higher speed. When all lasers and FP cavity are stabilized, then to measure the stability of the laser frequency and length of the cavity, we take Fast fourier transform (FFT) of the locked error signal. The FFT of the signal is obtained from the Rohde & Schwarz spectrum analyzer (FSV 40), which gives the power spectral density of the noise present in stabilized system as shown in Fig. 5.9(a). Analysis of this figure shows that the least noise density is present in reference laser but when the FP cavity is stabilized with respect to it, the noise power increases. This increase is due to the intrinsic noise of the cavity which comes from temperature fluctuation, vibration and other environmental factors. On locking of slave laser with respect to FP cavity, there is a very small increment in noise power which shows that the intrinsic noise of the slave laser is very small. Using rectangular noise spectrum approximation, we approximate the linewidth of the stabilized reference and slave laser. For this, we integrate the area under the curve of the noise spectra by using numerical analysis and find the V_{rms} of the signal which are 0.0062(2) V and 0.07(3) V for reference and slave laser, respectively. Using the formula for rectangular noise spectrum analysis from the Ref. [126], we calculate the approximated linewidths for the reference and slave lasers to be 0.4(1) MHz and 1.1(1) MHz with an interrogation time of 200 ms.

In transfer cavity locking technique, there is always a finite possibility that the locked slave frequency is not at the desired frequency. Frequency tunability of the system in such cases is therefore a solution. The tunability in controlled manner is done via optical modulators like AOM and EOM. In our optical setup, the AOM used for generating error signal is also used for tuning purpose. The change in RF frequency of AOM gives a frequency offset in reference laser which causes shift in transmitted mode. When the transmitted mode is shifted, the cavity follows the mode and changes its optical length which causes a shift in transmitted mode of the slave laser too. Its corresponding servo controller then follows the shift position of the slave laser mode and tunes its frequency to follow the master laser. Thus, frequency tuning of the slave laser can be done. In our experiment, we also use side of the fringe locking technique for tuning the slave laser frequency. The error signal generated for side of the fringe locking is shown in Fig. 5.7(b). Adding a DC offset to the error signal changes the setpoint of servo controller and so the PID locks the laser frequency at side of the fringe of the transmitted mode. We characterize side of the fringe locking using the power spectral density of noise generated in stabilized error signal as shown in Fig. 5.9(b). The noise analysis shows that the noise power of slave laser during top of the fringe and side of the fringe locking are same and gives same

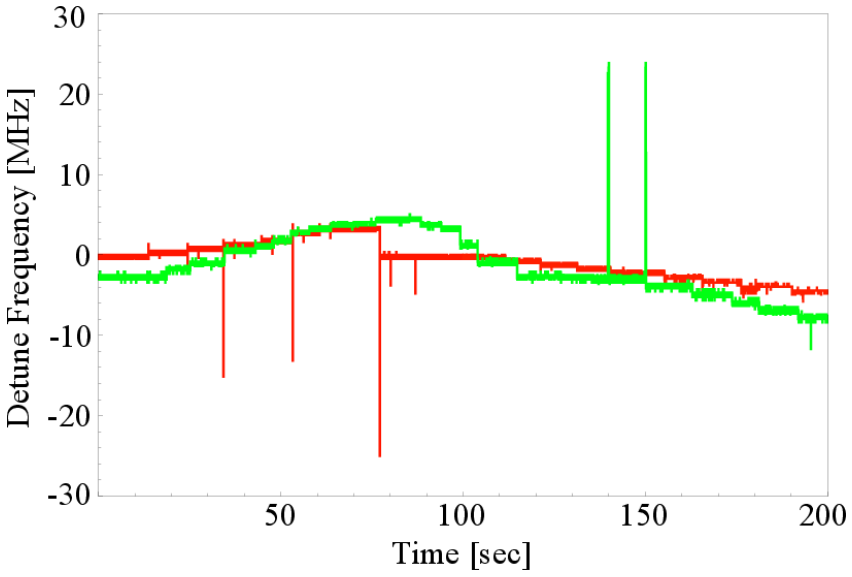

Fig. 5.11: Increase in tunability range of the slave laser (green) by side of the fringe locking of reference laser (red).

value of laser linewidth, this owes to the negligible intensity fluctuation of the diode laser. We also characterize and compare the tunability of our system obtained using AOM to that obtained using side of the fringe locking, which is shown in Fig. 5.10. In this process we lock the reference laser and cavity at top of the fringe and lock the transmitted mode of the slave laser at side of the fringe. During side of the fringe locking, we constantly change the setpoint of the servo controller which changes the slave laser frequency. The change in slave laser frequency is compared for both the cases. We observe that the linearity in tuning with AOM is larger than the side of fringe locking because when we change setpoint of the servo controller, the point drifts from linear region to curve region of the error signal which decreases the linearity range of the locking. To increase the linearity range of the side of the fringe locking, we use cascading technique. During the locked condition of the overall system *i.e.* both reference and slave lasers being locked by side of the fringe technique, cascading their individual tunability range results in increased tunability range of the slave laser. The possibilities of cascading and increasing the tunability range is shown in Fig. 5.11. In this figure, both reference and slave laser transmitted modes are locked at side of the fringe locking technique and the setpoint of the servo controller is changed continuously to drift the slave laser frequency. Such tunability is applied in atomic spectroscopy experiments where simultaneous operation of multiple laser wavelengths demand different detuning of these lasers at different stages, such as atom capturing and laser cooling, magneto optical trapping, state preparation by optical pumping, detection *etc.* These stages follow each other and require detuning of the lasers to be of the order of natural linewidth of the corresponding atomic transitions, which is typically 5-40 MHz for allowed transitions.

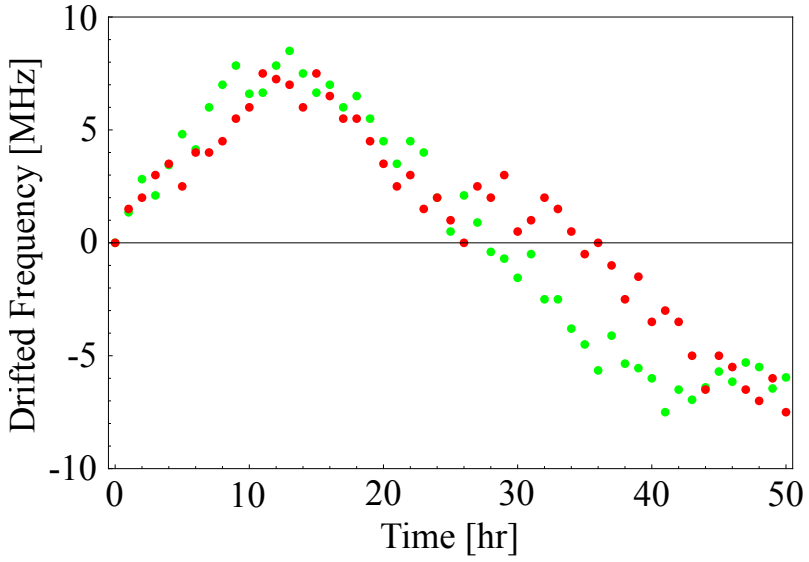

Fig. 5.12: Frequency drift of reference laser (Red) and Slave laser (Green)

Additional systems are thus required to set individual laser frequencies which makes the entire optical setup extensive and there are many free parameters that need to be adjusted during the operation. Here, using our transfer cavity locking setup, we show a way to simplify the system where detuning of a particular slave laser can be changed by shifting reference point of the side of the fringe locking for 5 MHz range or collectively frequency of all lasers an be shifted by tuning lock point of the reference laser, that gives wide range frequency tuning for 50 MHz range. Locking side of the fringe of the reference spectra is done by changing the offset of the error signal generated using Pound Drever Hall technique. The tunability range in this case depends on FWHM of the reference spectra used for locking.

During locking of reference and slave laser, there is always a small time dependent frequency drift observed in the experiment as shown in Fig. 5.12. The drift mainly decreases the long term stability of the locking system. The drifts arises due to change in frequency of locked Rb SAS spectrum and the air current present inside the cavity. The change in Rb SAS spectra frequency mainly depends upon the environmental perturbation on the Rb vapour cell and optical alignment between pump and probe light beam. Also the frequency difference between reference and slave laser is large which causes change in transmitted mode position due to change in refractive index arising from air current. In this figure the drift of slave laser (0.2(5) MHz/hr) follows that of the reference 0.3(5). To decrease the drift in locking system, we have to put the Rb vapour cell and FP cavity inside a vacuum chamber to avoid environmental perturbation. The stability and linewidth of reference and slave laser is tabulated in Tab. 5.2.

Tab. 5.2: Measurement of linewidth of lasers after locking in transfer cavity system

Laser/Spectra	Line width (MHz)	Stability (MHz/hr)
Natural linewidth of ^{87}Rb spectra use for locking reference laser	19(1)	
Natural linewidth of Yb ion cooling transition	18	
After locking linewidth of reference laser 780 nm	0.4(1)	0.2(5)
After locking linewidth of slave laser 739 nm	1.1(1)	0.3(5)
After locking linewidth of 369 nm	2.2(1)	0.6(5)

5.6. Conclusion

Many experiments require stabilized laser frequency for different purposes. Conventionally, for stabilization of laser frequency, it is locked with respect to any atomic spectra in SAS but there are several cases where no atomic transition spectra corresponding to a particular frequency is available in the SAS profile with respect to which the frequency may be locked. In this chapter, we therefore describe the transfer cavity locking technique for stabilizing such frequencies. This technique is one of the low cost alternatives for stabilizing laser frequency with respect to a reference point. In this technique, we use a laser frequency whose atomic SAS spectra is available and lock its frequency with respect to the relevant transition peak of the SAS profile. The locked reference laser frequency is used as a reference frequency and coupled into an FP cavity. The transmitted mode of the reference laser generated outside the cavity is used as a reference spectra which stabilizes the cavity optical length with respect to the mode. When length is stabilized, the slave laser frequency is coupled to the cavity and locked with respect to the its transmitted mode. In this technique, the stability of reference laser is transferred to the slave laser using FP cavity. Using this technique we are able to stabilize multiple lasers using single cavity, which reduces the cost and complexity of the experiment. The electronics which are used to stabilize the laser frequency in this technique are programmed in a single FPGA chip. In this chapter, we show the transfer cavity lock for stabilizing 739 nm laser by using a 780 nm laser which is stabilized by Rb SAS transition peak. We also show that tunability of the system can be achieved both by using side of the fringe locking technique and by tuning

through AOM upto a range of 5 MHz and 25 MHz, respectively. In this technique, we find the short term line width (200 ms) of reference laser is 0.4(1) MHz and slave laser is 1.1(1) MHz with a drift of 0.2(5) and 0.3(5) MHz/hr, respectively.

Chapter 6

Computer Controlled Radio Frequency Drivers for Acousto and Electro Optical Modulators (AOM & EOM)

6.1. Introduction

All laser based experiments, *e.g.*, atomic spectroscopy, laser cooling, magneto-optical trapping, optical lattice, optical tweezers and so on require control of properties of light such as, intensity, frequency, polarization and phase [20]. For that purpose, different types of optical modulators are used that are mostly available commercially [127]. In this chapter, we discuss only about the modulators which are able to modulate frequency of laser light, *i.e.* acousto optic modulator (AOM) [128] and electro optic modulator (EOM) [129]. In these modulators, a radio frequency (RF) is coupled with the optical frequency of the laser light to produce shifted frequencies. In AOM and EOM, the efficiency of modulation or modulation depth depends on its RF frequency and power [128, 129]. In this chapter we describe detailed design of our indigenously developed RF driver to operate AOMs and EOMs. These drivers are computer controlled to automate the entire experiment.

Relevant energy level diagram for laser cooling and probing the clock transition is described in Chapter 1. As shown in Fig. 1.3, we require few hundred MHz to few GHz frequency shifted optical frequencies to drive the hyperfine transitions [20]. For that purpose we use EOMs which have higher reach in RF domain, however in that case, all modulated sidebands at lower and higher frequency relative to the principle are co-propagating [130]. Upon generation of the desired frequencies, they require time tuning between few MHz to few 100 MHz range to identify their desired values. For that purpose, we use AOMs, that diffract the higher and lower order frequencies at different angles. Thus the spatially separated different laser frequencies are easy to isolate [131]. Additionally AOMs are also used for fast switching on-off of the laser lights [132]. Thus we require to operate the AOMs and EOMs in a controlled manner and their driv-

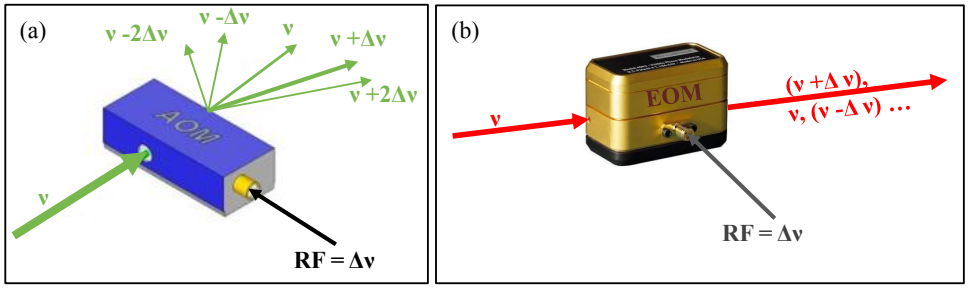

Fig. 6.1: Schematic of frequency modulation using (a) AOM and (b) EOM. In case of AOMs, higher and lower order diffracted patterns are spatially separated, whereas in an EOM they are not diffracted but all are co-propagating [133, 134].

ing parameters are dynamic during different stages of an experiment. To drive the AOMs and EOMs remotely, we have designed and developed in-house the respective RF drivers. These drivers are required to be computer controlled, tunable and low noise because the efficiency of cooling, optical pumping and shelving depends on precise control of laser frequencies and their shot-to-shot redundancy. In this chapter, we discuss about the circuit diagram and working principle of AOM and EOM drivers which are able to generate RF frequency in a very controlled manner. We also characterize our oscillators and filters, which are used for suppressing harmonics and producing stable RF source.

6.2. Theory

When a laser beam is passed through an AOM, the transmitted light gets diffracted. In AOM, there is a crystal which is biased with a RF source by an acceptable range of frequency and power. When light wave transmits into the crystal, it gets reflected from the driving acoustic waves and interfere constructively and form diffracted beam just like Bragg diffraction seen in XRD [131]. In this diffraction process, the light is reflected from a plane which is in motion with respect to lab frame, so the obtained diffracted light is also Doppler shifted and gets frequency modulated due to photon and phonon interaction. The diffracted photons with + & - n^{th} orders of photon's frequency (n = 0, 1, 2 ...) have homogeneous angular dispersion, which depends on frequency of the RF, which is shown in Fig. 6.1(a). Modulation efficiency of AOM is measured by intensity ratio of first and zeroth order of the diffracted beam which is given as [135],

$$\eta = \frac{I_1}{I_0} = \frac{\pi^2}{2\lambda^2}\left(\frac{n^6 p^2}{\rho v^3}\right)\frac{L}{H}P_a, \tag{6.1}$$

where I_1 and I_0 is intensity of the diffracted and incident light respectively. λ, L, H, P_a, n, p, ρ and V are the wavelength of light, length and breadth of Acousto optic (AO) crystal, power

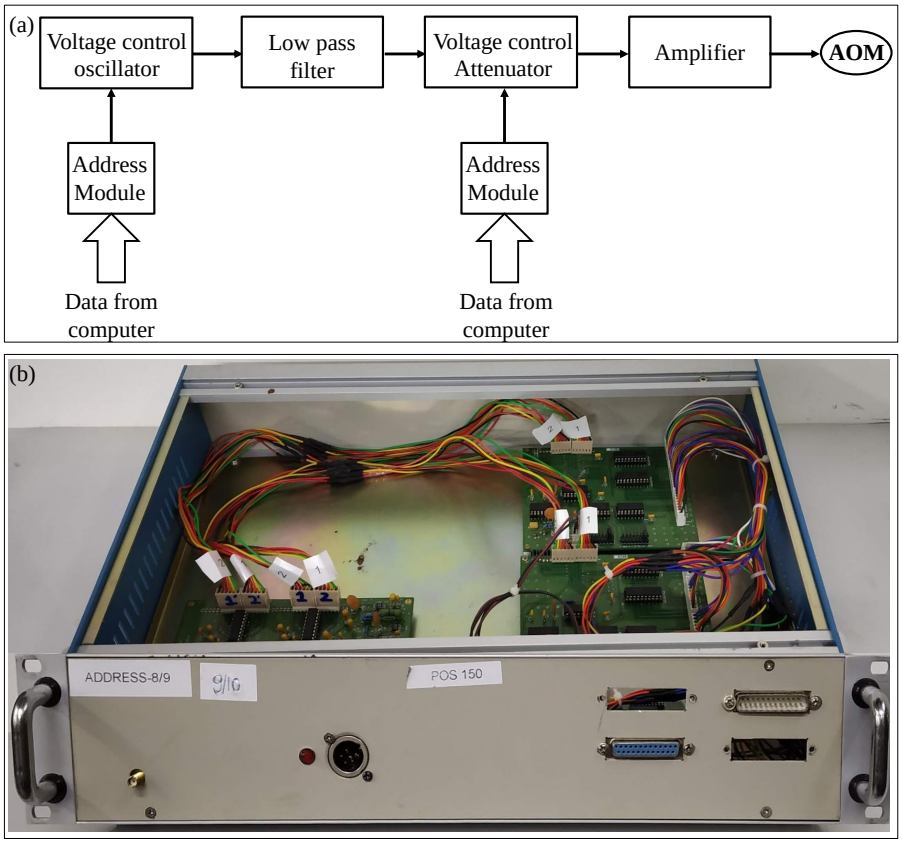

Fig. 6.2: (a) Block diagram of AOM RF driver circuit used to modulate light frequency and intensity. (b) AOM's RF driver module use in experiment

of RF used in AOM, refractive index of crystal, photoelastic coefficient, density of AO crystal and acousto velocity inside the crystal, respectively. The quality factor of AOM is [135]

$$Q = 2\pi \frac{\lambda L f^2}{n V^2}, \tag{6.2}$$

where f is frequency of RF used in modulation. The quality factor describes the efficiency of frequency modulation of the AOM.

In an EOM, when an electromagnetic signal $Ae^{i\Omega t}$, that is a laser light passes through, a time dependent phase term is added in the light and side bands are generated. This is depicted in Fig. 6.1(b). The respective output can be written as [136],

$$Ae^{i\omega t + i\beta \sin(\Omega t)} = A\left(e^{i\omega t} + \frac{\beta}{2} e^{i(\omega+\Omega)t} - \frac{\beta}{2} e^{i(\omega-\Omega)t}\right) \tag{6.3}$$

Here, A and ω are amplitude and frequency of laser light, β and Ω are modulation amplitude and frequency of RF used in EOM, respectively. In EOM, there is a non linear crystal, whose

optic axis changes with respect to the potential across the crystal. The RF source is used to change this potential around crystal periodically. As a result of this, relative rotation depends on the RF.

As brief principle of operation for the AOMs and EOMs as described, their RF drivers play important role. The generation of low noise tunable RF sources is done mainly in two ways, using a Direct digital synthesizer (DDS) [137] and using a voltage controlled oscillator (VCO) [138]. In DDS technique, we use an oscillator whose frequency is fixed and stable, a digital frequency divider and a multiplier to generate different frequencies. In this technique, we can achieve a very stable RF, the amplitude and phase of which can be controlled precisely, but the speed of tuning the frequency is slow due to the frequency divider/multiplier processing delay. In VCO based technique, there is a resonance tank circuit whose resonance frequency is changed by using controlled voltage. The controlled voltage is actually changing the effective time constant of the circuit, which changes the resonance frequency. These type of oscillators where the RF power depends on the RF frequency, are easy to use, provides a high speed of tunability but not a good frequency stability. Among these two techniques, DDS is costlier and more complex than the VCO based oscillators. We use VCO type oscillators as in our experiment, when we require rapid tuning in frequency modulation while the experiment is ongoing. To increase its frequency stability and power, we use phase locked loop (PLL) [139] with DDS and voltage variable RF attenuators (VVA), respectively.

6.3. Circuit Diagram for RF drivers

Circuit designing of RF drivers for optical modulators require VCO, VVA, reference frequency source, filters, amplifiers and automation unit. The range of frequency shifts for AOM is of the order of MHz whereas that of EOM is GHz. Due to this reason, the circuit designing for AOM and EOM RF drivers are different as their principles of operation are different.

Figure 6.2 shows the block diagram of RF driver for AOM which uses VCO, VVA, filters, amplifier and digital to analog (DAC) converters. As shown in the figure, we first generate control pin voltages for VCO and VVA separately using DAC and DACM to generate their desired output. These voltages are generated through a DAC where the digital bits for DAC comes from a digitally operated addressing and control module (DACM)(described in Chapter 3) which is connected with data acquisition (DAQ) card through a digital data bus. The DAQ card is connected to a computer where a LabVIEW based GUI aids in controlling parameters such as, frequency and RF power of the driver. The VCO generates a signal whose frequency depends on the control pin voltage of the VCO. The signal generated by VCO is stable within 0.2 MHz/h, which is good enough for our application, but contains higher order harmonics. To

Tab. 6.1: List of items required for fabricating the RF driver for AOM following the schematic as shown in Fig. 6.3(a)

S.No	Items	Quantity
1.	Mini-circuit VCO POS-300	1
2.	Attenuator Mini-circuit PAS-2+	1
3.	DAC -AD7541	2
4.	RF amplifier MAR3+	2
5.	OPAMP-OPA189	6
6.	Buffer BUF634	6
7.	Buffer MAX4204	1
8.	Decoder 74LS138	4
9.	Quad NAND 7400	2
10.	Monostable 74LS123N	1
11.	Latch 74LS373N	4
12.	LT1763	3
13.	LT1175	2
14.	47 nH air core SMD	10
15.	51 nH air core SMD	10
16.	100 nH air core SMD	10
17.	10 nH air core SMD	10
18.	15 pF ceramic capacitor	10
19.	50 pF ceramic capacitor	10
20.	100 nF ceramic capacitor	50
21.	10 nF ceramic capacitor	50
22.	22 pF ceramic capacitor	10
23.	30 pF ceramic capacitor	10
24.	10 μF polar capacitor	4
25.	10 nF ceramic capacitor	10
26.	1 μF polar capacitor	4
27.	XLR male PCB mount connector	1
28.	DB25 Male Connector	1
29.	DB25 Female Connector	2
30.	1k SMD resistance	16
31.	150k SMD resistance	6
32.	47k SMD resistance	2
33.	10k SMD resistance	8
34.	12k SMD resistance	4
35.	3.2k SMD resistance	4
36.	442k SMD resistance	2
37.	SMA Female PCB mount	1
38.	LED	1
39.	Jumper	4
40.	2U Box	1

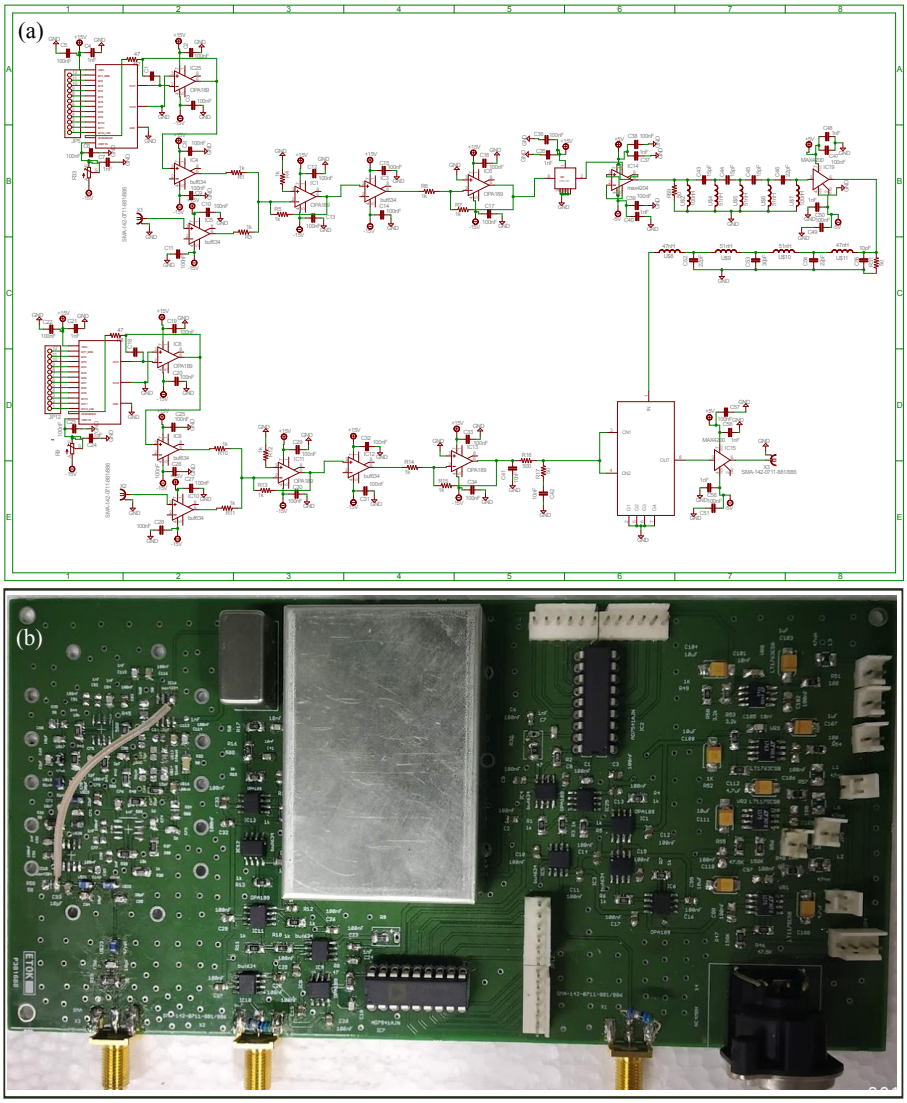

Fig. 6.3: (a) Schematic and (b) populated printed circuit board of an RF driver for driving AOMs.

suppress the harmonics, we use LC type low pass filters and the output of filter is connected to the VVA. The VVA attenuation depends upon the input frequency and its control pin voltage. Thus, using VVA, the RF power of the harmonics generated in the output frequency of the VCO can be controlled and suppressed by 40 dB than the principle frequency. The output signal from VVA is then connected to an [!ht] amplifier and used in AOM modulator for frequency and intensity modulation. The schematic of developed AOM driver is shown in Fig. 6.3(a), where the designed RF source is able to generate 150 MHz to 290 MHz, with RF power variation from -10 dBm to -70 dBm. The step size of the output frequency can be controlled to 0.02 MHz and its output power with a step size of 0.3 dB. In designing of this circuit, we use an adder circuits before the control pins of VCO and VVA, where we add voltage from DAC

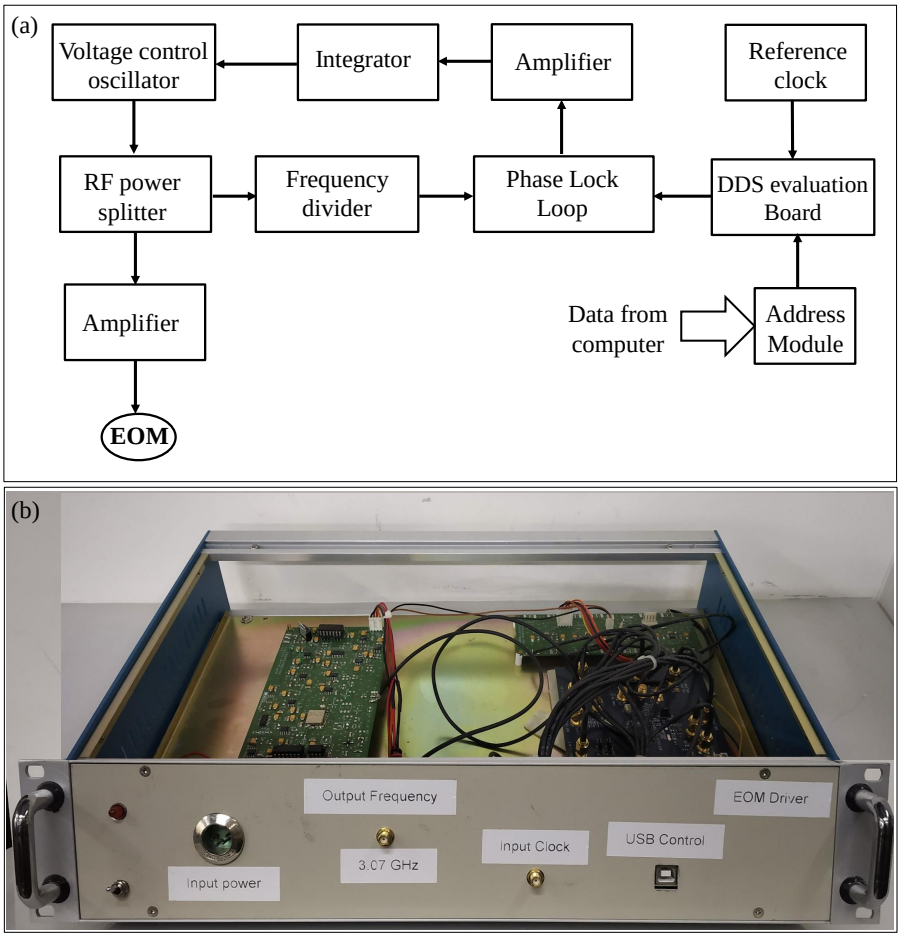

Fig. 6.4: (a) Block diagram of EOM RF driver and (b) the developed hardware mounted in a 19 inch rackmount 2U box

and voltage from external source. The purpose of this adder circuit is to control parameters using external source or to stabilize frequency/power using external servo controller. The use of external source is an optional connection in our RF driver which helps for providing extra stability thus making it a user friendly device. In the board we mounted the VCO and the LC type 4^{th} order filter in a PCB mount grounded case for electromagnetic shielding, which is shown in the Fig. 6.3(b). In PCB design of AOM driver, we take care about the impendence matching and the grounding shielding of the RF signal which suppress high frequency pickup noise and help to improve signal quality. Two address module PCBs for controlling VCO and VVA together with the described AOM driver PCB are mounted on standard 19 inch 2U box.

Circuitry of the EOM driver is more complex than the AOM driver, since stabilization at high frequency is not trivial. The block diagram for the circuit of EOM driver is shown in Fig. 6.4. In this, the RF frequency shift is in a range of few GHz which requires extra care for the

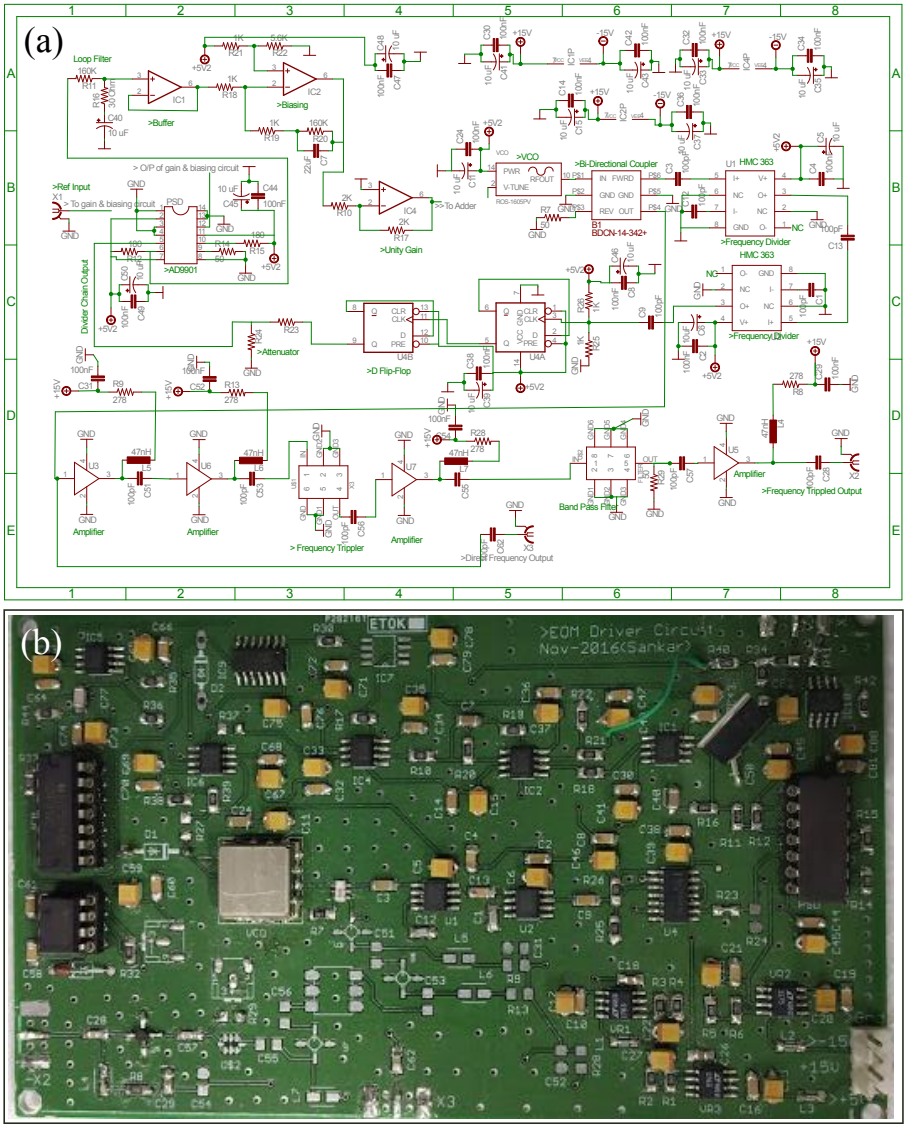

Fig. 6.5: (a) Schematic and (b) populated PCB board for the EOM RF driver

electronics components during the designing of PCB. The circuit for RF driver of EOM has three parts: a DDS board used to generate reference frequency, VCO for generating required frequency and phase locked loop (PLL) to stabilize the VCO output frequency. The PLL compares the reference signal and the output signal from VCO and generates a feedback voltage which is connected to the control pin of the VCO and stabilizes the output frequency of the driver. The schematic and PCB for EOM driver are shown in Fig 6.5(a). The developed hardware is able to generate 1.5 GHz - 3.5 GHz which is tunable with a step size of 10 MHz.

Our DDS circuit is able to generate 20 MHz frequency which is very small compared to the output frequency of VCO, due to this reason we use frequency divider, which divides VCO

Tab. 6.2: List of items required for designing RF driver for driving the EOMs

S.No	Items	Quantity
1.	AD9912A DDS evaluation board	1
2.	Mini-circuit ROS 3800	1
3.	Coupler BDCN-14-342+	2
4.	Frequency divider HMC363	3
5.	Phas/frequency discriminator AD9901	1
6.	Buffer BUF634	2
7.	Buffer MAX4204	3
8.	Opamp MAX4304	2
9.	OP07	6
10.	LT1175	6
11.	LT1763	6
12.	Timer 555	1
13.	Quad NAND 7400	1
14.	47 nH air core SMD	10
15.	51 nH air core SMD	10
16.	100 nH air core SMD	10
17.	10 nH air core SMD	10
18.	15 pF ceramic capacitor	10
19.	50 pF ceramic capacitor	10
20.	100 nF ceramic capacitor	50
21.	10 nF ceramic capacitor	50
22.	22 pF ceramic capacitor	15
23.	30 pF ceramic capacitor	20
24.	10 μF polar capacitor	10
25.	10 nF ceramic capacitor	50
26.	1 μF polar capacitor	10
27.	XLR male PCB mount connector	1
28.	DB25 Male Connector	1
29.	DB25 Female Connector	2
30.	1k SMD resistance	25
31.	150k SMD resistance	8
32.	47k SMD resistance	10
33.	10k SMD resistance	12
34.	12k SMD resistance	8
35.	3.2k SMD resistance	10
36.	442k SMD resistance	8
37.	SMA Female PCB mount	3
38.	LED	1
39.	Jumper	4
40.	2U Box	1
41	Toggle switch	1

output 256 times. Then the output frequency of divider circuit is in range of DDS frequency, which is now easily comparable in PLL and the output of PLL is fed back to the control pin of the VCO. In this process, VCO frequency is locked with respect to the DDS frequency and DDS master clock is locked with respect to a reference clock from an atomic clock source. Once VCO is locked with respect to DDS, RF frequency tuning can be done only by changing DDS output frequency. The VCO follows the DDS and generates output whose frequency is 256 times the frequency of DDS. In designing of PCB for EOM driver, we place all components as close as possible in the PCB, so that no interaction or antennal effect occurs in between IC to IC. As visible in Fig. 6.5(b), some parts are left unpopulated as a future option for implementing auto scan of EOM's VCO during large range of tuning and frequency multipliers which are used in different EOMs requiring high frequency in our trapped Yb ion experiment during laser cooling.

6.4. Result and Discussion

In our experiment, we have used two types of AOMs whose operating ranges are between 150 - 250 MHz and 50 - 100 MHz with central frequency 200 MHz and 80 MHz respectively. In this section, we show results of the RF driver which is able to generate 150 MHz to 250 MHz. We have used Mini Circuit POS-300 as the VCO and for VVA, we use Mini Circuit PAS-2+. The VVA that we used are actually a current control attenuator that works under the principle of current to voltage convertor. Figure 6.6(a) shows tunability of the RF driver with respect to the voltage which is applied to the control pin of the VCO. We control this voltage using a 12 bit DAC whose voltage resolution is 1.0(1) mV and stability is 0.4(1) mV over a period of 24 hour operation. Using this DAC, we are able to tune from 129.16(8) MHz to 265.30(8) MHz with a resolution of 20(8) kHz. The voltage controlling frequency of the VCO is (9.8± 0.1) MHz/V, which is calculated by a linear fit of the data taken in the region between 130 MHz to 160 MHz, as also shown in Fig. 6.6(a). The VCO used in this circuit generates fundamental frequency and additional higher harmonics, which is not desired for the experiment in case we use a high bandwidth modulator. To overcome this problem, we use LC type low pass and high pass filter and by cascading them we create a bandpass filter whose pass range is between 130 MHz to 170 MHz. We also use VVA whose attenuation factor is frequency dependent, and which helps to suppress the harmonics or any high frequency pickup noise. Figure 6.6(b) shows the RF power control using VVA, filters and amplifiers which follow a non-linear profile saturating above certain level of the voltage. In this attenuation control, we plot for three different frequencies 150 MHz, 200 MHz and 250 MHz, so that we are able to find its linear region which is nearly universal for every frequency. In our system, we are able to control 20 dBm RF power with a rate of nearly 7.4(1)dBm/V for a voltage range 4.0(5) to 6.0(5) V with a resolution of 0.3 dBm. We use this linear region to stabilize the RF power using external servo

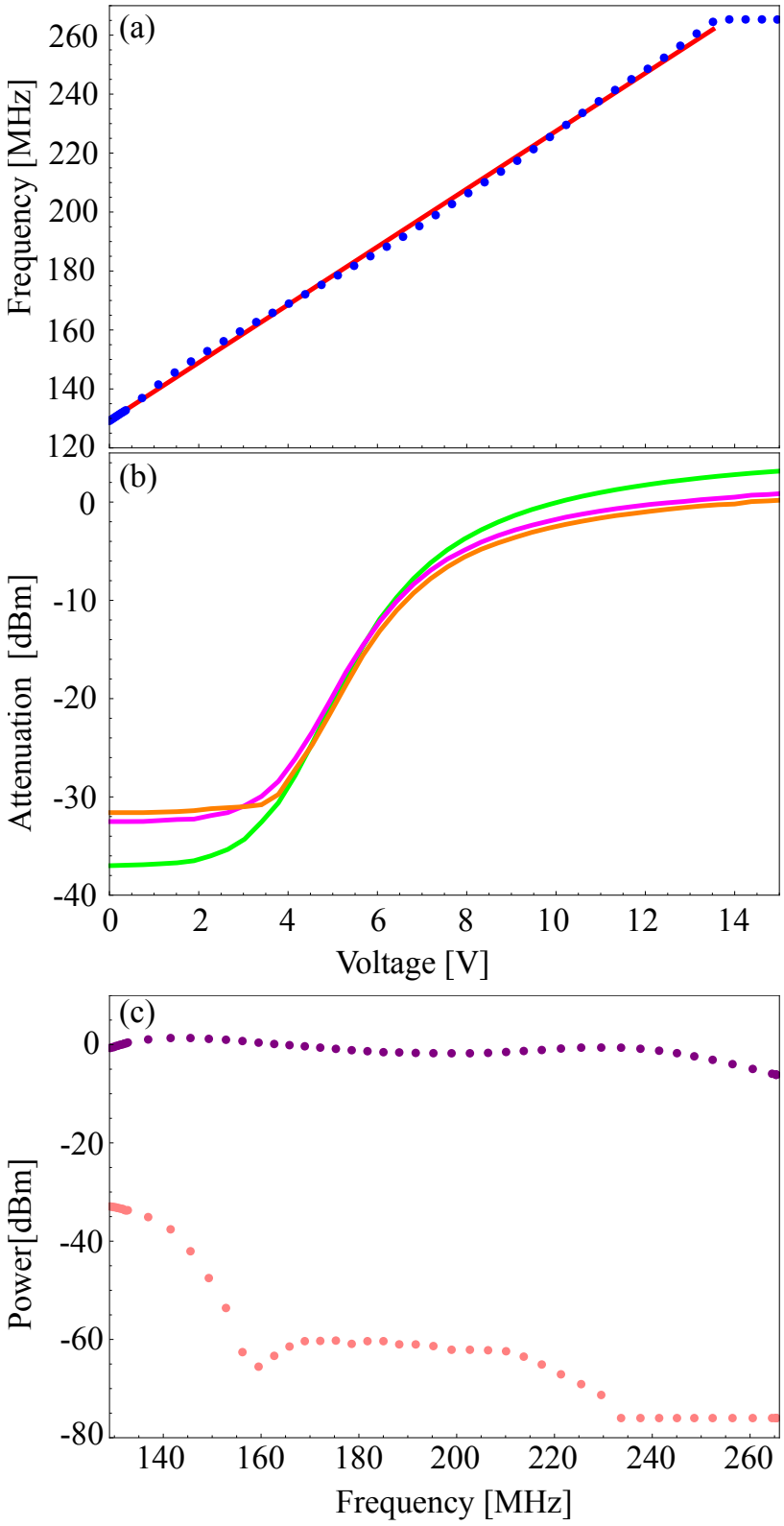

Fig. 6.6: (a) Tuning VCO frequency with respect to the voltage given at the control pin (blue), and a linear fit to it (red). (b) The VVA characterization with respect to the voltage given at control for different input frequencies 150 MHz (green), 200 MHz (magenta) and 250 MHz (orange). (c) Bode plot of the filters used in RF driver, that shows power vs frequency for fundamental signal (purple) and second harmonics (pink)

controller, where we clamp our servo controller in this region for tight locking of RF power or also use for laser intensity stabilization. The filters and VVA also produce a transfer function of the form $1/\omega$, which we obtain through measurement, corresponding plots of which are shown in Fig. 6.6(c). In this plot, we show the attenuation of second order filter which confirms about the filter response and purity of the signal. The RF power in second harmonic is suppressed by 40 dB relative to the fundamental which is due to dual stage 3^{rd} order low pass filter. The power variation of fundamental frequency in pass region of filter is upto 4.2(2) dBm from 150 MHz to 250 MHz due to the LC filter, which creates a bump in transfer function near its cutoff region. We also calculate the phase noise of the RF source which is -94.2 dBc/Hz @ 80kHz when signal amplitude is -17 dBm and frequency is 166.2 MHz. At 200 MHz and at -6.92 dBm, phase noise produced is 130.34 dBc/Hz @12.4 MHz. The phase noise measurement, concludes that our frequency stability is quite good as per our experimental requirement and there is no extra need of servo controller to stabilize the VCO frequency. However, in case we use the RF driver for frequency scanning upto few tens of MHz, then there is a requirement of intensity stabilizer to stabilize the RF power during tuning of frequency.

As per the requirement of experiment, the EOMs generate side bands of the fundamental frequency to drive the transitions between different hyperfine levels of the associated states. In our experiment, we require optical frequencies shifted by 2.1 GHz, 14.7 GHz, 3.07 GHz, 12.6 GHz and 10 GHz for the Yb ion spectroscopy. Since the desired RF frequencies are known, the EOM drivers are designed in a way so that they provide stable frequency and about 400 MHz tunability. Here we characterize our EOM driver which we use for generating 3.07 GHz for repumping lasers at wavelength 935 nm. In designing this driver, we use mini-circuit VCO ROS-3800, which generates 1.7 GHz to 3.9 GHz. In this circuit, we are not using any attenuator because the output intensity of laser does not depend upon the RF power. The magnitude of side bands however depend upon the RF power which we control using power amplifiers used in the EOM drivers. Stabilization of the VCO frequency is done by using a commercial AD9912A DDS board which can generate 10 Hz to 100 MHz and the master clock of this DDS board is locked to an ultrastable reference frequency at 10 MHz, which comes from Cs atomic clock or Rb clock or H-maser or GPS receiver or elsewhere. When we supply a voltage to VCO, the output signal is passed through a bi-directional coupler, where one part moves towards main output and other part passes through a frequency divider. The frequency divider output and DDS output is connected to PLL and the output is fed back to VCO which generates a stabilized frequency. The tuning of VCO frequency is completely dependent upon the tunability of DDS. In Fig. 6.7(a), we show the tunability of VCO with respect to the voltage applied to control pin of the VCO. This VCO has a linear range from 1.8 GHz -3.5 GHz, where we find smooth voltage controlled frequency tuning of (132 $\pm$ 2) MHz/V. The voltage requirement to generate 3.07 GHz is about 9.3 V to VCO's control pin, the PLL used in our circuit is not

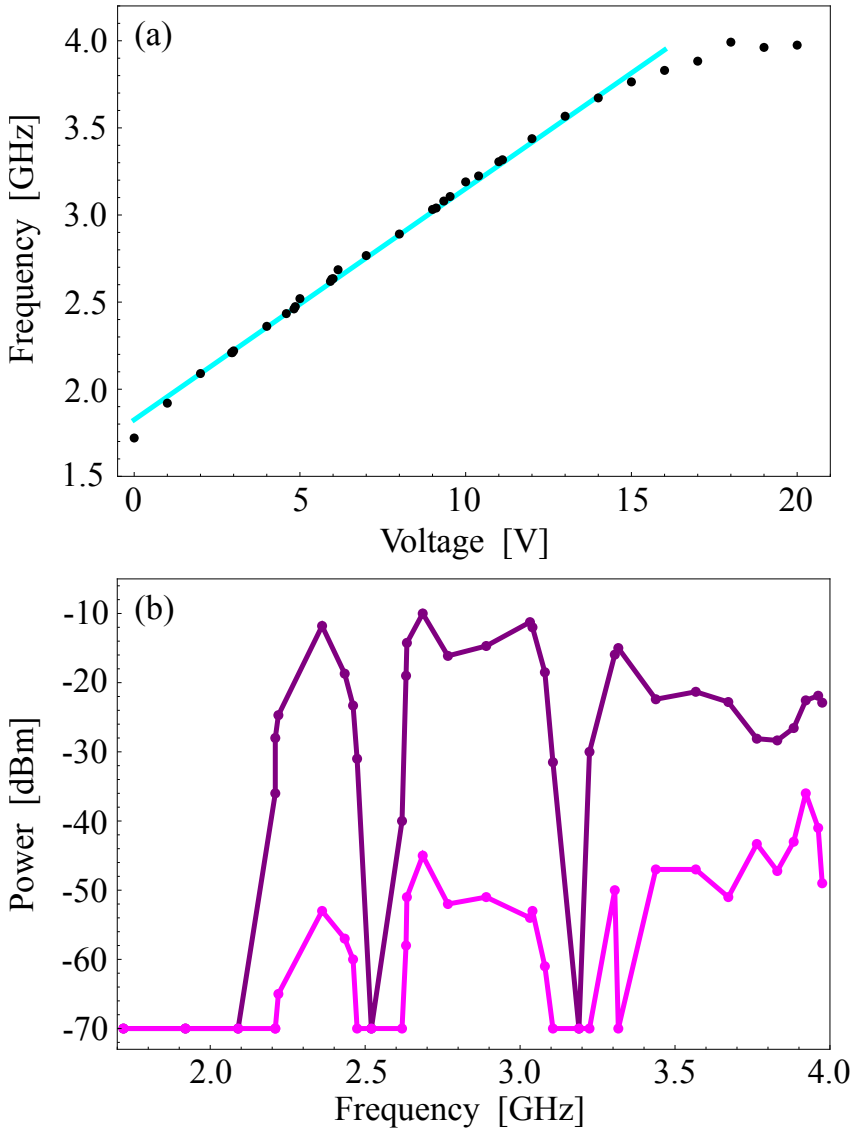

Fig. 6.7: (a) Tuning VCO frequency with respect to voltage given to control pin (black), also a linear to it (cyan). (b) Bode plot of the filters use in the RF driver, where we plot the power and frequency for fundamental signal (purple) and second harmonics (magenta)

able to generate this amount of voltage, so we additionally put a low noise OPAMP OP-07 which helps the PLL to reach the desired voltage. In our circuit, we use a bi-directional coupler whose operating range is 1.7 - 3.4 GHz and a band pass filter that removes any harmonics. This makes an equivalent bandpass filter, whose transfer function is measured and plotted in Fig. 6.7(b). The figure also shows the second harmonic power so that it can be easily compared with the power associated to the fundamental frequency. The required pass band from range of 2.6 - 3.1 GHz in this filter has a power variation upto 6(1) dBm and the difference between second and fundamental power is upto 40 dBm, which also clarifies about the 6^{th} order band

pass filter in this region. We also measure the phase noise at an operating frequency of 3.07 GHz is 125 dBc/Hz @ 17.70 MHz at an RF power of 10 dBm. The frequency stability of the VCO is measured to be 100(20) kHz and the power fluctuation is 0.08(3) dBm during 1 hr measurement. In our experiment, once the RF driver is fixed at a certain frequency, it does not require any further tuning.

6.5. Conclusion

In this chapter, we have described the requirement of the optical modulators *i.e* AOM and EOM along with the design specifications and working principle of the RF drivers which are used to drive these modulators for frequency modulation. The characterization parameters of one of the AOM drivers operating in the frequency tuning range of 150 - 250 MHz has also been reported. This AOM driver is completely computer controlled using our DACM modules which is previously described in Chapter 3. In AOM driver, we have used VVA which controls the RF power fluctuation and stabilizes laser intensity via an external servo controller. The EOM RF driver is able to generate 3.07 GHz frequency with a stability of 100(2) kHz and has a tunability range of 2.6 -3.1 GHz. We obtained transfer function of the filters which are used to suppress the higher order harmonics upto 40 dB during the generation of RF signal. Both EOM and AOM drivers are used in the optical setups of our Yb-ion experiment.

Chapter 7

Conclusion and Outlook

The accurate reference for time which is the most essential and fundamental unit of measurement that can be obtained with highest precision from atomic clocks. An atomic clock is nothing but precise measurement of an atomic transition frequency which is constant in nature and least perturbed by environmental factors which can be controlled. Most of the developed/developing countries maintain their local time using atomic clocks as it has direct linkage to the country's growth and security. Thus generation of accurate local time from state-of-the-art atomic clocks, maintenance of standard time and dissemination of that to the users is necessary. Together with that more accurate clocks with improved accuracy need to be developed to meet the requisites. In India, at CSIR -NPL, which is the NMI of the country, we are designing a state-of-the-art optical atomic clock using single trapped Yb ion, that will be able to generate time with an inaccuracy of 1 s over the age of the universe that is in other way few parts in 10^{18}. In future, optical atomic clock is also expected to be giving the new definition of SI second.

Developing the Yb ion based optical clock involves the accomplishment of a plethora of subsegments including designing, fabrication, instrumentation, various measurements, in the areas of vacuum system, optical setups, electronic modules and so on. This thesis expounds a wide variety of essential instrumentation that are part of the precision ion-trap experiment. These include indigenously designed and developed devices which are requisites of the experiment and laser locking techniques together with associated hardware to lock several lasers to be used and so on. An additional detailed theoretical study on estimation of BBR shift, magic wavelength and tuneout wavelength, has also been explicated in the thesis.

The protocol of the planned single trapped ion experiment includes production of Yb atoms, ionising them to produce Yb-ions, trapping, laser cooling and clock transition probing. During the experiment, the clock states get perturbed due to several external factors leading to uncertainty in the measurement, which can not be ignored to operate it as an accurate clock. Among

several environmental factors, BBR from the surrounding body is one of the major contributors for perturbing the clock states. We have therefore calculated the energy shift due to BBR using theoretical and experimental data, as described in Chapter 2. The static polarizabilities for the ground state $^2S_{1/2}$ and the metastable state $^2D_{3/2}$ are calculated using which the BBR shift is estimated to be -0.44(3) Hz at 25 ^{o}C. Our estimated values have improved accuracy compared to the previous estimated values [58], which matches well with the recent experiment [59]. The calculated polarizability value also aids in obtaining the magic wavelengths, tune out wavelengths for possible optical trapping of Yb^+ in an optical lattice. The results obtained in this study will be of immense interest for carrying out precision measurements in the $[4f^{14}6s]^2S_{1/2} \rightarrow [4f^{14}5d]^2D_{3/2}$ transition of Yb^+ for attaining high accuracy clock frequency and investigating fundamental physics.

In our experiment, the process of ion trapping to probe the clock transition eventuates within a few milliseconds and thus requires control of many electronics module like DC voltage source, tunable RF frequency to drive the optical modulators like AOMs, EOMs, mechanical shutters for fast switching on-off of the laser beams, current and voltage controller *etc.* To control all these modules manually within a small interval of time within which the experiment to be carried out, is not possible and thus they require complete automation so that their sequential operations are free from any human errors. We have developed an automation unit that is a DACM module, which hooks up with our every indigenously developed modules and connects each module through a common digital data bus using serial and parallel hybrid type communication protocol. The presented DACM module in Chapter 3 is able to control 64 different modules distinguished by unique individual addresses using 8 bit for address and 16 bit for controlling them. Performance of the DACM module is tested by using our indigenously developed ultra stable programmable DC voltage source, as described in Chapter 3. In our trapped ion experiment, the machining error due to fabrication of the ion trap causes significant offset of the potential minima relative to the center of the vacuum chamber. Due to this offset, ion position gets shifted from the center and as a result of that considerable amount of systematic shift arises. To minimize such errors, we have developed a low noise ultra stable DC voltage source which is connected with the compensating electrodes near the ion trap to control the motion of the trapped ion. The voltage source is able to generate 0 - 100 V DC with a resolution of 3 mV and long term stability of 1.9 mV over a few days. This voltage source is fully computer controlled through our DACM module and programmable from a remote PC. Further it is also used as a low frequency, high amplitude arbitrary waveform generator, which is useful for biasing piezo to tune different parameters in the experiment in a very controlled manner.

Once the ion is trapped, it has to be laser cooled to sub mK temperature for accurate probing of the clock transition. The lasers to be used for laser cooling need to have a high quality

factor and good frequency stability, which requires an active frequency stabilizer and a reference frequency. This necessitates the development of a laser frequency stabilization hardware module, which is able to lock the laser with respect to any atomic transition spectra or reference Fabry Perot cavity. For that purpose we have designed an developed an FPGA based module that incorporates all required modules in it. Its details are described in Chapter 4. The standard stabilization of laser frequencies requires function generator, lock-in amplifier and PID controller, which are programmed inside of a single FPGA chip. The bandwidth of our module is 100 kHz which can be extended further by different choice of ADC if required. The characterization of our FPGA based module is performed by locking a 780 nm laser with respect to D2 hyperfine transition of ^{87}Rb by a saturation absorption spectroscopy. In order to test universality of the instrument, we further tested its performance by using it in a Auger spectroscopy and optical coherence tomography. Compared to available commercial systems, we incorporated auto relock mechanism, that locks the laser to its set frequency automatically without any manual intervention. Using this module, we are able to lock laser frequency for more than a week in normal environmental conditions of the lab

The stability of laser frequency depends on stability of the reference points, which are typically generated by atomic transition spectra, transmission peak of ULE cavity and reference output of an optical frequency comb. In our Yb ion trap experiment, reference frequency generation via conventional SAS spectra is not possible for locking the required lasers with respect to an atomic transition. Other options e.g., ULE and frequency combs are very costly for the required purpose and also increase the experimental complexity. To encounter this problem we use another simple technique called transfer cavity locking, where we use a reference laser and first lock it's frequency with respect to an atomic transition, then we use this reference laser frequency to stabilize optical length of a FP cavity. The FP cavity is then treated as the reference cavity where we couple the lasers to be used in ion trap experiment and use PDH technique to stabilize their frequencies. The entire electronics for three stage locking, that are the reference laser, FP cavity and usable laser, are programmed inside of a single FPGA chip. This makes the system less noisy, compact and cost effective. We have demonstrated locking of the 739 nm laser using this transfer cavity locking, where the FP cavity is locked using a stabilized 780 nm laser. In this technique we are able to lock the 739 nm laser for more than two days. The details are described in Chapter 5.

The presence of hyperfine levels as shown in the energy diagram of Ytterbium, affirms the requirement of laser frequencies shifted by few hundred MHz to few GHz to drive different hyperfine transitions. Frequency of light can be shifted by using AOMs and EOMs. Chapter 6 of this thesis reports about the design and development of their respective drivers. Both the drivers are fully computer controlled. The AOM driver has frequency tuning range of 150 -

250 MHz, with a resolution of 20 kHz and suppresses the adjacent harmonics by 40 dB. The EOM, on the other hand has a tunability range of 2.6 -3.1 GHz with a stability of 100(2) kHz and resolution of 50 MHz and offers 40 dBm harmonic suppression.

Many essential building blocks as required for developing the complex experimental setup for trapped ion based optical atomic clock are developed within this thesis work. The described work brings a step forward towards realization of the planned experiment. At present, upon development of the described instrumentation, we are in a stage of Yb-ion production, its trapping in the ion trap and laser cooling. It is expected that the future works using the developed essential components within the scope of this thesis will lead CSIR-NPL towards completion of mission mode project “Quantum standard of time Via optical frequency standard”.

Bibliography

[1] SI Brochure: The International System of Units (SI): https://www.bipm.org/en/publications/si-brochure/

[2] V. Gerginov, N. Nemitz, S. Weyers, R. Schroder, D. Griebsch, and R. Wynands, Uncertanity evaluation of the caesium fountain clock PTB-CSF2, Metrologia. **47**, 65-79 (2010).

[3] H. Figger, C. zimmermann, D. Meschede, Application of atomic clock: F. N. Ramsey, Laser physics at the limits, Springer, Berlin, Heidelberg, pp 3-8 (2002).

[4] N. Poli, C. W. Oates, P. Gill and G. M. Tino, optical atomic clocks, Rivista del nuovo cimento **36**, 555-624 (2013).

[5] N. Huntemann, C. Sanner, B. Lipphardt, Chr. Tamm, and E. Piek, Single-ion atomic clock with 3×10^{-18} systematic uncertanity, Phys. Rev. Lett. **116**, 063001 (2016).

[6] Andrew D. Ludlow, Martin M. Boyd, Jun Ye, E. Piek and P. O. Schmidt, optical atomic clocks, Rev. Mod. Phys **87**, 638-692 (2015).

[7] Masao Takamoto, Feng-lei hong, Ryoichi higashi and, Hidetoshi katori, An optical lattice clock, Nature **435**, 321-324 (2005).

[8] W. W. Smith, D. S. Goodman, I. ssivarajah, J. E. Wells, S. Banerjee, R. Cote, H. H. Michels, J. A. Mongtomery Jr., and F. A. Narducci, Experiments with an ion-neutral hybrid trap:cold charge-exchange collisions, App. Phys. B. **114**, 75-80 (2014).

[9] D. Gallego, S. Hofferberth, T. Schumm, P. Kruger, and J. Schmiedmayer, Optical lattice on an atom chip, Optics letter **34**, 3463 (2009).

[10] Zachary L. Newman, Vincent maurice, Tara Drake, Jordan R. Stone, Travis C. Briles, Daryl T. Spence, Connor fredrick, Qing Li, Daron Westly, B. R. Ilic, Boqiang shen, Myoung-Gyun suh, Ki Youl Yang, Cort Johnson, Davis M. S. Johnson, Leo Hollberg, Kerry J. Vahala, Kartik srinivasan, Scott A. Diddams, John Kitching,

Scott B. Papp and Mathew T. Hummon,Architecture for the photonic integration of an optical atomic clock, Optica **5**, 680 (2019).

[11] N. Batra, A. Roy, S. Majhi, S. Panja, S. De, Singly charged ions for optical clocks, Assian Journal of Physics **25**,1069 (2016).

[12] Fritz riehle, Patrick gill, Felicitas arias, and Robertsson, The CIPM list of recommended frequency standard values: guidelines and procedures, Metrologia **55**, 188-200 (2018).

[13] S. De, N. Batra, S. Chakraborty, S. Panja and A. Sen gupta, Design of an ion trap for trapping single $^{171}Yb^{+}$, Curr. sci. **106**, 1348 (2014).

[14] Yuan Qian, Chang-da-ren Fang, Yao Huang, Hua guan, and Ke-Lin Gao,Optimization of endcap trap for single-ion manipulation, chin. Phys. B **27**, 063701 (2018).

[15] Kazuhio Sugiyama, Characterization of ytterbium ions stored in RF traps, Thesis, Kyoto University **1080** (1996).

[16] P. Taylor, M. Roberts, S. V. Gateva-kostova, R. B. M. Clarke, G. P. Barwood, W. R. C. Rowley and, P. Gill, Investigation of the $^{2}S_{1/2}$ - $^{2}D_{5/2}$ clock transition in a single ytterbium ion, Phys. Rev. A. **56**, 2699 (1997).

[17] A. Schacht, J. R. Danielson, S. Rahaman, J. R. Torgerson, J. Zhang and M. M. Schauer, $^{171}Yb^{+}$ $5D_{3/2}$ hyperfine state detection and F = 2 lifetime, J. Phys. B:At. Mol. Opt. Phys. **48**, 065003 (2015).

[18] E. Biemont and P. Quinet, Theoretical study of the $4f^{14}$6s $^{2}S_{1/2}$ - $4f^{13}6s^{2}$ $^{2}F_{7/2}$ E3 transition in Yb II, Phys. Rev. Lett. **81**, 3345 (1998).

[19] Peter T. H. Fisk, Matthew J. Sellars, Malcolm A. Lawn and Colin Coles, Accurate measurement of the 12.6 GHz clock transition in trapped $^{171}Yb^{+}$ ions, IEEE Trans. UFAFC **44**, 344(1997).

[20] S. Olmschenk, K. C. Younge, D. L. Moehring, D. N. Matsukevich, P. Maunz, and C. Monroe, Manipulation and detection of a trapped Yb^{+} hyperfine qubit, Phys. Rev. A **76**, 052314 (2007).

[21] Marianna S. Safronova, Viewpoint: Time trials for fundamental constants, APS Physics **7**, 117 (2014).

[22] R. M. Godun, P. B. R. Nisbet-Jones, J. M. Jones, S. A. King, L. A. M. Johnson, H. S. Margolis, K. Szymaniec, S. N. Lea, K. Bongs, and P. Gill, Frequency ratio of two optical clock transitions in $^{171}Yb^{+}$ and constraints on the time variation of fundamental constants, Phys. Rev. Lett **113**, 210801 (2014).

[23] Nils Nemitz, Takuya ohkubo, Masao Takamoto, Ichiro Ushijima, Manoj das, Noriaki Ohmae and Hidetoshi Katori, Frequency ratio of Yb and Sr clocks with 5×10^{-17} uncertainty at 150 second averaging time, Nat. Photonics **10**, 258 (2016).

[24] Christian sanner, Nils Huntemann, Richard Lange, Christian Tamm, Ekkehard Peik, Marianna S. Safronova and Serget G. Porsev, Optical clock comparision for lorentz symmetry testing, Nature. **567**, 204-208 (2019).

[25] E. H. Pinnington, G. Rieger and, J. A. Kernahan, Beam-laser measurement of the lifetimes of the 6p levels in Yb II, Phys. Rev. A **56**, 2421 (1997).

[26] Ann-Marie Martensson-Pendrill, Daavid S. Gough, and Peter Hannaford, Isotopes shifts and hyyperfine structure in the 369.4-nm 6s-$6p_{1/2}$ resonance line of singly ionized ytterbium, Phys. Rev. A **49**, 3351 (1994).

[27] M. Roberts, P. Taylor, S. V. Gateva-kostova, R. B. M. Clarke, G. P. Barwood, W. R. C. Rowley and, P. Gill, Measurement of the $^2S_{1/2}$ - $^2D_{5/2}$ clock transition in a single $^{171}Yb^+$ ion, Phys. Rev. A. **60**, 2867 (1999).

[28] C. Tamm, D. Schnier and, A. Bauch, Radio-frequency laser double-resonance spectroscopy of trapped ^{171}Yb ions and determination of line shifts of the ground-state hyperfine resonance, Appl. Phys. B. **60**,19-29 (1995).

[29] N. Huntemann, M. Okhapkin, B. Lipphardt, S. weyers, Chr. Tamm and E. Peik, High-accuracy optical clock based on the octupole transition in $^{171}Yb^+$, Phys. Rev. Lett. **108**, 090801 (2012).

[30] R Schmied, T Roscilde, V Murg, D Porras and J I Cirac, Quantum phases of trapped ions in an optical lattice, New Journal of Physics **10**, 045017 (2008).

[31] Florian Mintert and Christof Wunderlich, Ion-Trap Quantum Logic Using Long-Wavelength Radiation, Phys. Rev. Lett. **87**, 257904 (2001)

[32] D. Kielpinski, C. Monroe & D. J. Wineland, Architecture for a large-scale ion-trap quantum computer, Nature **417**, 709 (2002)

[33] R Schmied, T Roscilde, V Murg, D Porras and J I Cirac, Quantum phases of trapped ions in an optical lattice, New Journal of Physics **10**, 045017 (2008).

[34] Thaned Pruttivarasin1, Michael Ramm, Ishan Talukdar, Axel Kreuter and Hartmut Häffner, Trapped ions in optical lattices for probing oscillator chain models, New J. Phys, **13**, 075012 (2011)

[35] M. Roberts, P. Taylor, G. P. Barwood, W. R. C. Rowley, and P. Gill, Observation of the $^2S_{1/2} -^2 F_{7/2}$ electric octupole transition in a single $^{171}Yb^+$ ion, Phys. Rev. A **62**, 020501(R) (2000).

[36] Chr. Tamm, S. Weyers, B. Lipphardt and E. Peik, Stray-field-induced quadrupole shift and absolute frequency of the 688-THz $^{171}Yb^{+}$ single-ion optical frequency standard, Phys. Rev. A **80**, 043403 (2009).

[37] Y. Imai, K. Sugiyama, T. Nishi, S. Higashitani, T. Momiyama and M. Kitano, Poster No. B3-PWe21 *The* 12^{th} *Asia Pacific Physics Conference*, 14-19 July 2013.

[38] A. Rastogi, N. Batra, A. Roy, J. Thangjam, V. P. S. Kalsi, S. Panja and S. De, Design of the Ion Trap and Vacuum System for 171Yb-ion Optical Frequency Standard, Mapan **30**, 169 (2015)

[39] T. R. Tan, R. Kaewuam, K. J. Arnold, S. R. Chanu, Zhiqiang Zhang, M. S. Safronova, and M. D. Barrwtt, Suppressing inhomogeneous broadening in a lutetium multi-ion optical clock. axXiv: 1905.03486v1 (2019).

[40] K. Beloy, *Theory of the ac stark effect on the atomic hyperfine structure and applications to microwave atomic clocks* (2009), PhD thesis submitted to University of Nevada, Reno, USA.

[41] V. A. Dzuba, V. V. Flambaum, K. Beloy, and A. Derevianko, Hyperfine-mediated static polarizabilities of monovalent atoms and ions, Phys. Rev. A **82**, 062513 (2010).

[42] N. L. Manakov, V. D. Ovsiannikov, and L. P. Rapport, Atoms in a laser field, Phys. Rep. **141**, 320 (1986).

[43] S. G. Porsev and A. Derevianko, Multipolar theory of blackbody radiation shift of atomic energy levels and its implications for optical lattice clocks, Phys. Rev. A **74**, 020502(R) (2006).

[44] S. Singh, B. K. Sahoo, and B. Arora, Magnetic-sublevel-independent magic wavelengths: Application to Rb and Cs atoms, Phys. Rev. A **93**, 063422 (2016).

[45] Jasmeet Kaur, Sukhjit Singh, Bindiya Arora, and B. K. Sahoo, Magic wavelengths in the alkaline-earth-metal ions, Phys. Rev. A **92**, 031402 (2015).

[46] Bindiya Arora, D. K. Nandy and B. K. Sahoo, Multipolar blackbody radiation shifts for single-ion clocks, Phys. Rev. A **85**, 012506 (2012).

[47] Bindiya Arora, M. S. Safronova, and Charles W. Clark, Magic wavelengths for the np - ns transitions in alkali-metal atoms, Phys. Rev. A **76**, 052509 (2007).

[48] U. I. Safronova and M. S. Safronova, Third-order relativistic many-body calculations of energies, transition rates, hyperfine constants, and blackbody radiation shift in $^{171}Yb^{+}$, Phys. Rev. A **79**, 022512 (2009).

[49] B. K. Sahoo and B. P. Das, Parity nonconservation in ytterbium ion, Phy. Rev. A **84**, 010502(R) (2011).

[50] D. K. Nandy and B. K. Sahoo, Quadrupole shifts for the $^{171}Yb^{+}$ ion clocks: Experiments versus theories, Phys. Rev. A **90**, 050503(R) (2014).

[51] NIST atomic spectra Database, http : //www.nist.gov/pml/data/asd.cfm

[52] Y. Singh, B. K. Sahoo, and B. P. Das, Correlation trends in the ground-state static electric dipole polarizabilities of closed-shell atoms and ions, Phys. Rev. A **88**, 062504 (2013).

[53] E. H. Pinnington, G. Rieger, and J. A. Kernahan, Beam-laser measurements of the lifetimes of the 6p levels in Yb II, Phys. Rev. A **56**, 2421 (1997)

[54] S. G. Porsev, M. S. Safronova and M. G. Kozlov, Correlation effects in Yb^{+} and implications for parity violation, Phys. Rev. A **86**, 022504 (2012).

[55] D. Kedzierski, J. Kusz, J. Muzolf, Atomic transition probabilities for selected Yb II lines emitted from a ferroelectric plasma source, Spectrochimica Acta Part B. **65**, 248-252 (2010).

[56] E. Biemont, J. F. Dutrieux, I. Martin, and P. Quinet, Lifetime calculations in Yb II, J. Phys. B **31**, 3321 (1998).

[57] Hendrik M. Meyer, Matthias Steiner, Lothar Ratschbacher, Christoph Zipkes, and Michael Kohl, Laser spectroscopy and cooling of Yb^{+} ions on a deep-UV transition, Phys. Rev. A **85**, 012502 (2012).

[58] S. N. Lea, S. A. webster, G. P. Barwood, *Proceeding of the* 20^{th} *European Frequency and Time Forum (EFTF)*, edited by F. Riehle (PTB, Braunschweig, Germany, 2006), pp. 302-307.

[59] T. Schneider, E. Peik and C. Tamm, Sub-Hertz Optical Frequency Comparisons between Two Trapped $^{171}Yb^{+}$ Ions Phys. Rev. Lett. **94**, 230801 (2005).

[60] Chr. Tamm *et. al.*, *Proceeding* 20^{th} *European Frequency and Time Forum (EFTF)*, edited by F.Riehle(PTB, Braunschweig, Germany, 2006).

[61] S. De, N. Batra, S. Chakraborty, S. Panja, and A. Sen Gupta, Design of an ion trap for trapping single 171Yb+, Curr. Sci. **106**, 1348 (2014).

[62] N. Batra, B. K. Sahoo and S. De, An optimized ion trap geometry to measure quadrupole shifts of 171Yb+ clocks, Chin. Phys. B **25**, 113703 (2016).

[63] A. Rastogi, N. Batra, A. Roy, J. Thangjam, V. P. S. Kalsi, S. Panja, and S. De, Design of the ion trap and vacuum system for 171Yb+ ion optical frequency standard, MAPAN-Journal of Metrology Society of India **30**, 169 (2015).

[64] N. Batra, S. Panja, S. De, A. Roy, S. Majhi, S. Yadav and A. Sen Gupta, Design and construction of a helical resonator for delivering radio frequency to an ion trap, MAPAN-Journal of Metrology Society of India **32**, 193 (2017).

[65] S. Yadav, A. Acharya, P. Arora, and A. Sen Gupta, An electronic sequence controller for the Cs fountain frequency standard developed at CSIR-NPL India, Measurement **75**, 192 (2015).

[66] A. Agarwal and A. Sen Gupta, Frequency and intensity control of lasers to cool and control caesium atoms, MAPAN-Journal of Metrology society of India **27**, 169 (2012).

[67] P. Arora, S.B. Purnapatra, A. Acharya, R. Kumar and A. Sen Gupta, Measurement of temperature of atomic cloud using time of flight technique, MAPAN-Journal of Metrology society of India **27**, 31–39 (2012).

[68] A. Acharya, S. De, P. Arora, and A. Sen Gupta, A universal driver for vibration free operation of mechanical shutter, Measurement **61**, 16 (2014).

[69] N. Batra, A. Roy, C. Samal, S. Manjhi, S. Panja, and S. De, Automation of an optical frequency standard experiment, in *IEEE Conference Proceeding, CIEC, 2016*, (Kolkata, January 2016), p. 78-82.

[70] H. J. Lewandowski, D. M. Harber, D. L. Whitaker, and E. A. Cornell, Simplified System for Creating a Bose-Einstein Condensate, J. Low Temp. Phys. **132**, 309 (2003).

[71] S. F. Owen, and D. S. Hal, Fast Line Based Timming system for Labview, Rev. Sci. Instrum. **75** 259 (2004).

[72] D. S. Hall, Triggerable general-purpose interface bus controller, Rev. Sci. Instrum. **75**, 562 (2004).

[73] P. E. Gaskell, J. J. Thorn, S. Alba, and D. A. Steck, An open source, extensible system for laboratory timing and control, Rev. Sci. Instrum. **80**, 115103 (2009).

[74] A. Keshet, and W. Ketterle, A distributed, graphical user interface based, computer control system for atomic physics experiments, Rev. Sci. Instrum. **84**, 015105 (2013).

[75] E. E. Eyler, A single-chip event sequencer and related microcontroller instrumentation for Atomic physics research, Rev. Sci. Instrum. **82**, 013105 (2011).

[76] E. E. Eyler, Instrumentation for laser physics and spectroscopy using 32-bit microcontrollers with an Android tablet interface, Rev. Sci. Instrum. **84**, 103101 (2013).

[77] A. Roy, N. Batra, S. Majhi, S. Panja, A. Sen Gupta, and S. De, Design of a Stable DC Voltage Source and Computer Controlling of It Using an Indigenously Developed All-Digital Addressing-Cum-Control Hardware, MAPAN-Journal of Metrology Society of India, **33**, 139-145 (2019).

[78] A. L. Schawlow and C. H. Townes, Infrared and optical masers, Phys. Rev. **112**(6), 1940 (1958).

[79] Luc Couturier, Ingo Nosske, Facho Hu, Canzhu Tan, Chang Qiao, Y. H. Jiang, Peng Chen and Matthias Weidemuller, Laser frequency sabilization using a commercial wavelength meter, Rev. Sci. Instrum. **89**, 043103 (2018).

[80] Seung Koo Lee, Byoung Woong Han and D. Cho, Automatic system to relock a laser frequency to a Fabry-Perot cavity, Rev. Sci. Instrum. **76**, 026101 (2005).

[81] Eric D. Black, An introduction to Pound-Drever-Hall laser frequency stabilization, Rev. Sci. Instrum. **69**, 79 (2001).

[82] Arne Schwettmann, Jonathon sedlacek and James P. Shaffer, Field-programmable gate aray based locking circuit for external cavity diode laser frequency stabilization, Rev. Sci. Instrum. **82**, 103103 (2011).

[83] R. Nane, V. Sima, C. Pilato, J. Choi, B. Fort, A. Canis, Y. T. Chen, H. Hsiao, S. Brown, F. Ferrandi, J. Anderson, and K. Bertels, Survey and Evaluation of FPGA High-Level Synthesis Tools IEEE Trans. Comput.-Aided Des. Integr. Circuits Syst. **35**, 1591 (2016).

[84] Xilinx support is available at https://www.xilinx.com/support.html

[85] A. Restelli, R. Abbiati, and A. Geraci, Digital field programmable gate array-based lock-in amplifier for high performance photon counting applications, Rev. Sci. Instrum. **76**, 093112 (2005).

[86] J. Xiao, X. Wang, and Y. Feng, High-speed real-time data acquisition system based on FPGA, in *Proceedings of the 9th International Conference on Electronic Measurement & Instruments , Beijing, China, 2009, pp. 4-378-4-381.*

[87] S. N. Nikolic, V. Batic, B. Panic and B. M. Jelenkovic, Field-programmable gate array based arbitrary signal generator and oscilloscope for use in slow light and storage of light experiments, Rev. Sci. Instrum. **84**, 063108 (2013).

[88] A. Ryou and J. Simon, Active cancellation of acoustical resonances with an FPGA FIR filter, Rev. Sci. Instrum. **88**, 013101 (2017).

[89] E. D. Moris Jr. and H. S. Johnston, Digital Phase sensitive Detector, Rev. Sci. Instrum. **39**, 602 (1968).

[90] L. Samet, N. Masmoudi, M. W. Kharrat, and L. Kamoun, A digital PID controller for real time and multi loop control: a comparative study, in *IEEE Int. Conf. Electronics, Circuits and Systems. Surfing the Waves of Science and Technology (Cat. No.98EX196)*, Lisboa, Portugal, 1998, Vol.1, pp. 291-296.

[91] B. M. Sparkes, H. M. Chrzanowski, D. P. Parrain, B. C. Buchler, P. K. Lam, and T. Symul, A scalable, self-analyzing digital locking system for use on quantum optics experiments, Rev. Sci. Instrum. **82**, 075113 (2011).

[92] A. Schwettmann, J. Sedlacek, and P. James Shaffer, Field-Programmable gate array based locking circuit for external cavity diode laser frequency stabilization, Rev. Sci. Instrum. **82**, 103103 (2011).

[93] G. Yang, J. F. Barry, E. S. Shuman, M. H. Steinecker, and D. DeMille, A Low-cost FPGA-based servo controller with lock-in amplifier, J. Instrum. **7**, 10026 (2012).

[94] S. K. Lee, B. W. Han, and D. Cho, Automatic system to relock a laser frequency to a Fabry-Perot cavity, Rev. Sci. Instrum. **76**, 026101 (2005).

[95] J. Zhang, W. H. Yuan, K. Deng, A. Deng, Z. T. Xu, C. B. Qin, Z. H. Lu, and J. Luo, A long-term frequency stabilization deep ultraviolet laser for Mg+ ions trapping experiments, Rev. Sci. Instrum. **84**, 123109 (2013).

[96] D. R. Leibrandt and J. Heidecker, An open source digital servo for atomic, molecular and optics physics experiments, Rev. Sci. Instrum. **86**, 123115 (2015).

[97] N. B. Jorgensen, D. Birkmose, K. Trelborg, L. Wacker, N. Winter, A. J. Hilliard, M. G. Bason, and J. J. Arlt, A simple laser locking system based on a field programmable gate array, Rev. Sci. Instrum. **87**, 073106 (2016).

[98] S. Z. Yu, E. Fajeau, L. Q. Liu, D. J. Jones, and K. W. Madison, The performance and limitation of FPGA-based digital servos for atomic, molecular and optical physics experiments, Rev. Sci. Instrum. **89**, 025107 (2018).

[99] S. K. Lee, B. W. Han and D. Cho, Automatic system to relock a laser frequency to a Fabry Perot cavity, Rev. Sci. Instrum. **76**, 026101 (2005).

[100] D. R. Leibrandt and J. Heidecker, An open source digital servo for atomic, molecular and optical physics experiments, Rev. Sci . Instrum. **86**, 123115 (2015).

[101] H. C. Beica, A. Carew, A. Vorozcovs, P. Dowling, A. Pouliot, G. Singh, and A. Kumarakrishnan, An auto-locked diode laser system for precision metrology, in Proceedings of High-Power Diode Laser Technology XV, SPIE LASE, 2017, Vol. 100860.

[102] S. Bennett, Development of the PID controller, IEEE Control Systems Magazine **13**, 58 (1993).

[103] Y. Li, K. H. Ang, and G. C. Y. Chong, PID control system analysis and design, IEEE Control Systems Magazine **26**, 32 (2006).

[104] W. Yang, D. Kelly, I. Mehar, M. T. Sayuk and L. Singer, A 3-V 340-mW 14-b 75 Msample/s CMOS ADC with 85-dB SFDR at Nyquist Input, IEEE J. Solid State Circuits **36**, 1931 (2001).

[105] IIR filter roll off available in wikipedia: https://en.wikipedia.org/wiki/Roll-off

[106] Daryl W. Preston, Doppler-free saturated absorption: Laser Spectroscopy, Am. J. Phys. **64**, 1432 (1996).

[107] U. Heiz, F. Vanolli, L. Trento, and W. D. Schneider, Chemical reactivity of size-selected supported clusters: An experimental setup, Rev. Sci. Instrum. **8**, 1986 (1997).

[108] K. Divakar Rao, D. V. Udupa, C. Prathap, A. Rathod, R. Balasubramaniam, and N. K. Sahoo, Optical coherence tomography for shape and radius of curvature , measurement of deeply curved machined metallic surfaces: a comparision with two-beam laser interferometry, Opt. Lasers Eng. **66**, 204 (2015).

[109] A. Rastogi, N. Batra, A. Roy, J. Thangjam, V. P. S. Kalsi, S. Panja, and S. De, Design of the ion trap and vaccum system for 171Ybion optical frequency standard, MAPAN-J. Metrology Soc. India **30**, 169 (2015).

[110] John L. Hall, Nobel Lecture: Defining and measuring optical frequencies, Rev. Mod. Phy. **78**, 1279 (2006).

[111] Christian Hagemann, Christian Grebing, Christian Lisdat, Stephan Falke, Thomas Legero, Uwe Sterr, Fritz Riehle, Michael J. Martin, and Jun Ye, Ultrastable laser with average fractional frequency drift rate below 5 $\times 10^{-19}$/s, Opt. Lett. **39**, 5102-5105 (2014).

[112] Ch. Eisele, A. Yu. Nevsky, and S. Schiller, Laboratory test of the isotropy of light propogation at the 10^{-17} level, Phys. Rev. Lett **103**, 090401 (2009).

[113] J. E. Debs, N. P.Robins, A. Lance, M. B. Kruger, and J. D. Close, Piezo-locking a diode laser with saturated absorption spectroscopy, Applied Optics **47**, 5163 (2008).

[114] Eric D. Black, An introduction to Pound-Drever-Hall laser frequency stabilization, American Journal of Physics **69**, 79 (2001).

[115] A. D. Ludlow, X. Huang, M. Nootcutt, T. Zanon-Willette, S. M. Foreman, M. M. Boyd, S. Blatt, and J. Ye, Compact thermal -noise-limited optial cavity for diode laser stabilization at 1×10^{-15} , Opt. Lett **32**, 641 (2007).

[116] Th. U dem, R. Holzwarth and T. W. Hansch, Optical frequency metrology, Nature **416**, 233-237 (2002).

[117] Luc Couturier, Ingo Nosske, Fachao Hu, Canzhu Tan, Chang Qiao, Y. H. Jiang, Peng Chen, and Matthias Weidemuller, Laser frequency stabilization using a commercial wavelength meter, Rev. Sci. Instrum **89**, 043103 (2018).

[118] S. De, U. Dammalapati, K. Jungmann, and L. Willmann, Magneto-optical trapping of barium, Phys. Rev. A **79**, 041402(R) (2009).

[119] J. R. Guest, N. D. Scielzo, I. Ahmad, K. Bailey, J. P. Greene, R. J. Holt, Z. T. Lu, T. P. O'connor, and D. H. Potterveld, Laser trapping of ^{225}Ra and ^{226}Ra with repumping by room temperature blackbody radiation, Phys. Rev. Lett **98**, 093001 (2007).

[120] K. Honda, Y. Takahashi, T. Kuwamoto, M. Fujimoto, K. Toyoda, Magneto-optical trapping of Yb atoms and a limit on the branching ratio of the $^1P_1$ state, Phys. Rev. A **59**, 2603(R) (1999).

[121] K. R. Vogel, T. P. Dinneen, A. Gallagher and J. L. Hall, Narrow-line Doppler cooling of strontium to the recoil limit, in IEEE Transactions on Instrumentation and Measurement, **48**, 618-621 (1999).

[122] Higgins, Gerard and Li, Weibin and Pokorny, Fabian and Zhang, Chi and Kress, Florian and Maier, Christine and Haag, Johannes and Bodart, Quentin and Lesanovsky, Igor and Hennrich, Markus,Single Strontium Rydberg Ion Confined in a Paul Trap, Phys. Rev. X, **7**, 021038 (2017).

[123] James J. McLoughlin, Altaf H. Nizamani, James D. Siverns, Robin C. Sterling, Marcus D. Hughes, Bjoern Lekitsch, Bjorn Stein, Seb Weidt, and Winfried K. Hensinger, Versatile ytterbium ion trap experiment for operation of scalable ion-trap chip motional heating and transition-frequency measurement, Phys. Rev. A, **83**, 013406 (2011).

[124] Julia Benedikter, Thomas Hummer, Matthias Mader, Benedikt, Schlederer, Jakob Reichel, Theodor W Hansch and David Hunger, Transverse-mode coupling and diffraction loss in tunable Fabry–Perot microcavities, New. J. Phys., **17**, 053051 (2015).

[125] L. Richter, H. Mandelberg, M. Kruger and P. McGrath, Linewidth determination from self-heterodyne measurements with subcoherence delay times, in IEEE Journal of Quantum Electronics, **22**, 2070-2074 (1986).

[126] Gianni Di Domenico, Stephane Schilt, and Pierre Thomann, Simple approach to the relation between laser frequency noise and laser line shape, Applied Optics, **49**, 4801 (2010).

[127] Dennis R. Pape, Spatial light modulator technology: Materials, Devices and Application, edited by Uzi Efron, Optical engineering, New York **47**,p 415 (1994)

[128] E. A. Donley, T. P. Heavner, F. Levi, M. O. Tataw, and S. R. Jefferts, Double-pass acousto-optic modulator system, Rev. Sci. Instrum **76**, 63112 (2005).

[129] Darren D. Hudson, Kevin W. Holman, R. Jason Jones, Steven T. Cundiff, Jun Ye, and David J. Jones, Mode-locked fiber laser frequency-controlled with an intracavity electro-optic modulator, Opt. Lett. **30**, 2948-2950 (2005).

[130] Theresa A. Maldonado, Michael bass, Eric W. Van Stryland, David R.Williams, W. L. Wolfe, HandBook of Optics:Electro-optic modulators, **2**, 13.1-13.35 (1995).

[131] N. J. Berg, Acousto-optic signal processing: Theory and implementation, edited by N. J. Berg and J. N. Lee, Optical Engineering, New York **2**, 496 (1983).

[132] Kakeru Takahashi, Masaki Ando and Kimio Tsubono, Stabilization of laser intensity and frequency using optical fiber, J. Phys: Conf. Ser. **122**, 012016 (2008).

[133] ISOMET Acousto optic modulator: http://www.isomet.com/acousto optic modulators.html

[134] Newport Electro optic modulator: https://www.newport.com/c/electro-optic-modulators

[135] Eddie H. Young, JR., and Shi-Kay Yao, Design considettion for Acousto-Optic Devices, IEEE Proceeding **69**, 54-64 (1981).

[136] Electro optic modulator, Wikipedia: https://en.wikipedia.org/wiki/Electro-optic modulator

[137] Robert P. Gilmore, Direct digital synthesizer driven phase lock loop frequency synthesizer, Qualcomm Inc. US patent **4965533** (1990)

[138] Jose I. Suarez, Voltage controlled oscillator with current control, Mororol Inc, US patent **5175884**, (1992).

[139] Y. R. Shayan and T. Le-Ngoc, All digital phase-locked loop: concepts, design and applications, IEEE Proceedings F - Radar and Signal Processing, **136**, 53-56 (1989).

Publications

Journals

1 A. Rastogi, N. Batra, **A. Roy**, J. Thangjam, V. P. S. Kalsi, S. Panja and S. De, Design of the ion trap and vacuum system for ^{171}Yb-ion optical frequency standard, MAPAN **30**, 169-174 (2015).

2 N. Batra, **A. Roy**, S. Majhi, S. Panja, S. De, Single charged ions for optical clocks, Asian Journal of Physics **25**, 9 (2016).

3 N. Batra, S. Panja, S. De, **A. Roy**, S. Majhi, S. Yadav and A. Sen Gupta, Design and Construction of Helical Resonator for Delivering Radio Frequency to an Ion Trap, MAPAN **32**, 193-198 (2017).

4 **A. Roy**, S. De, Bindiya Arora and B. K. Sahoo, Accurate determination of black-body radiation shift, magic and tune-out wavelength for the $6S_{1/2} \rightarrow 5D_{3/2}$ clock transition in Yb^+, J. Phys. B: At. Mol. Opt. Phys. **50**, 205201 (2017).

5 **A. Roy**, N. Batra, S. Majhi, S. Panja, A. Sen Gupta, and S. De, Design of a Stable DC Voltage Source and Computer Controlling of it Using an Indigenously Developed All-Digital Addressing-Cum-Control Hardware, MAPAN **33**, 139-145 (2017).

6 Lakhi Sharma, **A. Roy**, S. Panja, V. N. Ojha and S. De, Estimation of the ion-trap assisted electrical loads and resulting BBR shift, Scientific Reports **8**, 16884 (2018).

7 Lakhi Sharma, **A. Roy**, S. Panja, and S. De, Atomic flux distribution from a low-divergent dark wall oven, Rev. Sci. Inst. **90**, 053201 (2019).

8 **A. Roy**, Lakhi Sharma, I. Chakraborty, S. Panja, V. N. Ojha and S. De, An FPGA based all-in-one function generator, lock-in amplifier and auto-relockable PID system, JINST **14**, 05012 (2019).

Conference Proceedings

1 **A. Roy**, A. Rastogi, N. Batra, J.Thangjam, A. Acharya, S. De, P. Arora, S. Panja and A. Sen Gupta, Instrumentation for Atomic Clock experiment, in *Proceedings of the National Conference for Advances in Metrology, CSIR-CMERI, Durgapur, 2015.*

2 S. De, N. Batra, A. Rastogi, **A. Roy**, J. Thangjam, S. Yadav, S. Panja, and A. Sen Gupta, Ytterbium ion optical frequency standard, in *Proceedings of the Current Developments in Atomic Molecular and Optical Physics (CDAMOP), Delhi University, 2015.*

3 N. Batra, **A. Roy**, S. Panja, and S. De, Developing the first optical atomic clock in India, in *Proceedings of the India International Science Festival, IIT Delhi, 2015.*

4 S. Panja, S. De, N. Batra, A. Rastogi, **A. Roy**, N. Varsney, C. Samol and A. Sen Gupta, Development of an optical frequency standard at CSIR-NPL, in *Proceedings of the International Union of Radio Science: URSI-RCRS, JNU, New Delhi, 2015.*

5 S. De, N. Batra, **A. Roy**, N. Varshney, C. Samal, and S. Panja, Developing Ytterbium-ion Optical Frequency Standards in India, in *Proceedings of the Cold atom GDR, Paris, France, 2015.*

6 S. De, N. Batra, **A. Roy**, C. Samal, S. Mjhi, and S. Panja, Ytterbium-ion trap: aiming for optical frequency standard and precision measurements, in *Proceedings of the Charged particle collisions and electronic processes in atoms, molecules and materials (q-PaCE 2016), ISM Dhanbad, 2016*

7 **A.Roy**, N.Batra, S.Manjhi, C.Samal, S.Panja, B.K.Sahoo, B.Arora and S.De, Energy Shifts and Magic wavelength of $^{171}Yb^{+}$ clock transition, in *Proceedings of the AdMet: International Conference for Advances in Metrology, CSIR-NPL, New Delhi, 2016.*

8 N. Batra, **A. Roy**, S. Majhi, S. Panja and S. De, Automation of an optical frequency standard experiment, in *Proceedings of the IEEE Explore, International Conference on Control, Instrumentation, Energy & Communication (CIEC), Kolkata, 2016.*

9 **A.Roy** ,B. Arora, B. K. Sahoo, and S. De, Optical lattice of ytterbium-ion: possibility to build next generation commercial clock, in *Proceedings of the India International Science Festival (IISF), CSIR-NPL, 2016.*

10 **A.Roy**, N. Batra, L. Sharma, S. Panja and S. De, Laser locking with FPGA based advanced electronics modules, in *Proceedings of the DAE-BRNS, National Laser Symposium (NLS) – 25, KIIT University, 2016.*

11 **A.Roy**, Bindiya Arora, B. K. Sahoo and S. De, Accurate polarizability calculation of the states for the $6S_{1/2}$-$5D_{3/2}$ clock transition in Yb ion, in *Proceedings of the 21st NCAMP abstract book, Physical Research Laboratory, Ahemdabad, 2017.*

12 **A.Roy**, B. Arora, B. K Sahoo and S. De., Polarizability abd magic wavelength of Yb+ clock transition $2S_{1/2}$ – $2D_{3/2}$, in *Proceedings of the IEEE - EFTF, Besancon, France, 2017.*

13 **A.Roy**, Bindiya Arora, B. k. Sahoo, N. Batra, L. Sharma, K. Sharma, S. Panja and S. De, Developing optical frequency standard using single Yb ion, in *Proceedings of the SERB School SPIE event, IIT Guwahati, 2017.*

14 **A.Roy**, L. Sharma, S. Panja and S. De, FPGA based Lock-in amplifier and PID controller, in *Proceedings of the META-2018, NCRA-TIFR, Pune, 2018.*

15 **A.Roy**, N. Batra, S. Panja, S. De, Computer controlled, low noise and ultra stable DC voltage source, in *Proceedings of the NCEEM, CSIR-NPL, New Delhi, 2018.*

16 **A.Roy**, L. Sharma, I. Chakraborty, S. Panja, V. N. Ojha and S. De, Demonstration of self-relocking on laser frequency, in *Proceedings of the AdMet: International Conference for Advances in Metrology, CSIR-NPL, New Delhi, 2019.*